ASSESSMENT OF THE UTILITY OF SM ARTPHONES FOR WATER QUALITY MONITORING

PETER N-JONAAM MAHAMA

FEBRUARY, 2016

SUPERVISORS:
DR. IR. MHD. SUHYB SALAMA
DR. IR. ROGIER VAN DER VELDE

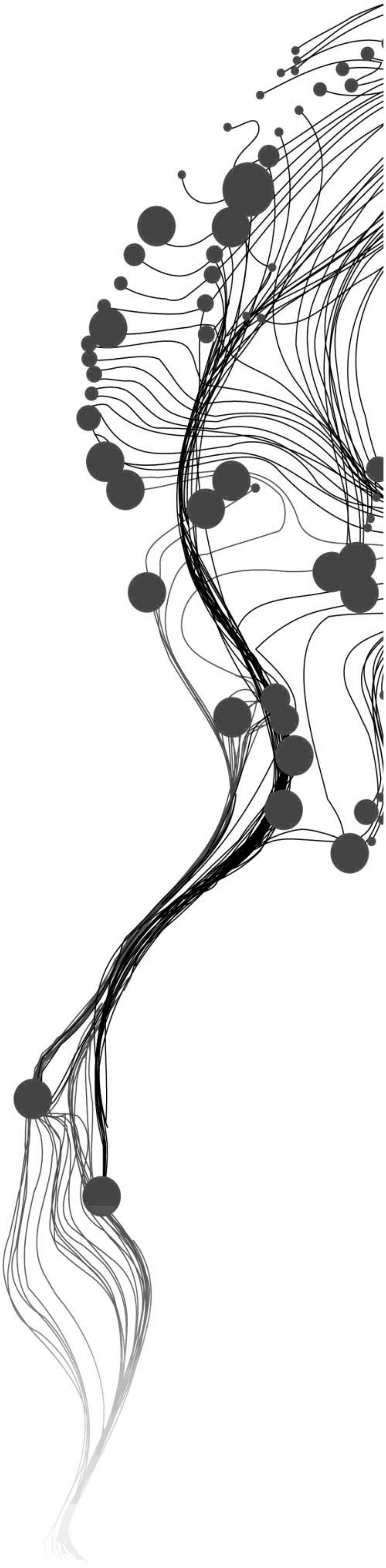

ASSESSMENT OF THE UTILITY OF SMARTPHONES FOR WATER QUALITY MONITORING

PETER N-JONAAM MAHAMA
ENSCHEDE, THE NETHERLANDS,
FEBRUARY, 2016

Thesis submitted to the Faculty of Geo-Information Science and Earth Observation of the University of Twente in partial fulfilment of the requirements for the degree of Master of Science in Geo-information Science and Earth Observation.
Specialisation: Water Resources and Environmental Management

SUPERVISORS:
Dr. Ir. Mhd. Suhyb Salama
Dr. Ir. Rogier van der Velde

THESIS ASSESSMENT BOARD:
Dr. Ir. C. M. M. Mannaerts (Chair)
Dr. H. J. van der Woerd (External Examiner, Institute for Environmental Studies (IVM), Vrije Universiteit, Amsterdam)

DISCLAIMER

DEDICATION

I dedicate this research work to my late father Rev. Ubor. John Wesley Mahama Nandak II, whose journey to heaven occurred in the course of my journey through this research work.

ABSTRACT

With society becoming increasingly cautious and aware of their environment, monitoring and sensor platforms are shifting toward empowering citizens with the capability to collect, process and share information about their environment. In terms of water quality monitoring, the ubiquity of smartphones makes it the better tool to achieve such goal through the development and use of smartphone applications (APPs). The capability of smartphones through APPs to quantify water quality variables such as colour, turbidity and the concentration of suspended particulate materials ([SPM]) have been the subject of this thesis. This was accomplished by evaluating two existing smartphone APPs: HydroColor and Citclops. Both APPs use the RGB channels of images acquired by the smartphone camera. However, the two APPs use different transfer functions (colour space) to estimate water quality variables. The HydroColor APP uses the RGB channels of the smartphone images taken of a gray card, sky and water surface to convert to remote sensing reflectance, $R_{rs}(RGB)$. Using specific models, the $R_{rs}(RGB)$ is used to estimate turbidity and [SPM]. For the Citclops APP, the RGB channels of a smartphone water surface image is converted to xyz chromaticity coordinates which is used to index the colour of the water image as a Forel-Ule index (FUI). Field measurements using hyperspectral sensors were carried out and used to calibrate and validate the $R_{rs}(RGB)$ and xyz chromaticity coordinates derived from smartphone images. Results of laboratory analysis of turbidity and [SPM] of corresponding areas of the smartphone images were also used to validate estimates of turbidity and [SPM] from the smartphone images through the models used by the APPs. The specified models of the HydroColor APP estimate have 0.36 and 0.83 of R^2 values for turbidity and [SPM] respectively. The HydroColor APP uses 0.044 sr^{-1} as the water surface reflectance saturation limit from which it can give estimate of turbidity and [SPM]. By this, according to the HydroColor APP model, the estimate of turbidity and [SPM] at half the saturation limit (that is, 0.022 sr^{-1}) are 22.57 NTU and 21.91 gm^{-3} respectively. Thus, the HydroColor APP cannot be used to estimate turbidity and [SPM] for very turbid water systems whose reflectance exceeds the saturation limit. To improve upon the HydroColor APP estimate of turbidity and [SPM], this research employed, calibrated and validated a semi-analytical model and a logarithmic model. The logarithmic model was the better model in terms of accuracy whiles the semi-analytical model can be used to estimate very turbid water systems. The Citclops APP which estimates water colour translated to FUI derived from the smartphone images resulted in $R^2 = 0.7$ in comparison to FUI estimates from the hyperspectral sensors. To obtain more water quality variable estimates which can be used by the Citclops APP, this research employed, calibrated and validated a semi-analytical model and a logarithmic model. As a pilot study, the chromaticity coordinates of the smartphone images were used to estimate turbidity and [SPM] through the semi-analytical and logarithmic models. The logarithmic model was the better model compared to the semi-analytical model. The research, therefore, showed that the logarithmic model performed better in estimating turbidity and [SPM] from smartphone images for the two colour space of the APPs. Comparing the proposed logarithmic model results of the two APPs in estimating the water quality variables, the HydroColor APP gave more accurate [SPM] estimate of $R^2 = 0.90$ compared to Citclops APP of $R^2 = 0.79$. For turbidity the Citclops APP gave more accurate estimate of $R^2 = 0.73$ compared to HydroColor APP of $R^2 = 0.63$. Although the two colour space used by HydroColor APP and Citclops APP are different, they can be converted from one colour space to another. The research, however, recommends that the colour space used by Citclops is an easy and efficient colour space to be used in a smartphone APP for water quality monitoring by citizens since it uses only the water surface image. These research findings therefore introduced innovative ways to improve on water quality monitoring using smartphone APPs.

Keywords: colour, smartphone image, Citclops APP, HydroColor APP, concentration of suspended particulate materials ([SPM]), turbidity.

ACKNOWLEDGEMENTS

I want to thank the Almighty God for his unfathomable grace and protection throughout this research work.

I would like to extend my profound gratitude to my supervisor, Dr. Ir. Mhd. Suhyb Salama for his relentless time in supervising this research work. Your time spent with us during the field campaigns and data collection will continue to linger through my mind. Not forgetting the time I had with my second supervisor, Dr. Ir. Rogier van der Velde. I also want to thank my external supervisor Dr. Marcel R. Wernand of the Department of Oceanography of the Royal Institute for Sea Research, The Netherlands. I would also like to thank Dr. Ir. Chris M. M. Mannaerts for his time and support during the field work and laboratory analysis of water samples at the ITC – WREM laboratory.

I would like to thank the Vechtstromen and Brabantsedelta Water Boards for their supports. In particular I am indebted to Arjan Segeren, Guido Waajen from the Brabantsedelta, Sjon Monnix and Leontien van der Molen from Vechtstromen and Bas Waanders, Park manager of Het Hulsbeek for providing the sampling boats and facilitating the field works. I also want to thank my colleagues (Justin Yieri, Christian Kwasi Owusu and Mujeeb Rahman Nuhu) for their support during our data collection.

My profound gratitude to Dr. Shungu P. Garaba of the Marine Science Department of the University of Oldenburg for the MATLAB codes to derive FUI. Not to forget Mrs. Irina Miranda Miguel for the Alcatel One Touch 7041D smartphone for this research work.

I wish to thank Ir. Arno. M. van Lieshout, the course director of WREM for his resourceful time and attention especially when I lost my father during this research work. I wish to also thank the WREM course secretaries especially Tina E. L. Butt-Castro for her kind words and encouragement during this research work.

I am grateful to the University of Twente – ITC Scholarship for the scholarship grant offered me for the whole study period of my M. Sc. Programme.

I wish to thank my parents; the late Rev. Ubor. John Wesley Mahama Nandak II and Mrs. Grace Mawan Mahama and siblings; Samuel, Emmanuel, Joshua, Peace, Mercy, Paul and Priscilla for their prayers, love, encouragement and support during my M. Sc. Programme.

TABLE OF CONTENTS

DEDICATION i

ABSTRACT ii

ACKNOWLEDGEMENTS iv

TABLE OF CONTENTS v

LIST OF FIGURES viii

LIST OF TABLES xv

NOTATIONS xvi

ABBREVIATIONS xvii

1. INTRODUCTION 1

- 1.1. Research Background 1
- 1.2. Problem Statement 3
- 1.3. Research Objective 4
- 1.4. Research Questions 4

2. LITERATURE REVIEW 5

- 2.1. Colour Vision 5
- 2.2. Colour Space 5
- 2.3. Water Colour 6
- 2.4. Remote Sensing of Water Quality 7
- 2.5. Water Quality Variables 7

3. STUDY AREA AND DATA SET 8

- 3.1. Study Area 8
- 3.1.1. Binnenschelde Lake and Markiezaatsmeer Lake 9
- 3.1.2. Hulsbeek Lake and Kristalbad Artificial Wetland 10
- 3.2. Data Set 12
- 3.3. Optical Field Measurement 13
- 3.4. Laboratory Analysis 15
- 3.4.1. Turbidity 15
- 3.4.2. Suspended Particulate Materials (SPM) 15

4. RESEARCH APPROACH AND METHODOLOGY 17

- 4.1. Summary of Data Analysis and Flow Chart 17

4.2. Deriving Remote Sensing Reflectance 19
4.3. HydroColor Data Processing 20
4.3.1. Converting RAMSES $R_{rs}(\lambda)$ to $R_{rs}(RGB)$ 20
4.3.2. Deriving $R_{rs}(RGB)$ from Smartphone Images 22
4.3.3. Deriving HydroColor APP Water Quality Variables 24
4.3.4. Assessment of Alternative Models to Estimate Turbidity and [SPM] 24
4.3.5. Error Quantification 25
4.4. Citclops Data Processing 26
4.4.1. Converting RAMSES $R_{rs}(\lambda)$ to FUI 26
4.4.2. Deriving FUI from Smartphone Images 28
4.4.3. Comparison of RAMSES and Smartphone Images xyz Chromaticity Coordinates 32
4.4.4. Deriving Water Quality Variables for Citclops APP 32
4.4.5. Error Quantification 32
4.4.6. Deriving Colour Saturation and Dominant Wavelength 33
5. RESULTS AND DISCUSSIONS 35
5.1. Remote Sensing Reflectance 35
5.2. Laboratory measurements 39
5.3. Smartphone Images Analysis 40
6. HYDROCOLOR APP 43
6.1. Calibration of the Printed Grey Paper 43
6.2. Comparison of RAMSES $R_{rs}(RGB)$ and Smartphone Images $R_{rs}(RGB)$ 44
6.3. Assessment of HydroColor APP Water Quality Variables 45
6.3.1. Limitation of HydroColor APP Models 48
6.4. Alternative Approaches for Estimating [SPM] 50
6.4.1. Limitation of the Proposed HydroColor [SPM] Models 53
6.5. Alternative Approaches for Estimating Turbidity 54
6.5.1. Limitation of the Proposed Turbidity Models 55
6.6. Error Quantification of the HydroColor APP Models 56
6.7. Accuracy of the HydroColor APP Models 57
7. CITCLOPS APP 59
7.1. Comparison of RAMSES xyz and Smartphone Images xyz 59

7.2. Hue Colour Angles and Forel-Ule Index 61
7.3. Assessment of the Chromaticity Coordinates for Estimating Water Quality Variables 65
7.4. Estimating the [SPM] from the x Chromaticity Coordinate 67
7.4.1. Limitation of the Proposed [SPM] Models 67
7.5. Estimating Turbidity from the *x* Chromaticity Coordinate 68
7.5.1. Limitation of the Proposed Turbidity Models 69
7.6. Error Quantification of the Proposed Citclops APP Models 70
7.7. Accuracy of Citclops APP Models 72
7.8. Colour Saturation as a Measure of Water Transparency 72
8. CONCLUSION AND RECOMMENDATIONS 75
8.1. Conclusion 75
8.2. Recommendations 77
LIST OF REFERENCES 79
ANNEX I – LINKS TO THE APPs USED 87
ANNEX II - CITCLOPS APP USAGE 87
ANNEX III - HYDROCOLOR APP USAGE 89
ANNEX IV - COMPARISON OF CITCLOPS AND HYDROCOLOR APPS 90
ANNEX V – PROCESSED SMARTPHONE IMAGES 92

LIST OF FIGURES

Figure 1: Google Earth map showing the overlaid study sites (red dots) in the Netherlands country boundary (yellow line). 8

Figure 2: Google imagery map showing Binnenschelde Lake (blue boundary line) and Markiezaatsmeer Lake (yellow boundary line) with overlaid sampled points (red dots). 10

Figure 3: Google imagery map showing Hulsbeek Lake (yellow boundary line) with overlaid sampled points (red dots). 11

Figure 4: Google imagery map showing Kristalbad artificial wetland (yellow boundary line) with overlaid sampled points (red dots). 12

Figure 5: Instrumental set-up, calibration and measurement of turbidity. (a) Gelex secondary turbidity standards of know turbidity values. (b) Turbidimeter reading in NTU of the measured water sample. 15

Figure 6: Instrumental set-up for the measurement of suspended particulate materials SPM. (a) Electronic balance used for measuring the weight of the filter papers. (b) Oven drying of the filter papers containing total suspended materials after filtering the water samples. 16

Figure 7: Flow chart of the research work; Citclops and HydroColor APPs assessment using hyperspectral sensors (RAMSES) and laboratory measurements. 18

Figure 8: The standard 2-degree field of view colour matching functions (CMF) of CIE1931. Values used to generate the CMF curves were obtained from http://cvrl.ioo.ucl.ac.uk/cmfs.htm. (a) Tristimulus response of the CIE1931 CMF ($x\ y\ z$). (b) Normalized tristimulus response of the CIE1931 CMF ($x\ y\ z$). 21

Figure 9: An illustration of the smartphone images processing to derive remote sensing reflectance $R_{rs}(RGB)$. The uper panel is the cropping of the images, middle panel is the derivation of the histograms of the images and the lower panel is the derivation of the resulting $R_{rs}(RGB)$ from the images. The $R_{rs}(RGB)$ image was taken from Leeuw (2014). 23

Figure 10: Hue colour angles $\alpha_N(°)$ and their corresponding Forel-Ule index (FU 1 to 21) of Novoa et al. (2013). These $\alpha_N(°)$ were derived from laboratory FU solutions of transmission measurements of their research. 28

Figure 11: Structural diagram of the processes used to derive the xyz chromaticity coordinates, hue colour angle $\alpha_P(°)$ and Forel-Ule index FUI of the smartphone images adapted from Novoa et al. (2015)......31

Figure 12: An illustration of the derivation of radians and angles from the *xy* chromaticity coordinate on a polar coordinate system. The left panel is the *xy* chromaticity coordinates of CIE1931 2-degree standard observation for spectrally pure colours at specific wavelengths (λ). Source: Colour & Vision Research Laboratory Database http://cvrl.ioo.ucl.ac.uk/cmfs.htm. The right panel is the *xy* chromaticity coordinates of a polar coordinate system showing the four quadrants of the polar coordinate system. The white point (WP) is indicated as the origin......33

Figure 13: Spectral reflectance curves of water surface reflectance and remote sensing reflectance derived using different sun-sky glint correction factors applied to different water bodies. (a) Spectral reflectance curves of a clear water. (b) Spectral reflectance curves of a chlorophyll-a pigment materials dominated water. (c) Spectral reflectance curves of a CDOM dominated water......36

Figure 14: Spectral reflectance curves (blue lines) for the sample sites and their corresponding coefficient of variation of the wavelengths (red line). For all the measurements, Mobley (1999) sun-sky glint correction factor of 0.028 was used to correct for specular reflectance except for Hulsbeek Lake (c). (a) Binnenschelde Lake; (b) Markiezaatsmeer Lake; (c) Hulsbeek Lake; (d) Kristalbad Artificial Wetland; (e) CDOM dominated pit water sampled near Kristalbad wetland......37

Figure 15: Bar plots of laboratory measured water quality variables with respect to their sample sites. (a) Turbidity. (b) [SPM], the concnetration of suspended particulate materials......40

Figure 16: Relation between laboratory measured turbidity and the [SPM]......40

Figure 17: Derived RGB bands of a water surface image taken at Markiezaatsmeer Lake. The upper panel from left to right is the original image, the red band of the cropped image, the green band of the cropped image and the blue band of the cropped image. The lower panel from left to right is the cropped image, histogram of the red band, histogram of the green band and histogram of the blue band......41

Figure 18: Derived RGB bands of water surface image taken at Hulsbeek Lake. The upper panel from left to right is the original image, the red band of the cropped image,

the green band of the cropped image and blue band of the cropped image. The lower panel from left to right is the cropped image, histogram of the red band, histogram of the green band and histogram of the blue band. 41

Figure 19: Derived RGB bands of water surface image taken at the CDOM dominated pit at Kristalbad artificial wetland. The upper panel from left to right is the original image, the red band of the cropped image, the green band of the cropped image and the blue band of the cropped image. The lower panel from left to right is the cropped image, histogram of the red band, histogram of the green band and histogram of the blue band. 42

Figure 20: Scatter plot of printed grey paper versus original grey card under the shadowed condition, clear sky and sunny condition and for both conditions for the red (R), green (G) and blue (B) bands. The left panel is for the shadowed condition, middle panel for the sunny condition and the right panel for both conditions. 43

Figure 21: Relationship between derived RAMSES $R_{rs}(RGB)$ and smartphone images $R_{rs}(RGB)$ of the studied water bodies. (a) The variation of RAMSES and smartphone images $R_{rs}(RGB)$ with respect to sample sites. (b) The correlation between RAMSES $R_{rs}(RGB)$ versus smartphone images $R_{rs}(RGB)$. 45

Figure 22: The relationship between laboratory measured turbidity and the [SPM], and the red band reflectance of the smartphone images. (a) Smartphone images red band reflectance versus lab measured turbidity. (b) Smartphone images red band reflectance versus lab measured [SPM]. 46

Figure 23: Validation of the original models used by HydroColor APP to estimate turbidity and the [SPM]. (a) Estimates of turbidity through the semi-analytical model of the HydroColor APP versus laboratory measured turbidity. (b) Estimates of the [SPM] through the logarithmic model of HydroColor APP versus laboratory measured [SPM]. The relations were based on all the corresponding red band reflectance of the smartphone images to laboratory measurements. 47

Figure 24: Validation of the original models used by HydroColor APP to estimate turbidity and [SPM]. (a) Estimates of turbidity through the semi-analytical model of HydroColor APP versus laboratory measured turbidity. (b) Estimates of the [SPM] through the logarithmic model of HydroColor APP versus laboratory measured [SPM].

The relations were based on measurements of the red band reflectance of the smartphone images < 0.02 sr^{-1}. 48

Figure 25: Simulation of the estimation of turbidity and [SPM] from the red band reflectance to determine the limitation of the original models used by HydroColor APP. (a) Estimated turbidity versus the red band reflectance. (b) Estimated [SPM] versus the red band reflectance. (c) The 1 NTU : 1 gm^{-3} relation of turbidity and [SPM] applied by HydroColor APP showing an overlap of the two estimated water quality variables. 49

Figure 26: Probability distributions of the derived Nechad model coefficients α_{HS1} and β_{HS1} (upper plots) the slope and intercept of the type II linear regression (middle plots), the MAE and R^2 (lower plots). 51

Figure 27: Probability distributions of the derived logarithmic model coefficients α_{HS2} and β_{HS2} (upper plots) the slope and intercept of the of type II linear regression (middle plots), the MAE and R^2 (lower plots). 52

Figure 28: Validation of the proposed models for the HydroColor APP in estimating [SPM]. (a) Estimated [SPM] of the proposed semi-analytical model of Nechad et al. (2010) versus laboratory measured [SPM]. (b) Estimated [SPM] of the proposed logarithmic model versus laboratory measured [SPM]. The relations were based on measurements of the red band reflectance <0.02 sr^{-1}. 53

Figure 29: Simulation of the estimation of the [SPM] from the red band reflectance to determine the limitation of the proposed models for HydroColor APP. (a) Semi-analytical model of Nechad et al. (2010) estimated [SPM] versus the red band reflectance. (b) The logarithmic model estimated [SPM] versus the red band reflectance. 54

Figure 30: Validation of the proposed models for HydroColor APP in estimating turbidity. (a) Estimates of the proposed semi-analytical model by Nechad et al. (2009) versus laboratory measurements. (b) Estimates of the proposed logarithmic model versus laboratory measurements. The relations were based on measurements of the red band reflectance < 0.02 sr^{-1}. 55

Figure 31: Simulation of the estimation of turbidity from the red band reflectance to determine the limitation of the proposed models for HydroColor APP. (a) Semi-analytical model of Nechad et al. (2009) estimated turbidity versus the red band reflectance. (b) The logarithmic model estimated turbidity versus the red band reflectance. 56

Figure 32: Pie charts of the relative contributions of the error in the models parameters proposed for the HydroColor APP shown as percentages, % with respect to the total error of each model. The upper left panel indicates the errors in % of the Nechad model parameters in estimating [SPM]. The lower left panel indicates the errors in % of the logarithmic model parameters in estimating [SPM]. The upper right panel indicates the errors in % of the Nechad model parameters in estimating turbidity. The lower right panel indicates the errors in % of the logarithmic model parameters in estimating turbidity. 57

Figure 33: Bar charts of the accuracy of the original HydroColor APP models and the proposed HydroColor APP models estimate of turbidity and [SPM] compared to laboratory measurements. The upper left panel indicates the R^2 of the models for estimated [SPM] after validating with lab measured [SPM]. The lower left panel indicates the MAE of the models for estimated [SPM] after validating with lab measured [SPM]. The upper right panel indicates the R^2 of the models for estimated turbidity after validating with lab measured turbidity. The lower right panel indicates the MAE of the models for estimated turbidity after validating with lab measured turbidity. 58

Figure 34: Relationship between RAMSES *xyz* chromaticity coordinates and smartphone images *xyz* chromaticity coordinates. The *x* data is specified by red, *y* data by green and the *z* data by blue. The left panel of the figure, (a) indicates the plot of the *xyz* chromaticity coordinates versus the sample sites. On the right panel, (b) are the scatter plots of the *xyz* chromaticity coordinates of RAMSES versus the smartphone images. 60

Figure 35: Illustration of the xy chromaticity coordinates derived from RAMSES and the smartphone images on a chromaticity diagram. This is compared to the chromaticity coordinates that were developed from laboratory FU solution transmission measurements by Novoa et al. (2013). The white point of the chromaticity coordinate is indicated as WP. 61

Figure 36: Relationship between the hue colour angle $\alpha_P(°)$ and Forel-Ule Index (FUI) derived from RAMSES and the smartphone images. (a) Scatter plot of the $\alpha_P(°)$ derived from RAMSES and the smartphone images with a linear fit (full line) and the 95 % confidence interval (dotted line). (b) Scatter plot of the FUI derived from RAMSES and the smartphone images with a linear fit (full line) and the 95 % confidence interval (dotted line). 62

Figure 37: Deviation, Δ of the smartphone images hue colour angles $\alpha_P(°)$ and Forel-Ule index (FUI) from RAMSES. (a) Derived Δ of the smartphone images $\alpha_P(°)$ with respect to sample sites. (b) Derived Δ of the smartphone images $\alpha_P(°)$ with respect to the original $\alpha_P(°)$ of the smartphone images. (c) Derived Δ of the smartphone images FUI with respect to the original FUI of the smartphone images. (d) Derived Δ of the smartphone images $\alpha_P(°)$ for the sample sites excluding Hulsbeek Lake (36 - 47) in order to derive a model to correct for the deviations of the smartphone images. 64

Figure 38: The relationship between laboratory measured turbidity and the [SPM], and the x chromaticity coordinate from the smartphone images. (a) Smartphone images x chromaticity coordinate versus laboratory measured turbidity (b) Smartphone images x chromaticity coordinate versus laboratory measured [SPM]. 66

Figure 39: Validation of the proposed models for Citclops APP in estimating [SPM]. (a) Estimated [SPM] of the proposed semi-analytical model by Nechad et al. (2010) versus laboratory measured [SPM]. (b) Estimated [SPM] of the proposed logarithmic model versus laboratory measured [SPM]. 67

Figure 40: Simulation of the estimation of the [SPM] from the x chromaticity coordinate to determine the limitation of the proposed models for Citclops APP. (a) Semi-analytical model of Nechad et al. (2010) estimated [SPM] versus the x chromaticity coordinate. (b) The logarithmic model estimated [SPM] versus the x chromaticity coordinate. 68

Figure 41: Validation of the proposed models for Citclops APP in estimating turbidity. (a) The estimated turbidity of the proposed semi-analytical model by Nechad et al. (2009) versus laboratory measured turbidity. (b) Estimated turbidity of the proposed logarithmic model versus laboratory measured turbidity. 69

Figure 42: Simulation of the estimation of turbidity from the x chromaticity coordinate to determine the limitation of the proposed models for Citclops APP. (a) Semi-analytical model of Nechad et al. (2009) estimated turbidity versus the x chromaticity coordinate. (b) The logarithmic model estimated turbidity versus the x chromaticity coordinate. 70

Figure 43: Pie charts of the relative contributions of the errors in the models parameters proposed for the Citclops APP shown as percentages % with respect to the total error of each model. The upper left panel indicates the errors in % of the Nechad model parameters in estimating [SPM]. The lower left panel indicates the errors in % of the logarithmic model parameters in estimating [SPM] The upper right panel indicates

the error in % of the Nechad model parameters in estimating turbidity. The lower right panel indicates the error in % of the logarithmic model parameters in estimating turbidity. 71

Figure 44: Bar charts of the accuracy of proposed Citclops APP models (Nechad and logarithmic) estimates of water quality variables compared to laboratory measurements. The upper left panel indicates the R^2 of the models for estimated [SPM] after validating with lab measured [SPM]. The lower left panel indicates the MAE of the models for estimated [SPM] after validating with lab measured [SPM]. The upper right panel indicates the R^2 of the models for estimated turbidity after validating with lab measured turbidity. The lower right panel indicates the MAE of the models for estimated turbidity after validating with lab measured turbidity. 72

Figure 45: An illustration of derived colour saturation and dominant wavelength from the *xy* chromaticity coordinate on a polar coordinate system, and the deviation, Δ in estimating the difference in a point measured angle θ° and the angle of the corresponding CIE1931 chromaticity coordinate. This illustration is the result of the pit water sampled near Kristalbad artificial wetland. 73

Figure 46: Variation of the colour saturation and dominant wavelength derived from the smartphone images with respect to the sample sites. (a) Colour saturation versus sample site. (b) Dominant wavelength versus sample site. From the Figure, Hulbeek Lake of site 36 – 47 (circled with red full line) gave lower colour saturation and dominant wavelengths within the blue wavelength range because of the clear nature of the water system. 74

LIST OF TABLES

Table 1: Summary of the datasets, tools/protocols, and the quantity of information that was collected from a field campaign and laboratory analysis of water samples. 12

Table 2: Summary of the coefficient of variation, CV of selected wavelengths for the study areas. The wavelengths used are dependent on the TriOS RAMSES-ACC-VIS irradiance sensor. 39

Table 3: Statistical summary of laboratory measurements of water quality variables: [SPM], the concentration of suspended particulate materials; SD, standard deviation; and CV, the coefficient of variation. 39

Table 4: Statistical summary of the variation between RAMSES derived $R_{rs}(RGB)$ and smartphone images derived $R_{rs}(RGB)$. SD, standard deviation; CV, coefficient of variation; PE, percentage error. 44

Table 5: Statistical summary of the variation between RAMSES derived *xyz* chromaticity coordinates and smartphone images derived *xyz* chromaticity coordinates. SD, standard deviation; CV, coefficient of variation; PE, percentage error. 59

Table 6: Statistical summary of the hue colour angles, $\alpha_P(°)$ and Forel-Ule Index (FUI) derived from RAMSES and the smartphone images. SD, standard deviation; CV, coefficient of variation; PE, percentage error. 61

Table 7: Statistical summary of the deviation, Δ of smartphone images hue colour angle $\alpha_P(°)$ and Forel-Ule index (FUI) from RAMSES. 63

Table 8: Visual comparison of the pit water smartphone image $\alpha_P(°)$ and FUI to the $\alpha_W(°)$ and FUI generated using RGB values of Wernand et al. (2013) and the $\alpha_N(°)$ and FUI of laboratory FU solution transmission by Novoa et al. (2013). The FUI is calculated based on the $\alpha_P(°)$. For example, the $\alpha_P(°)$ of the smartphone image was 36.896°. Base on Novoa et al. (2013) this angle is < 39.769°. The smartphone image is this indexed 17. Also, Base on Wernand et al. (2013) this angle is < 39.674°. The point measured RAMSES data is this indexed 21. 65

Table 9: Statistical summary of the colour saturation, dominant wavelength and the deviation, Δ in estimating the difference in a point measured angle θ° and the angle of the corresponding CIE1931 chromaticity coordinate. SD, standard deviation; CD, coefficient of variation. 74

NOTATIONS

$a(\lambda)$	Bulk absorption coefficient (m^{-1})
a_CDOM	Absorption of coloured dissolved organic materials (m^{-1})
$b_b(\lambda)$	Bulk backscattering coefficient (m^{-1})
$E_d(\lambda)$	Downwelling irradiance ($Wm^{-2}nm^{-1}$)
$E_{ill}(\lambda)$	Illumination spectrum ($Wm^{-2}nm^{-1}$)
$L_{rel}(\lambda)$	Relative radiance ($Wm^{-2}nm^{-1}sr^{-1}$)
$L_u(\lambda)$	Upwelling water surface radiance ($Wm^{-2}nm^{-1}sr^{-1}$)
$L_{sky}(\lambda)$	Downwelling sky radiance ($Wm^{-2}nm^{-1}sr^{-1}$)
$R_{sfc}(\lambda)$	Water surface reflectance (sr^{-1})
$R_{rs}(\lambda)$	Remote sensing reflectance (sr^{-1})
α	Camera exposure time (s)
μ	Mean of observations
θ	Angle (degree)
$\rho_{air\text{-}water}$	Sun-sky glint correction coefficient at the air-water interface
σ	Standard deviation of observations
Δ	Deviation of observations
Σ	Summation of observations
$\int$	Integration of observations

ABBREVIATIONS

APP	Application
ILWIS	Integrated Land and Water Information System
IOP	Inherent Optical Properties
SIOP	Specific Inherent Optical Properties
CDOM	Coloured Dissolved Organic Materials
CET	Central European Time
CIE	Commission Internationale d'Eclairage
CMF	Colour Matching Function
CV	Coefficient of Variation
CVRL	Colour and Vision Research Laboratory
FUI	Forel-Ule Index
FUME	Forel-Ule MERIS
GeoCalVal	Calibration and Validation of Geophysical Observations
GF/F	Glass Fiber/Filter
GPS	Global Positioning System
Lab	Laboratory
MAE	Mean Absolute Error
NTU	Nephelometric Turbidity Unit
PD	Probability Distribution
PE	Percentage Error
RAMSES	Radiation Measurement Sensor with Enhanced Spectral Resolution
RGB	Red, Green and Blue channels of an image
RMSE	Root Mean Square Error
R^2	Determination Coefficient
SD	Standard Deviation
[SPM]	Concentration of Suspended Particulate Materials
UV	Ultra Violet
WACODI	Water COlour from Digital Images
WP	White Point

1. INTRODUCTION

1.1. Research Background

Water is an abundant liquid which continuously recycles as it moves on, above and under the earth's surface (Bethea, 2011). Although the amount of water in the earth system does not change, global climate changes greatly affect the distribution pattern of water and, therefore, dictate its availability and usability (Dore, 2005). As the water reaches the surface of the earth, its quality degrades because it encounters and picks up many pollutants along its path (Ouyang et al., 2006; Verma, 2009). The water quality, therefore, varies from place to place, with the seasons, and with the type of rocks and soils which it moves through (Centre for Affordable Water and Sanitation Technology, 2008). In addition to these influence from nature, pollution and contamination caused by humans have greatly compromised the quality of available water. The increased pollution and contamination of small water bodies has raised a global concern (United Nations, 2002). The fear is that if we do not address the quality problems now, there will be quantity problems in the near future due to the fact that we may render most of our water bodies unusable. To monitor the quality of the water bodies, McGrath & Scanaill (2014) conclude that in addition to traditional laboratory analysis, new technologies are needed to provide real-time information. Over the years, such ideas are growing into reality as more instruments are enabled with remote sensing capabilities for monitoring water quality.

The remote sensing of water quality can be simply accomplished by; observing the colour of water to quantify suspended and dissolved materials in the upper layer of the water. Colour can be represented and therefore measured either in the colour space (image capture by a smartphone's camera) or in the frequency space (that is, spectrum). Radiometers on satellites that observe the earth measure water leaving spectra. Bio-optical models are then applied to establish the relationship between water surface reflectance and optically significant water constituents through empirical models (O'Reilly et al., 1998) or to their optical properties through semi-analytical inversion models (Maritorena et al., 2002). In applying these models, water quality variables such as phytoplankton pigments, suspended particulate matter and dissolved organic matter can be estimated (Gordon et al., 1988; Lee et al., 2002) as cited in Chang and Gould (2006).

The use of satellites and other airborne platforms with radiometric sensors have shown remarkable results in the field of water quality remote sensing for the oceans and larger inland water bodies for decades now (Qihao, 2011). Notwithstanding, there are still quite a number of challenges with satellite observations. For example; long revisit time, low spectral resolution, and inability to easily access and interpret data. Alternatively, the value of smartphones as tools for water quality monitoring has thus been recognised with applications (APPs) developed to derive water quality variables from them. For example; Algae Watch – for algae monitoring (Kotovirta et al., 2014); Citclops, now called EyeOnWater – for water colour (Novoa et al., 2014); HydroColor – for water turbidity, [SPM] and backscattering coefficient in the red (Leeuw, 2014); and pesticides detection using pictures taken of test strips (Sicard et al., 2015). Some smartphone APPs also require the phone to be linked to an external sensor (Haklay, 2013). For example; the iSitu water monitoring APP connects to a handheld instrument for collecting water quality and quantity data (In-Situ Inc., 2013). Smartphone APPs have also been developed and sited in a number of scientific fields such as; Creek Watch – for waterways monitoring, (Kim et al., 2011); air quality (Kim & Paulos, 2010); noise pollution (Maisonneuve et al., 2010); and healthcare management (Aitken & Gauntlett, 2013).

Globally, there are nearly 7 billion mobile phone subscriptions (accounting for 95.5 % of the world's population) according to the International Telecommunication Union (2014) report with 4.5 billion mobile users (Ericsson, 2014). As mobile technologies continue to advance, it is estimated that by 2020, about 70 % of the world's population will be using smartphones (Ericsson, 2015). Day in day out, more functionality is integrated into smartphones to make access to information easier through the use of APPs. Thus, smartphone APPs are becoming increasingly prevalent across mobile phone users (Lim, 2015). The number of APPs downloads had grown from 10 billion downloads in 2010 to 77 billion by 2014 (Bilbao-Osrio et al., 2014). As this trend continues and people become more interested in environmental monitoring APPs, participatory sensing would become prominent in producing scientifically meaningful observations.

The use of smartphone APPs for water quality monitoring by citizens might finally be the breakthrough in achieving real-time water quality monitoring to complement laboratory analysis. In the light of this, it would not only be beneficial for citizens to be able to know the quality of their water but can also be enabled to serve as water quality alert systems and/or further developed to serve as national monitoring networks and generate water resource databases (Chapman, 2002; Su et al., 2011). Quite apart, over a century's data on Forel-Ule (FU) index classification of global water bodies if added to existing and forthcoming data from the Citclops APP can facilitate the interpretation of long-term water colour data series valuable for climate-related studies (Novoa et al., 2013). With such anticipated innovative usage, there is the need to know the efficiency and accuracy of measurements from upcoming water quality monitoring APPs.

1.2. Problem Statement

The human society has become very cautious and curious about their environment. Non-scientists thus volunteer to participate in data collection and analysis to better understand their environment and what they consume. Monitoring and sensor platforms are therefore shifting toward empowering citizens with the capabilities to collect and share information about their environment. Devices and applications that extend the theory of quantified self into the living environment according to McGrath & Scanaill (2014) therefore will continue to evolve. Business Communications Company Report (2014), thus projects the global market for environmental sensing and monitoring to be valued at nearly $17.6 billion USD by 2019, with a compound annual growth rate of 5.9 %.

Water monitoring sensors have to be of great concern as water forms an essential environmental component and a central element of life. Deteriorated water quality poses a threat to both humans and the environment. Innovative long-term water monitoring initiatives, therefore, have the potential to see increased investment in large-scale, from the scientific and societal realm as water quality demand, continue to increase (Corke et al., 2010). With near real-time analysing capabilities, innovative technologies in optical remote sensing of water quality are gradually enabling sensing technologies to move from the laboratory into world use in time and space (Banna et al., 2014). A novel in such areas is the use of smartphone APPs to quantify some water quality variables. Currently, there are two of such APPs (Citclops and HydroColor) in

APPs stores. Cameras on smartphones are used to take RGB colour composite of water upper layer. These APPs within a smartphone then apply specific models to derive *xyz* chromaticity coordinates for Citclops and remote sensing reflectance RGB for HydroColor. These are subsequently used to index and/or quantify water quality variables from the image. These two APPs use different transfer functions in converting RGB to spectrum. There has been no research on their efficiency and accuracy of measurements in relation to their transfer functions. For effective monitoring and decision making to be made on water bodies from these smartphone APPs, there is the need to evaluate the efficiency and accuracy of their measurement.

1.3. Research Objective

Although the two APPs (Citclops and HydroColor) use the same RGB camera input, they employ different transfer functions in converting RGB to spectrum and hence water quality variables of; colour, turbidity and [SPM]. The research objective is, therefore; to evaluate the efficiency and accuracy of these two approaches to deriving these water quality variables.

1.4. Research Questions

1. How accurate are the retrieved spectra from smartphones RGB images compared to hyperspectral observations?
2. How accurate is the retrieved water quality variables from the APPs compared to laboratory measurements?
3. Which approach is recommended for use in inland water in the Netherlands?

2. LITERATURE REVIEW

2.1. Colour Vision

The theory of colour is bound by the spectral power distribution of light rays over the visible spectrum. Light from an object is thus perceived in the wavelength region 380 to 780 nm over the electromagnetic spectrum (Klein, 2010). Depending on the objects surface, the spectrally reflected light may be altered. This does not only affect the reflected light but also information of the light source and the subsequent impression of the object's colour (Reinhard et al., 2014). According to Wyszecki (2006), the human eye can approximately distinguish 10 million different colours. To perceive these colour differences, the human eyes only used three receptor cones in the retina. Each of these receptors responds differently to the light waves in the visible spectrum. These receptors thus send only three signals to the brain to interpret the perceived object depending on the signal intensities.

Colour perceived by human is therefore not a physical quantity that can be measured by engineering applications but a psychophysical response to light energy interpreted by the brain from the signal transmitted by the cones (Klein, 2010). However, these responses can be engineered by using three numbers to represent the cone's signals. Just like the human eyes, three numbers can be used to represent the visible spectrum for any optically sensing device. According to Reinhard et al. (2014) *"the field of colourimetry has, therefore, being concerned with assigning numbers to physically defined stimuli such that stimuli with the same specification look alike (that is, match)"*.

2.2. Colour Space

Colour appearance of objects measured by devices is represented using the principle of the three cone responses of the human eye. The colour presentation of objects can, therefore, be said to be based on the theory of trichromacy which states that *"Any colour can be formed by combining three properly chosen primary colours"* (Cotton, 1995). Relying on the additive nature of the trichromacy theory, the red (R), green (G) and blue (B) primary colours form the basis for the colour organisation in devices.

In an attempt to classify perceived colour of objects, colour space has been specified for different devices. A common colour space used by devices is the RGB colour space. For image capturing devices, the RGB colour of an image is dependent on the $R(\lambda)$, $G(\lambda)$ and $B(\lambda)$ sensitivity functions of the device and the spectral power distribution of incoming light $S(\lambda)$ over the visible spectrum as indicated in Eq. (1 – 3) (Tkalcic & Tasic, 2003).

$$R = \int_{380}^{780} S(\lambda)R(\lambda)d\lambda \tag{1}$$

$$G = \int_{380}^{780} S(\lambda)G(\lambda)d\lambda \tag{2}$$

$$B = \int_{370}^{780} S(\lambda)B(\lambda)d\lambda \tag{3}$$

The RGB colour of an image in an RGB colour space would, therefore, vary from device-to-device since image capturing devices have different sensitivity functions. The RGB of an object as stated earlier would also vary with changing illumination condition.

In order for everyone to use the same specification of colours, a standard colour space known as the XYZ colour space was set by the Commission Internationale d'Eclairage (CIE) in 1931 (CIE, 2004). By this, no matter the variation in objects colour observed by different devices or perceived by different viewers, the objects colour can be described using the CIE standard XYZ tristimulus values. The CIE XYZ colour space therefore does not depend on the device used (Tkalcic & Tasic, 2003). The resulting produce from the XYZ colour space such as the chromaticity coordinates is also illumination independent. This makes such a colour space a good colour space to be used for objects colour of image capturing devices.

2.3. Water Colour

In an open water system, light from a given source is either absorbed or scatter by water molecules and order materials within it. The result of this phenomenon is the reflected light that comes to our sight to be interpreted as the colour of the water. The colour of water is thus related to its inherent optical properties (IOPs); absorption $\alpha(\lambda)$ and backscattering $b_b(\lambda)$ (IOCCG, 2006). A water molecule by itself has specific IOPs at explicit wavelengths. Variation of water colour therefore depends on the concentration level of particulate and dissolved water constituents. This results in the variation of the light signal intensity received by the human eye or a device. However, other secondary processes such as fluorescence by dissolved organic matter and phytoplankton pigments, and Raman scattering by water molecules may account for the colour of a water system (Stramski et al., 2004). The apparent colour (the colour of the water system as a whole) or the true colour (the colour obtained after filtering the water to remove all suspended material) have thus been used as a measure of water colour and its associated particulate and dissolved constituent's concentration.

2.4. Remote Sensing of Water Quality

Remote sensing of water quality is the quantification of the concentration of particulate and dissolved water constituent using the apparent colour of the upper layer of a water system perceived by the human eye or observed by remotely sensing device.

In an attempt to quantitatively assess the physics of water colour using remote sensing devices, optical closure relationships have been developed to relate the observed signal (remote sensing reflectance $R_{rs}(\lambda)$) to the IOPs of water molecules and its associated constituents. According to Lambert-Beer's law as sited in Salama et al. (2009), the IOPs of a water system are linearly proportional to the water constituent's concentrations and the specific inherent optical properties (SIOPs) of the water. The quantification of particulate and dissolved materials can, therefore, be obtained from the IOPs and SIOPs of a water system by remotely sensing its apparent colour. Remote sensing has thus been used as a tool to monitor the quality of water bodies especially through satellite and other airborne platforms.

2.5. Water Quality Variables

To determine the suitability of water for consumption, a number of water quality variables are checked. Common among them include; colour, [SPM] and turbidity. The [SPM] relates to the amount of suspended organic and inorganic materials within a given water column. Turbidity is related to light attenuation effect induced by the presence of [SPM]. The degree of light attenuation, therefore, determines the turbid nature of the water concerned. Water quality variables for this study have been limited to colour, turbidity and [SPM].

3. STUDY AREA AND DATA SET

3.1. Study Area

The research was carried out using four surface water resources (three lakes and an artificial wetland) in the Netherlands. The first two lakes, Binnenschelde and Markiezaatsmeer are neighbouring water bodies located southwestern of the Netherlands as shown in the Google Earth map of Figure 1. These lakes are located in the provinces of Zeeland and North Brabant. They shear boundary with the Reimerswaal Municipality to the north, Hulst Municipality to the south of Zeeland Province, Bergen op Zoom Municipality to the east of North Brabant Province and Scheldt-Rhine Canal to the west.

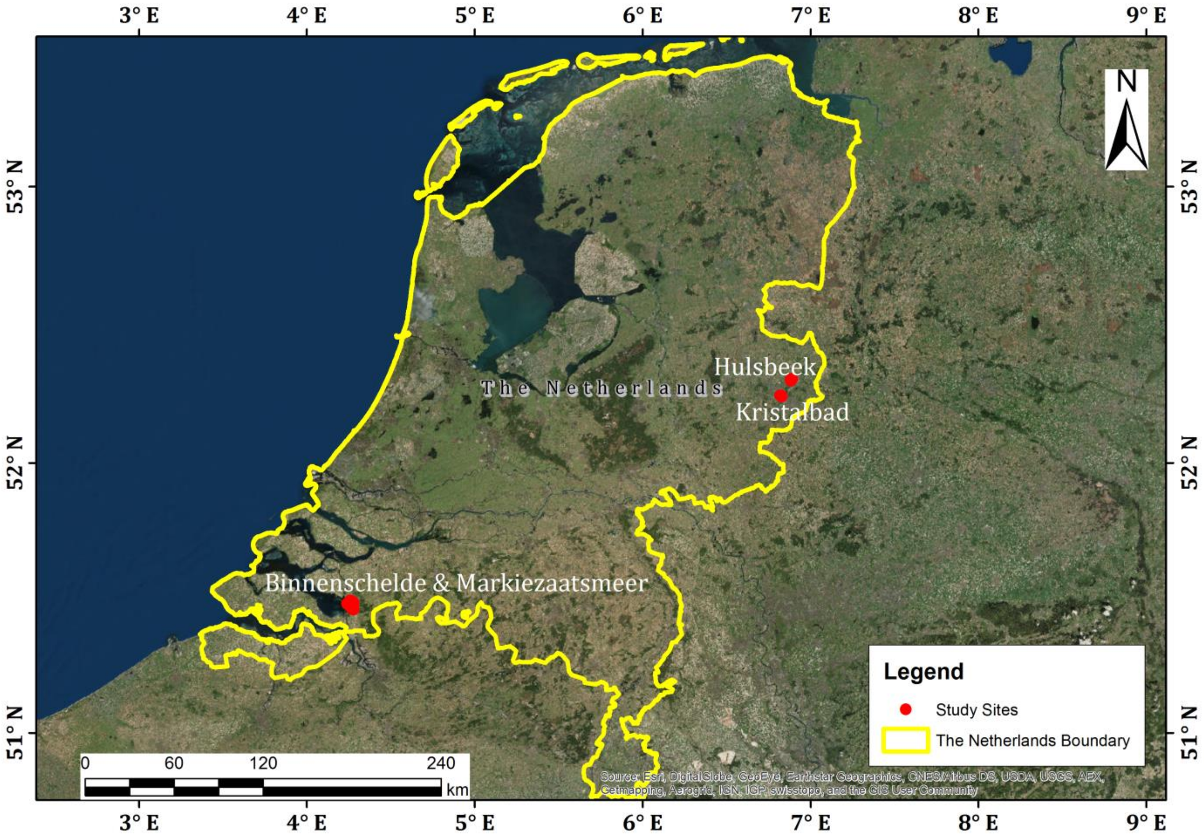

Source: Esri, DigitalGlobe, GeoEye, Earthstar Geographics, CNES/Airbus DS, USDA, USGS, AEX, Getmapping, Aerogrid, IGN, IGP, swisstopo, and the GIS User Community

Figure 1: Google Earth map showing the overlaid study sites (red dots) in the Netherlands country boundary (yellow line).

The second phase of the study was at Hulsbeek Lake and Kristalbad artificial wetland shown on the Google Earth map of Figure 1. These two surface water resources are located in the eastern part of the Netherlands within the Province of Overijssel. Hulsbeek Lake is located in the western part of Oldenzaal Municipality. Kristalbad artificial wetland shears boundary with Enschede Municipality to the west and Hengelo Municipality to the east.

3.1.1. Binnenschelde Lake and Markiezaatsmeer Lake

The delta region of the Southwest Netherlands has been threatened over the past years with flooding from the sea. Systems of dams, locks and other infrastructures have therefore been constructed to separate salt, brackish and fresh waters in an attempt to control the water. Haas & Tosserams (2001) in their research this concluded that the once dynamic environmental estuary abundant with a high degree of natural dynamics and productivity had to give way to secluded basins. Out of this development, the Oosterschelde Estuary had undergone a number of changes which resulted in the creation of Markiezaatsmeer Lake and Binnenschelde Lake. Both lakes are weak brackish water; as a result of dilution from precipitation after its separation from the Oosterschelde Estuary.

The Markiezaatsmeer Lake is centred at latitude 51.469119N and longitude 4.249778E. It is separated from the Oosterschelde Estuary by the Scheldt-Rhine Canal. The lake has a water surface area of about 18,000,000 m^3 and 3,900,000 m^3 of marshes. It has an average depth of 2.1 m and a maximum depth of 3.0 m. Its soil is said to have been transformed from Pleistocene to Holocene soils; a unique situation that is rarely found (Tosserams et al., 2001).

On the other hand, the Binnenschelde Lake is centred at latitude 51.487187N and longitude 4.264198E. It is a relatively small lake that borders the residential area of Bergen op Zoom and separated from Markiezaatsmeer Lake by a dike. The lake has a water surface area of about 1,780,000 m^3. Also, it has an average depth of 1.5 m and a maximum depth of 3.5 m. The lake is principally used for recreational activities.

The key challenge in both water bodies has being its quality. Since 1996, the concentration of nitrogen and phosphorus compounds are said to be much higher than the national limits (Withagen, 2000). The phosphorus compounds are attributed to the seabed and the nitrogen to precipitation. This high concentration of nutrients in the water has led to excessive algae growth occasionally observed in the summer. The eutrophic conditions and the small size of these lakes make them suitable study areas to assess the quality and benefits of smartphone APPs in water quality monitoring. A map of the study area showing Binnenschelde and Markiezaastmeeer Lakes with their sampled points is as shown in Figure 2.

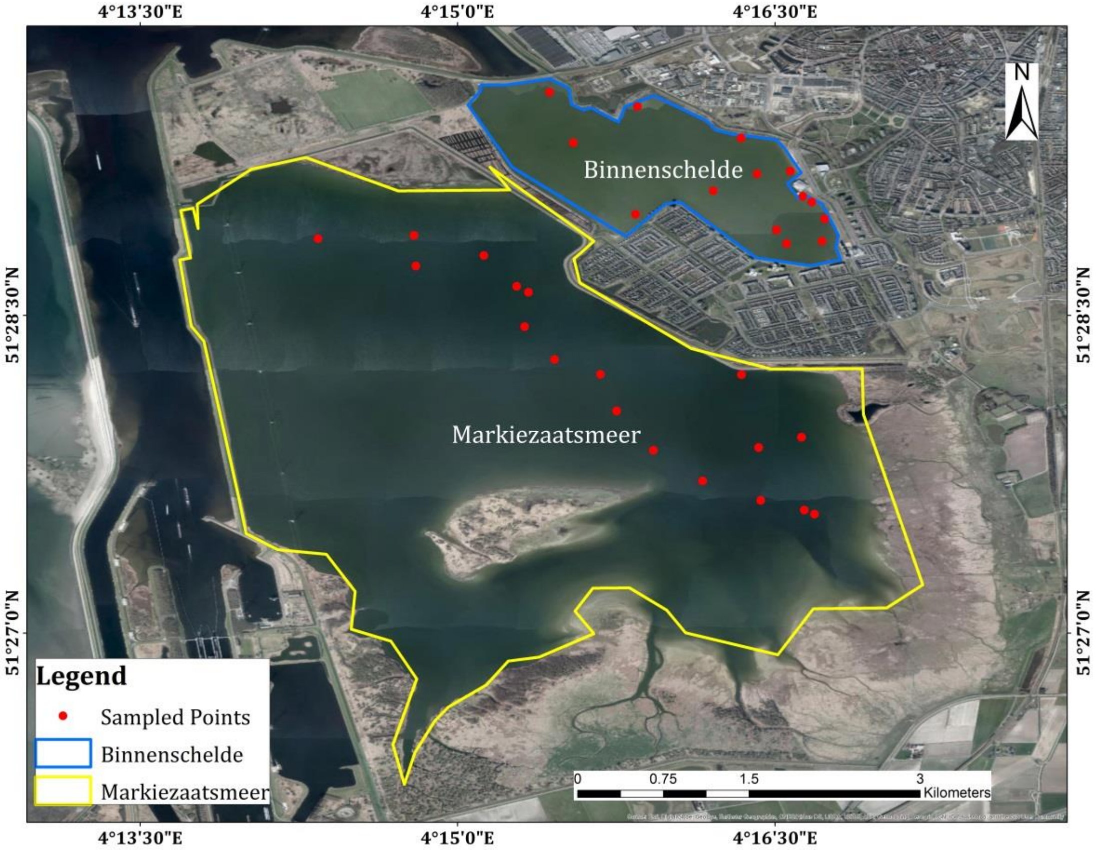

Figure 2: Google imagery map showing Binnenschelde Lake (blue boundary line) and Markiezaatsmeer Lake (yellow boundary line) with overlaid sampled points (red dots).

3.1.2. Hulsbeek Lake and Kristalbad Artificial Wetland

The increasing value of leisure times by the Dutch is often evident in recreational facilities spotted at various sections of their cities. A prominent figure of such facilities is water bodies. Lakes such as Hulsbeek are thus purposely created for recreational activities. Furthermore, even the creation of Kristalbad artificial wetland as a waste water treatment system has part of its landscape serving an ecological corridor and recreational area.

Hulsbeek Lake is centred at latitude 52.181464N and longitude 6.531025E. It is one of the top three recreational lakes visited in the Province of Overijssel used for swimming, surfing and other water sports (Abbenhues, 2003). It has a surface area of about 250,000 m^3 and a maximum depth of 6 m. A map of the study area showing Hulsbeek Lake with the sampled points is as shown in Figure 3.

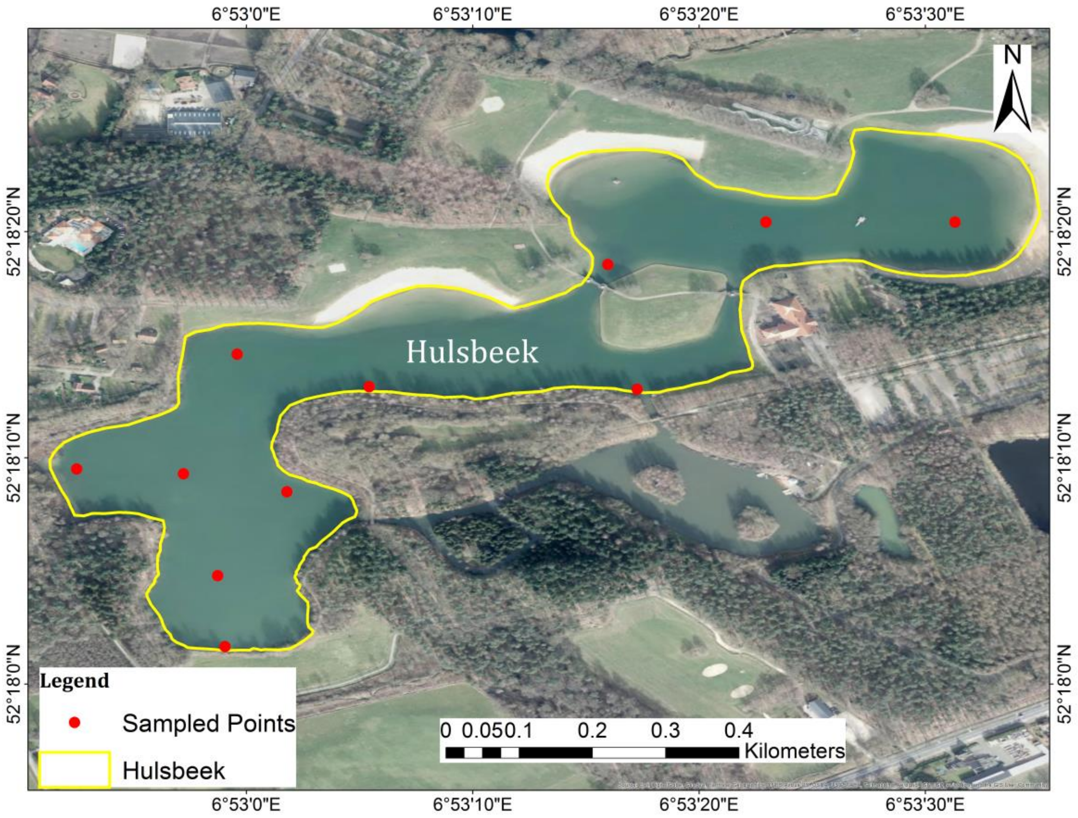

Figure 3: Google imagery map showing Hulsbeek Lake (yellow boundary line) with overlaid sampled points (red dots).

Kristalbad, on the other hand, is an artificial wetland centred at latitude 52.244297N and longitude 6.823907E. It is a wetland for further biological treatment of waste water effluent from the waste water treatment plant of Enschede. It has a total surface area of about 400,000 m^3 with 187,000 m^3 of the area used for water storage. A map of the study area showing Kristalbad artificial wetland with the sampled points is as shown in Figure 4.

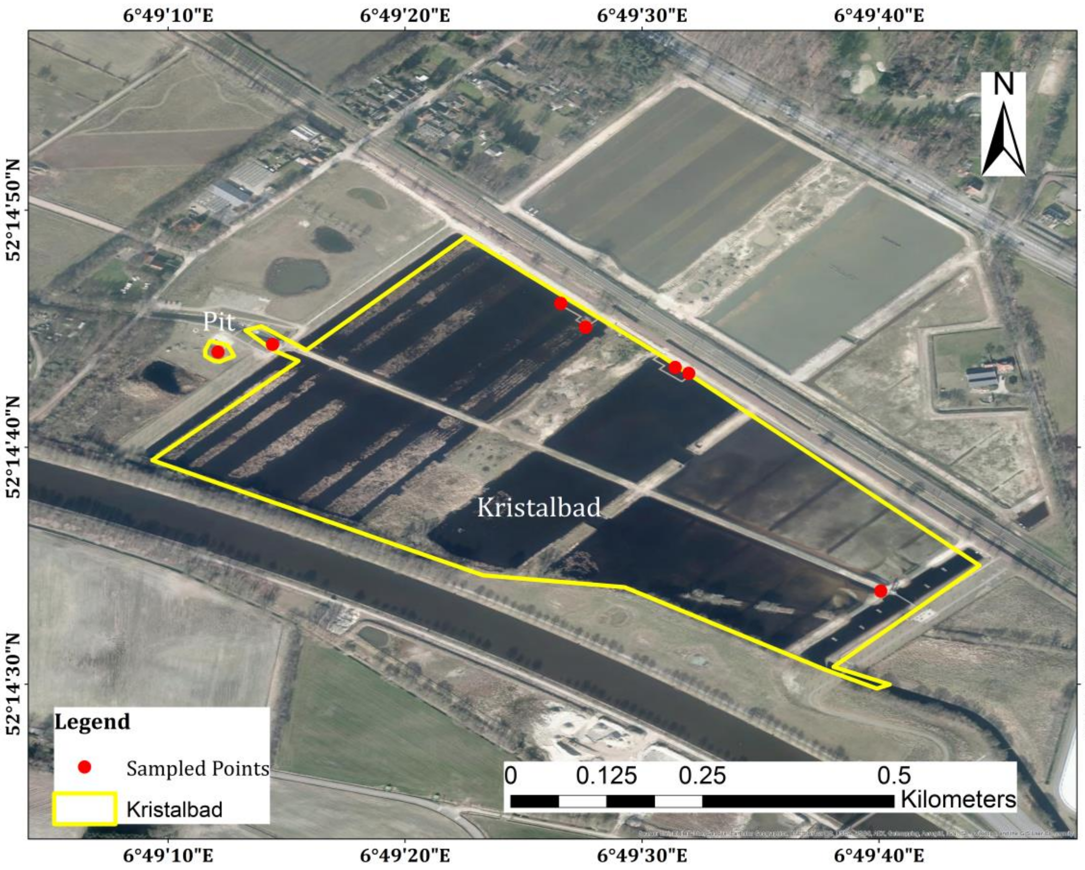

Figure 4: Google imagery map showing Kristalbad artificial wetland (yellow boundary line) with overlaid sampled points (red dots).

3.2. Data Set

A summary of the data sets that were taken on a field campaign and laboratory measurements is as shown in Table 1.

Table 1: Summary of the datasets, tools/protocols, and the quantity of information that was collected from a field campaign and laboratory analysis of water samples.

Data		Tool/Protocol	Quantity
Field Measurements			
Smartphone APP	Citclops	Samsung Galaxy S4 GT-i9515. Alcatel One Touch 7041D.	sRGB of water surface images.
	HydroColor	Samsung Galaxy S4 GT-i9515. Alcatel One Touch 7041D.	sRGB images of water surface, sky, grey card, and printed grey paper (in place of the grey card when absent).

Hyperspectral sensors	TriOS RAMSES-ACC-VIS irradiance sensor.	Sky-sun downwelling irradiance.
	TriOS RAMSES-ACC radiance sensor.	Water leaving radiance. Sky downwelling radiance.
Laboratory Analysis		
Water samples	Turbidimeter	Turbidity
Water samples	Gravimetric method	Concentration of suspended particulate materials [SPM]

3.3. Optical Field Measurement

A field campaign was organised on the 24th, 25th and 28th of September, and 1st of October, 2015 for Binnenschelde, Markirzaatmeer, Hulsbeek, and Kristalbad respectively. The sampling technique used was a random sampling. For the lakes, measurements were taken at various sections across the lakes using boats and for the wetland at its edges since there was no boat. Measurements commenced from 12:00 to 15:06 CET for Binnenschelde Lake with overcast clouds and wind. Measurements at Markirzaatmeer Lake started at 10:09 to 13:30 CET with scattered clouds, fluctuating the sunshine and relatively small wind condition. Measurements at Hulsbeek Lake started at 11:41 to 12:47 CET with no sunshine, no wind and about 60-90 % of cloud cover. Measurements at Kristalbad artificial wetland started at 11:21 to 13:24 CET with clear sky and sunshine, and gentle wind. In all, 53 measurement sites were visited with distance ranging from 50 – 1000 m. At each station, measurements carried out include; hyperspectral sensors measurements, smartphones measurements and some water quality indicators as shown previously in Table 1.

The hyperspectral sensor measurements include; TriOS RAMSES-ACC-VIS irradiance sensor and TriOS RAMSES-ACC radiance sensor. The two sensors were first used to take measurements instantaneously for downwelling sun-sky irradiance and upwelling water radiance. For Markirzaatmeer Lake and Kristalbad artificial wetland, the TriOS RAMSES-ACC radiance sensor was later used to take a measurement for the sky radiance considering its fluctuation weather condition and sunny condition respectively. Underwater downwelling, irradiance and upwelling radiance were also taken at two different depths (10 and 20 cm) from the water surface.

Measurements with the smartphone included the use of two different phones to take images using the Citclops APP and HydroColor APP. The main smartphone of which data was required for analysis was the Samsung S4. The Alcatel Onetouch Pop 7, on the other hand, was used as a back-up in case the Samsung S4 failed. Measurements were first taken using the Alcatel Onetouch Pop 7 followed by Samsung S4 for Citclops APP and HydroColor APP respectively. With the Citclops APP on the Alcatel Onetouch Pop 7, images of the water surfaces were taken at 15° - 35° viewing angle and 2° - 353° azimuth angle. The general procedure as described in Annex II was followed by comparing the water surface image to the digitised FU scale. This was followed by selecting the corresponding colour, information patterning the weather condition at that moment and visibility of the water bottom. The measurements on completion were then saved and sent to the Citclops database to be processed. For the HydroColor APP, following the instructions as described in Annex III, the grey card, water surface and sky images were taken at zenith angles 35° - 42°, 38° - 43° and 127° - 135° respectively. Upon completing the measurements for the APP, information of the water quality was then processed and displayed immediately.

Water quality variables of pH, dissolved oxygen and temperature were also measured using an HQ40d portable multimeter with two probes. Water samples were then collected at selected points in 2 L sampling bottles wrapped in aluminium foil to prevent light interaction with the water samples. This was to prevent the degradation of the phytoplankton in the water samples (Aminot & Rey, 2000). Also, 3 - 6 drops of Magnesium Hydroxy Carbonate $(4MgCO_3).Mg(OH)_2.5H_2O$ was added to prevent degradation of the water samples. The water samples were then refrigerated at 5°C after which they were analysed for turbidity and [SPM].

In two of the field campaigns (Binnenschelde and Hulsbeek Lakes), a printed grey paper was used in place of a grey card. Thus, the printed grey paper measurements needed to be corrected. Measurements were therefore taken off the printed grey paper and the grey card using the hyperspectral sensors and the smartphones. First, the measurements were taken in a sunny condition and second in a shadowed condition. For each of the cards, five measurements were taken from the devices used.

3.4. Laboratory Analysis

Water sampled from the field were analysed in the laboratory of the Faculty of Geo-information Science and Earth Observation of the University of Twente.

3.4.1. Turbidity

Turbidimeter of model 2100P was used for measuring the turbidity of the water samples as described in the instrument manual of Hach, (2008). The instrument was first calibrated using the Gelex secondary turbidity standards of known turbidity values shown in Figure 5.a. Raw water samples were then poured into the turbidimeter sample cells of Borosilicate glass with screw caps to 2/3 (that is, approximately 15 mL) of its volume. The sample cells were then placed into the cell compartment to analyse each sample. Each sample measurement was then recorded in Nephelometric Turbidity Unit (NTU) as shown in Figure 5.b.

Figure 5: Instrumental set-up, calibration and measurement of turbidity. (a) Gelex secondary turbidity standards of know turbidity values. (b) Turbidimeter reading in NTU of the measured water sample.

3.4.2. Suspended Particulate Materials (SPM)

Whatman's glass fibre filters (GF/F) of 0.7 μm were pre-weighed on an electronic balance of accuracy 10^{-4} g shown in Figure 6.a. 25 mL of water samples were then filtered through these filters to retain the total suspended materials using a low vacuum pump. At least 5 mL of distilled water was then filtered through the filtration apparatus to dissolve and remove any salt or dissolvable material. The filter papers were then placed on a petri dish and oven dried at a temperature of 105°C for 20-24 hours as shown in Figure 6.b. The final weight of the filter paper was then taken after oven drying. The concentration of SPM ([SPM]) was then obtained by subtracting the initial weight from the final weight of the filter paper and dividing by the volume of the water sample used as shown in Eq. (4) (Tilstone et al., 2003).

$$[SPM] = \frac{Final\ weight\ (g) - Initial\ weight\ (g)}{Volume\ of\ water\ sample\ filtered\ (mL)} \tag{4}$$

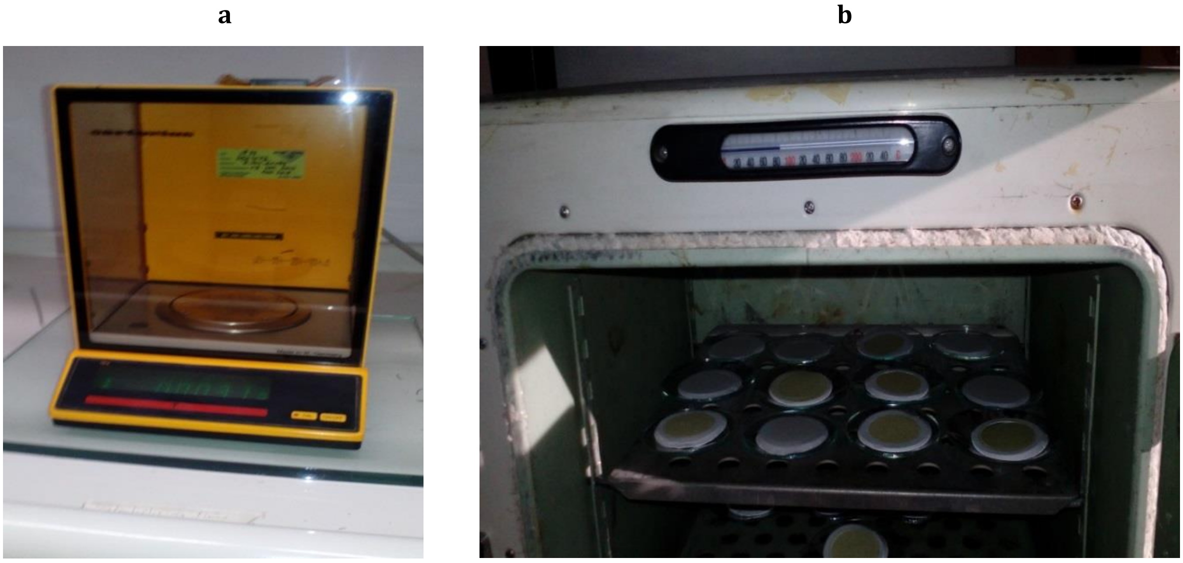

Figure 6: Instrumental set-up for the measurement of suspended particulate materials SPM. (a) Electronic balance used for measuring the weight of the filter papers. (b) Oven drying of the filter papers containing total suspended materials after filtering the water samples.

4. RESEARCH APPROACH AND METHODOLOGY

4.1. Summary of Data Analysis and Flow Chart

The research was designed to meet the objective of the study. By this, the field collected data sets were analysed. The flow chart for the research is as shown in Figure 7. The field measurements of the hyperspectral sensors hereafter referred to as RAMSES were first used to derive remote sensing reflectance $R_{rs}(\lambda)$. The $R_{rs}(\lambda)$ of RAMSES were then used to derive xyz chromaticity coordinates for Citclops APP assessment and also $R_{rs}(RGB)$ for HydroColor APP assessment. Smartphone images from the Samsung Galaxy S4 GT-i9515 through the HydroColor APP were used in the subsequent derivations. For the Citclops APP analysis, the field captured smartphone images were converted to the XYZ colour space from which the xyz chromaticity coordinates, hue colour angles $\alpha_P(°)$ and subsequently Forel-Ule indexes FUIs were derived. The xyz chromaticity coordinates, $\alpha_P(°)$ and FUIs of the smartphone images were then compared to the xyz chromaticity coordinates, $\alpha_P(°)$ and FUIs derived from RAMSES. The x chromaticity coordinate of the smartphone images was subsequently used to derive turbidity and [SPM] for the point measurements by using a single band semi analytical model and a logarithmic model as a pilot study. Regression analysis was then used to compare these estimated water quality variables to laboratory measurements. The limitations of the models were then determined by varying the models' parameters (that is, their coefficients and the x chromaticity coordinate). Errors in the estimation of the water quality variables using the proposed models parameters were then quantified. The xy chromaticity coordinates were also then used to derive the colour saturation as a measure of transparency for the point measurements. For the HydroColor APP, the field captured images on deriving their RGB bands were converted to $R_{rs}(RGB)$ and compared to the $R_{rs}(RGB)$ derived from RAMSES data. The $R_{rs}(RGB)$ of the APP results were also then used to derive water quality variables based on specified models of the APP and compared to laboratory measurements. A logarithmic and semi-analytical model were then used to derive water quality variables and compared to laboratory measurements. Limitations of the original model used by HydroColor APP and the proposed models parameters were then turned to determine the limit of their turbidity and [SPM] estimates. Errors were then quantified from the models parameters.

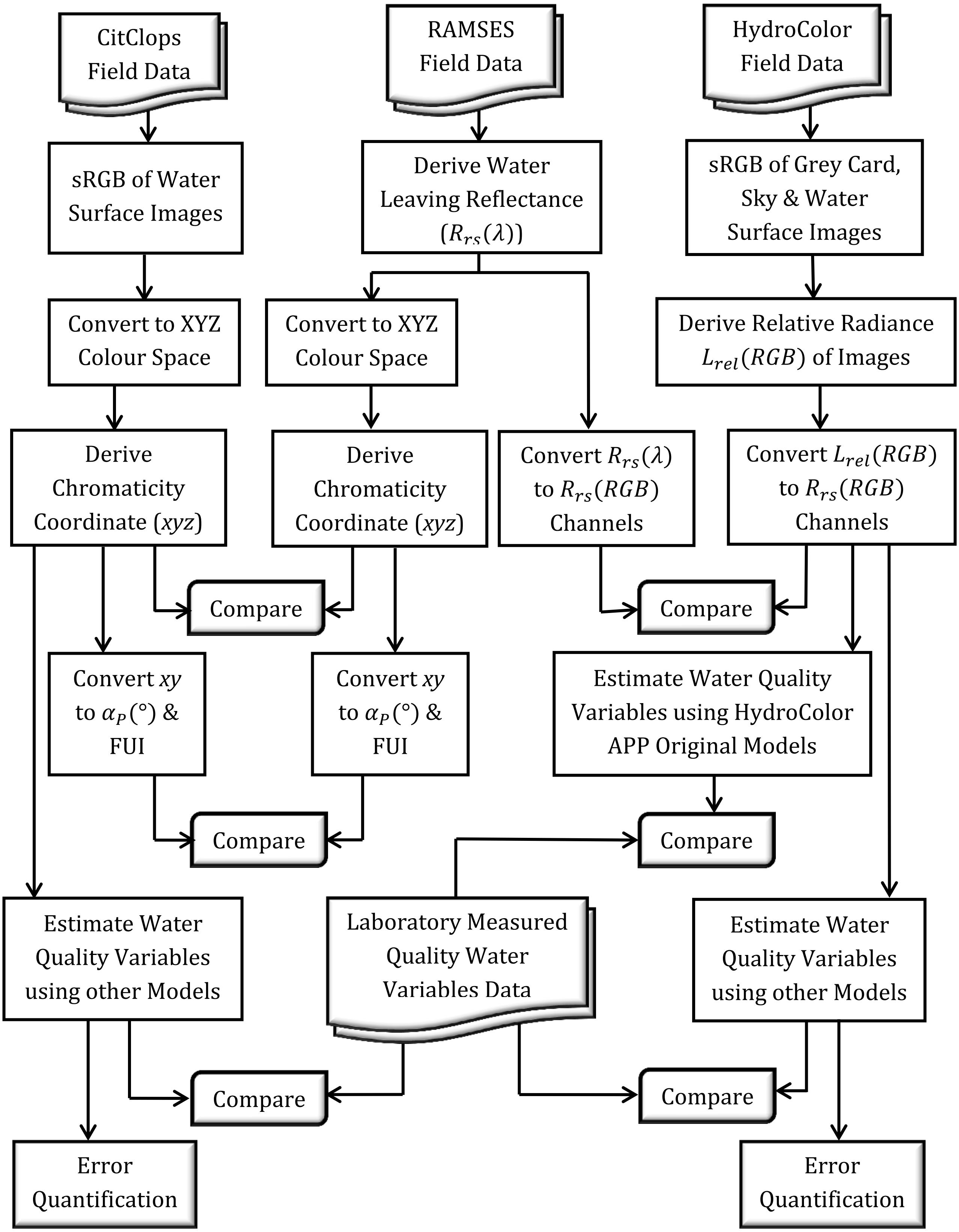

Figure 7: Flow chart of the research work; Citclops and HydroColor APPs assessment using hyperspectral sensors (RAMSES) and laboratory measurements.

4.2. Deriving Remote Sensing Reflectance

The field hyperspectral measurements of RAMSES were used to derive the remote sensing reflectance of the upper layer of the water bodies. First, the water surface reflectance $R_{sfc}(\lambda)$ was derived directly from the ratio of total upwelling water leaving radiance $L_u(\lambda)$ and the total downwelling irradiance $E_d(\lambda)$ measurements as indicated in Eq. (5).

$$R_{sfc}(\lambda) = \frac{L_u(\lambda)}{E_d(\lambda)} \tag{5}$$

However, the total upwelling water radiance is not only of the upper layer of the water molecules and its constituents but also contributions from specular reflectance (sun-sky glint), whitecaps, bubbles, foams, bottom reflectance, etc. If these contributing factors could be duly accounted for, the upwelling water leaving radiance could these be simply obtained by subtracting these factors from the total upwelling water leaving radiance. However, these contributing effects occur in unknown circumstances and still a challenge to correct for all of them (Garaba & Zielinski, 2013). The only measurement that was taken apart from the upwelling water surface radiance and downwelling irradiance was the sky radiance $L_{sky}(\lambda)$ for two water bodies (Markiezaatsmeer and Kristalbad). A more generic way was thus applied to correct for sun-sky glint which is modelled according to Eq. (6).

$$R_{rs}(\lambda) = \frac{L_u(\lambda) - \left(\rho_{air-water} \times L_{sky}(\lambda)\right)}{E_d(\lambda)} \tag{6}$$

Where $\rho_{air-water}$ is defined as the sun-sky glint correction coefficient at the air-water interface (Mobley, 1999). This equation can be modified should the other contributing factors have been measured or derived. Since the measurements were taken from different water bodies with varied meteorological conditions (from fully overcast conditions to clear sky and of rough to gentle winds), a number of $\rho_{air-water}$ were applied.

For Fresnel reflectance of a water surface, Akenine-Möller et al., (2008) recommended $\rho_{air-water}$ = 0.02. For overcast conditions at all wind speed, and also, for wind speed less than 5 ms^{-1} for all conditions, Mobley (1999) recommended $\rho_{air-water}$ = 0.028. Ruddick, et al., (2006) also recommended $\rho_{air-water}$ = 0.0256 for overcoat conditions at all wind speed. All these recommended values of $\rho_{air-water}$ were applied to the RAMSES measurements to derive the remote sensing reflectance. This was tested on clear water, chlorophyll dominated water and a CDOM dominated pit water. Based on the results, the $\rho_{air-water}$ of Mobley (1999) was chosen to derive the $R_{rs}(\lambda)$ for the measurements. Using the selected $\rho_{air-water}$ with the RAMSES measurements taken of the study areas, $R_{rs}(\lambda)$ for Markiezaatsmeer and Kristalbad were derived based on Eq. (6).

Measurements of Benninschelde were taken under an overcast sky condition with no $L_{sky}(\lambda)$ measurements taken. This, to correct for any possible sky reflectance it was assumed that the incoming light from the sky was divided equally among all possible directions. Incoming radiation from the atmosphere thus consisted only of the diffused light from the cloud cover (Kokhanovsky, 2013). Sky radiance was thus obtained by dividing the irradiance measurements by pi (π) as shown in Eq. (7). The resulting sky radiance was then put into Eq. (6) to obtain $R_{rs}(\lambda)$ for Benninschelde Lake.

$$L_{sky} = \frac{E_d(\lambda)}{\pi} \tag{7}$$

In the case of Hulsbeek, Eq. (5) was used to calculate the $R_{sfc}(\lambda)$ and used as the reflectance for the water body. This was because, $L_{sky}(\lambda)$ measurements were not taken and thus Eq. (6) could not be applied. Also, because of the fluctuation in the weather condition, Eq. (7) could not be applied since it only works for overcast skies with diffused light from the cloud cover only.

The variation in the derived $R_{rs}(\lambda)$ for each study area was then assessed. For each of the study areas, the coefficient of variation (CV) for each wavelength of the derived $R_{rs}(\lambda)$ was determined. This was by taken the standard deviation (SD) of $R_{rs}(\lambda)$ divided by the mean of $R_{rs}(\lambda)$ for each wavelength as shown in Eq. (8).

$$CV = \frac{SD\ (R_{rs}(\lambda))}{Mean\ (R_{rs}(\lambda))} \tag{8}$$

4.3. HydroColor Data Processing

4.3.1. Converting RAMSES $R_{rs}(\lambda)$ to $R_{rs}(RGB)$

RAMSES data of $R_{rs}(\lambda)$ were converted to $R_{rs}(RGB)$ to make it comparable to the smartphone images $R_{rs}(RGB)$ derived later in Section 4.3.2. Since the spectral response functions of the smartphone could not be obtained, the standard colourimetric 2-degree observation Colour Matching Functions, CMF's ($\bar{x}, \bar{y}$ and $\bar{z}$) of CIE1931 were used. The

CMF's of CIE1931 shown in Figure 8.a were downloaded from the Institute of Ophthalmology Colour and Vision Research Laboratory through the following link: http://cvrl.ioo.ucl.ac.uk/cmfs.htm.

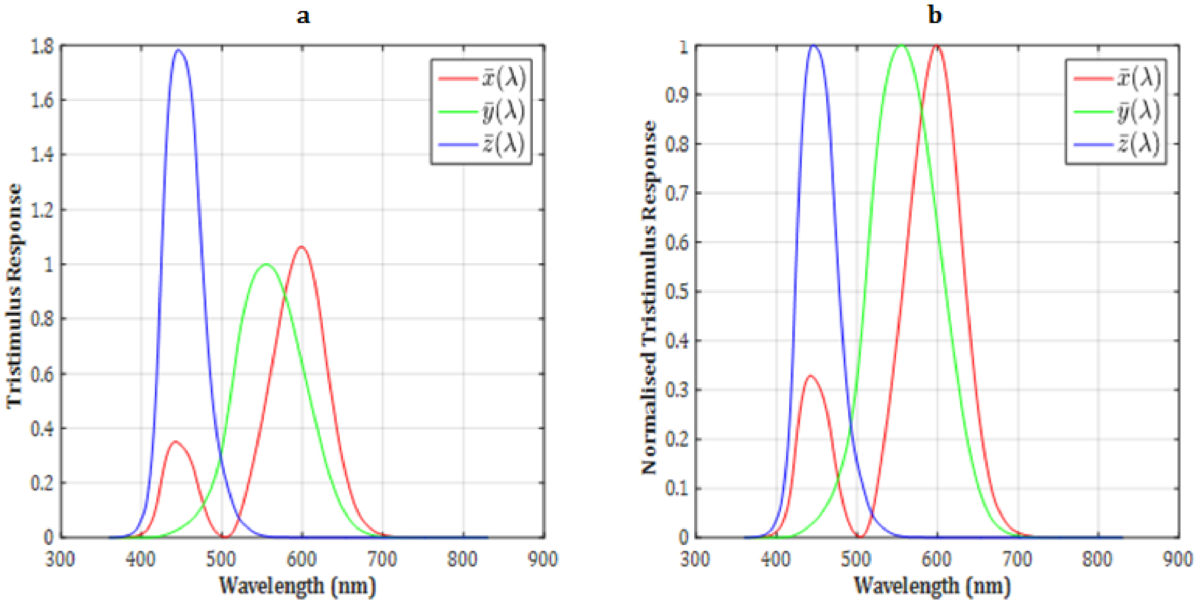

Figure 8: The standard 2-degree field of view colour matching functions (CMF) of CIE1931. Values used to generate the CMF curves were obtained from http://cvrl.ioo.ucl.ac.uk/cmfs.htm. (a) Tristimulus response of the CIE1931 CMF ($\bar{x}\,\bar{y}\,\bar{z}$). (b) Normalized tristimulus response of the CIE1931 CMF ($\bar{x}\,\bar{y}\,\bar{z}$).

The CMFs ($\bar{x}\,\bar{y}\,\bar{z}$) of CIE1931 were first normalised by dividing the tristimulus response value for each wavelength by the maximum value of each tristimuli response to obtain Figure 8.b. This was to ensure equal maximum intensity of the spectral response comparable to the spectral responses of the smartphones used by Leeuw (2014). The normalised $\bar{x}\,\bar{y}\,\bar{z}$ of CIE1931 were then interpolated to obtain the data at 4 nm interval over the visible spectrum (from 380 to 780 nm). This was to make the wavelength interval comparable to the interval of RAMSES data which has its spectral intervals of approximately 3.3 nm.

By convolution, the resulting $\bar{x}$, $\bar{y}$ and $\bar{z}$ of CIE1931 and $R_{rs}(\lambda)$ of RAMSES measurements for each site (from 380 to 780 nm) were then used to derive the $R_{rs}(RGB)$ of RAMSES as shown in Eq. (9).

$$R_{rs}(\mathrm{R}) = \frac{\sum_{380}^{780} R_{rs(RAMSES)}(\lambda) \times \bar{x}(\lambda)}{\bar{x}(\lambda)} \qquad (9a)$$

$$R_{rs}(\mathrm{G}) = \frac{\sum_{380}^{780} R_{rs(RAMSES)}(\lambda) \times \bar{y}(\lambda)}{\bar{y}(\lambda)} \tag{9b}$$

$$R_{rs}(\mathrm{B}) = \frac{\sum_{380}^{780} R_{rs(RAMSES)}(\lambda) \times \bar{z}(\lambda)}{\bar{z}(\lambda)} \tag{9c}$$

4.3.2. Deriving $R_{rs}(RGB)$ from Smartphone Images

Here below I will give an elaboration on the derivation of $R_{rs}(RGB)$ from the HydroColor APP of Leeuw (2014). Point captured images of printed grey paper, grey card, sky and water surface taken via the HyroColor APP of the Samsung Galaxy S4 GT-i9515 were processed to derive their $R_{rs}(RGB)$. Each image was read in an array ranging from 0 to 255 and displayed. A displayed image was then cropped at the middle for the printed grey paper, grey card and sky images, and an area with less specular reflectance, and no whitecaps for the water surface images. The RGB bands for the cropped image were then extracted. The RGB intensity (grey level) values were then normalized from 0 to 1 and subsequently averaged to obtain single values for each band.

In two of the field campaigns (Binnenschelde and Hulsbeek), a printed grey paper was used in place of a grey card. In this case, the derived RGB of these images had to be recalibrated to account for the printer tint on paper, that is, to account for the standard colour of the grey card. Following the same procedure, the RGB of 10 images of a grey card (5 each taken under sunny and shadowed conditions) and 10 images of the printed grey paper (5 each taken under sunny and shadowed conditions) were derived. A relation was then established between the grey card and printed grey paper using linear regression as shown in Eq. 10.

$$Required\ grey\ card\ results = (printed\ paper \times slope) + intercept \tag{10}$$

The same relation was used for the two atmospheric conditions separately and for both conditions combined. The resulting linear regression coefficients for the shadowed condition were then used to correct for the printed grey paper images RGB using a linear model.

The RGB values were then used to obtain the relative radiance $L_{rel}(RGB)$ of the images using Eq. (11). The camera's exposure time (α) during the capture of an image was obtained from the HydroColor APP Library of the smartphone.

$$L_{rel}(RGB) = \frac{RGB}{\alpha} \tag{11}$$

The water leaving reflectance for each band $R_{rs}(RGB)$ was then obtained using Eq. (12).

$$R_{rs}(RGB) = \frac{L_{rel}\big(L_{sfc}(RGB)\big) - \rho \times L_{rel}(L_{sky}(RGB))}{\frac{\pi}{R_{ref}} L_{rel}(L_{gc}(RGB))} \qquad (12)$$

Where; $L_{rel}\big(L_{sfc}(RGB)\big)$ = the relative water surface radiance, $L_{rel}\big(L_{sky}(RGB)\big)$ = the relative sky radiance, $L_{rel}\big(L_{gc}(RGB)\big)$ = the relative gray card or printed grey paper radiance, R_{ref} = the standard reference reflectance of the grey card which was taken as 0.18 and ρ = the sun-sky glint correction coefficient at the air-water interface taken as 0.028 from Mobley (1999).

A summary of the processes used in a structural diagram is as shown in Figure 9.

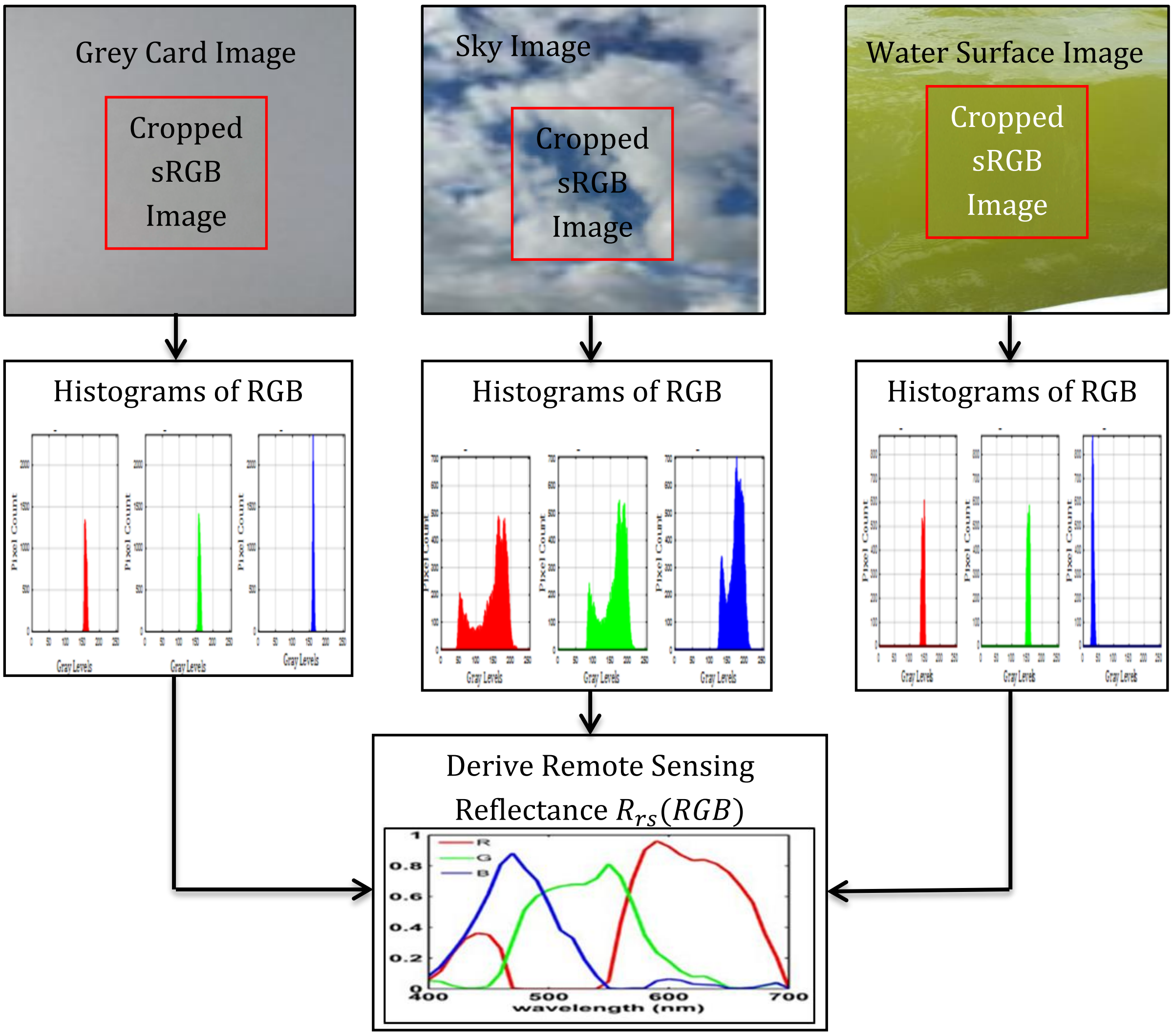

Figure 9: An illustration of the smartphone images processing to derive remote sensing reflectance $R_{rs}(RGB)$. The uper panel is the cropping of the images, middle panel is the derivation of the histograms of the images and the lower panel is the derivation of the resulting $R_{rs}(RGB)$ from the images. The $R_{rs}(RGB)$ image was taken from Leeuw (2014).

4.3.3. Deriving HydroColor APP Water Quality Variables

The $R_{rs}(R)$ derived from the smartphone images were used to obtain estimates of turbidity and [SPM] using specific models used by the HydroColor APP. The model used to estimate turbidity ($Turb$) from the water leaving reflectance of the red band $R_{rs}(R)$ as cited in Leeuw (2014) is as shown in Eq. (13). From this model, 0.044 is the saturation of the red band reflectance, sr^{-1} and 22.57 is the estimate of turbidity for which the red band reflectance is at half the saturation level, gm^{-3} as defined by Ambarwulan et al. (2012).

$$Turb = \frac{22.57R_{rs}(R)}{0.044 - R_{rs}(R)} \tag{13}$$

The APP uses a relation of turbidity (in FNU, Formazine Turbidity Unit) and the [SPM] to estimate $\log_{10}$[SPM] as cited in Leeuw (2014) is as shown in Eq. (14);

$$log_{10}[SPM] = 1.02log_{10}(Turb) - 0.04 \tag{14}$$

4.3.4. Assessment of Alternative Models to Estimate Turbidity and [SPM]

The laboratory measurements of the water samples and the $R_{rs}(R)$ derived from the smartphone images were used to develop alternative models for the estimation of turbidity and [SPM] from smartphone images. The following steps as shown below were applied based on the GeoCalVal method of Salama et al. (2012). The steps applied as follows for turbidity was also applied for [SPM];

The laboratory turbidity data and the $R_{rs}(R)$ of smartphone images were subdivided into calibration (Cal) and validation (Val) data sets. Taking the Cal data set, the first case was applying nonlinear regression by fitting the data to the model indicated in Eq. (15) using ordinary least square method. The second instant was by type I linear regression using ordinary least square method to fit the data to the model of Eq. (16). In the case of the type I linear regression, the $R_{rs}(R)$ were log transformated. From the two models as shown in Eq. (15 & 16), the independent variable is turbidity ($Turb$), the dependent variables are $R_{rs}(R)$ and $log_{10}(R_{rs}(R))$, and α_{HT1}, β_{HT1}, α_{HT2} and β_{HT2} are the coefficients to be estimated. The estimates of the model coefficients were then obtained from the model fit and then stored as probability distributions (PD$_c$) on bootstrapping the Cal data set. The standard error SE and mean absolute error MAE in estimating the model coefficients were also obtained.

$$Turb = \frac{\alpha_{HT1} \times R_{rs}(R)}{\beta_{HT1} - R_{rs}(R)} \tag{15}$$

$$Turb = \alpha_{HT2} \times log_{10}(R_{rs}(R)) + \beta_{HT2} \tag{16}$$

The mean of the estimated model coefficients was then obtained. Taking the Val data set of $R_{rs}(R)$, the mean of the model coefficients were then use as input into Eq. (15 & 16) respectively in the case of the semi-analytical nonlinear model or the linearised model to estimate $Turb$. Using type II regression analysis, a linear model was then fit between the estimated $Turb$ and the Val set $Turb$. The models coefficients, SE and MAE of the models coefficients and their R^2 were determined. The results from the validation data set were then store as probability distribution (PD_V).

The semi-analytical nonlinear model that was used in estimating the [SPM] is as shown in Eq. (17) which is based on Nechad et al. (2010). On log transforming the $R_{rs}(R)$ the model that was also used to estimate the [SPM] is as shown in Eq. (18).

$$[SPM] = \frac{\beta_{HS1} \times R_{rs}(R)}{\alpha_{SH1} + R_{rs}(R)} \tag{17}$$

$$[SPM] = \frac{log_{10}(R_{rs}(R)) - \beta_{HS2}}{\alpha_{HS2}} \tag{18}$$

4.3.5. Error Quantification

The uncertainty in the models variables were quantified; for instance the error in the turbidity semi-analytical nonlinear model of Eq. (15) was obtained by calculating its total error σ_{Turb}. This, the uncertainty of any estimated turbidity results based on the effect of uncertainty in the red band reflectance $R_{rs}(R)$, the model coefficients α_{HT1} and β_{HT1} was obtained by assuming these variables as independent. It should be noted that, since the noise to signal ratio of the smartphone device used was unknown, errors from the smartphone device could therefore not be quantified. Error due to the smartphone device is thus not inclusive in the total error. First, the mean $\mu_{\alpha_{HT1}}$ of these estimated variables were obtained as shown in Eq. (19). For example, using the alpha coefficient where; $\alpha_{HT1,i}$ represents the observations and n is the number of observations. The measure of how widely these observations are dispersed from the mean was obtained using the standard deviation $\sigma_{\alpha_{HT1}}$ as shown in Eq. (20) where; $n - 1$ is the degree of freedom lost in estimating the mean. By assuming that the total error is a sum of independent variables, a common formula can be used based on Taylor series of approximation of the first order expansion as shown in Eq. (21) to propagate its contributing error factors (Bevington & Robinson, 2003; Ku, 1966). From Eq. (15), turbidity was estimated based on α_{HT1}, β_{HT1} and $R_{rs}(R)$. This, the square root of the sum of squares for the partial derivative of turbidity with respect to each parameter multiplied by the standard deviation of each parameter was used to obtain the total error.

$$\mu_{\alpha_{HT1}} = \frac{\alpha_{HT1,i}}{n} \tag{19}$$

$$\sigma_{\alpha_{HT1}} = \sqrt{\frac{\sum_{i=1}^{n}(\alpha_{HT1,i} - \mu_{\alpha_{HT1}})^2}{n-1}} \tag{20}$$

$$\sigma_{Turb} \approx \sqrt{\left(\frac{\partial Turb}{\partial \alpha_{HT1}}\right)^2 \sigma_{\alpha_{HT1}}^2 + \left(\frac{\partial Turb}{\partial \beta_{HT1}}\right)^2 \sigma_{\beta_{HT1}}^2 + \left(\frac{\partial Turb}{\partial R_{rs}(R)}\right)^2 \sigma_{R_{rs}(R)}^2} \tag{21}$$

4.4. Citclops Data Processing

4.4.1. Converting RAMSES $R_{rs}(\lambda)$ to FUI

Forel-Ule index (FUI) from the $R_{rs}(\lambda)$ of RAMSES were derived by using the Forel-Ule MERIS (FUME) model of Wernand et al., (2013). First, the $R_{rs}(\lambda)$ of RAMSES were normalised by dividing $R_{rs}(\lambda)$ values for each wavelength by the maximum $R_{rs}(\lambda)$ value. The normalised $R_{rs}(\lambda)$ of RAMSES (as a colour function in the spectrum) were then multiplied by the standard colourimetric 2-degree Colour Matching Functions, CMF's ($\bar{x}, \bar{y}$ and $\bar{z}$) of CIE1931 and integrated over the visible spectrum (from 380 to 780 nm) as shown in Eq. (22) following the Grassmann's law in optics (Gert, 1996).

$$X = \int_{\lambda_{min}}^{\lambda_{max}} R_{rs}(\lambda)\bar{x}(\lambda)d\lambda = \sum_{380}^{780} R_{rs}(\lambda)\bar{x}(\lambda)d\lambda \tag{22a}$$

$$Y = \int_{\lambda_{min}}^{\lambda_{max}} R_{rs}(\lambda)\bar{y}(\lambda)d\lambda = \sum_{380}^{780} R_{rs}(\lambda)\bar{y}(\lambda)d\lambda \tag{22b}$$

$$Z = \int_{\lambda_{min}}^{\lambda_{max}} R_{rs}(\lambda)\bar{z}(\lambda)d\lambda = \sum_{380}^{780} R_{rs}(\lambda)\bar{z}(\lambda)d\lambda \tag{22c}$$

This resulted in single tristimulus values (X, Y and Z) computed for each $R_{rs}(\lambda)$ spectral curve. The CMF's of CIE1931 shown in Figure 8 for a 2-degree field of observation thus served as a weighting function to obtain the XYZ tristimuli values of the normalized $R_{rs}(\lambda)$ in CIE XYZ colour space (Wernand et al., 2013). The XYZ tristimuli values thus theoretically represent the amount of the three primary colours (RGB) stimulus of the human eye at their respective wavelength. Working with this three-dimensional colour space is complex. Thus, the tristimuli values were normalization (X +Y + Z =1). This was by taken the ratio of each tristimulus value and the sum of the three values, to obtain the *xyz* chromaticity coordinates as shown in Eq. (23). By this, the chromaticity coordinates of every point measurement (x_P, y_P, z_P) was calculated.

$$x = \frac{X}{X+Y+Z} \tag{23a}$$

$$y = \frac{Y}{X+Y+Z} \tag{23b}$$

$$z = \frac{Z}{X+Y+Z} \tag{23c}$$

This was followed by calculating the hue colour angle $\alpha_P(°)$ of each point. The chromaticity coordinates x_P *and* y_P with respect to the white point WP $(x_W = y_W = 1/3)$ were determined by subtracting (x_P, y_P) from (x_W, y_W) respectively. Taken WP as the midpoint, the hue colour angle (that is, the angle around the central vertical axis to $x_P - y_W, x_P = y_W$) was determined. This was by using the ATAN2 function in MATLAB programme in order to return the quadrant of the angle in radians. The derived angle was then multiplied by $180/\pi$ to obtain the angle in degrees as shown in Eq. (24).

$$\alpha_P(°) = arctan2(y_i - y_W, x_i - x_W) \times \frac{180}{\pi} \tag{24}$$

Using the same procedure as above, hue colour angles $\alpha_N(°)$ of Novoa et al. (2013) were derived using their CIE tristimulus values from laboratory prepared FU solutions transmission measurements. The resulting angles from the point measurements were then compared with the angles derived from the laboratory solutions of Novoa et al.

(2013) shown in Figure 10. Using a MATLAB loop for 1 to 21 FUI, if the argument; $\alpha_P(°) < \alpha_N(°)$ is true, then the FUI to the angle lower than $\alpha_N(°)$ is selected. Also, if $\alpha_P(°) >$ the maximum of $\alpha_N(°)$, 1 is selected, else, if $\alpha_P(°) <$ minimum of $\alpha_N(°)$ then 21 is selected. This was then used to obtain the FUI of all the point measurements.

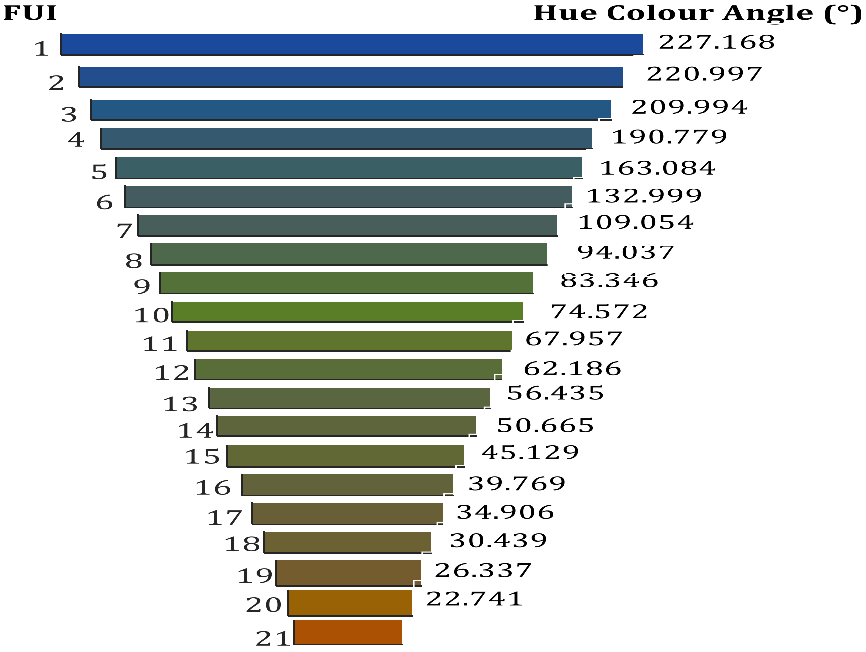

Figure 10: Hue colour angles $\alpha_N(°)$ and their corresponding Forel-Ule index (FU 1 to 21) of Novoa et al. (2013). These $\alpha_N(°)$ were derived from laboratory FU solutions of transmission measurements of their research.

4.4.2. Deriving FUI from Smartphone Images

The RGB bands (R'G'B') extracted from the cropped water surface images of Section 4.3.2 were used. The following procedure applied on the R'G'B' were based on the Water COlour from Digital Images (WACODI) model of Novoa et al. (2015). Here below I will give an elaborated explanation on the WACODI model which was modified to suit this research. For each of the R'G'B' bands, a gamma correction was first applied by using Eq. (25) to return each band's digital numbers to a linear level. In this case the gamma expansion value was taken as 2.2 since this value is standard for sRGB colour images and also generally used for digital instruments.

$$R = \begin{cases} \left(\dfrac{\frac{R'}{255} + 0.055}{1.055}\right)^{2.2} & if\ \dfrac{R'}{255} \leq 0.04045 \\ R' & else \end{cases} \tag{25a}$$

$$G = \begin{cases} \left(\dfrac{\frac{G'}{255} + 0.055}{1.055}\right)^{2.2} & if\ \dfrac{G'}{255} \leq 0.04045 \\ G' & else \end{cases} \tag{25b}$$

$$B = \begin{cases} \left(\dfrac{\frac{B'}{255} + 0.055}{1.055}\right)^{2.2} & if\ \dfrac{B'}{255} \leq 0.04045 \\ B' & else \end{cases} \tag{25c}$$

The RGB values from each pixel were then averaged to obtain single values for each band. By this, the resulting RGB values were then multiplied by a conversion matrix of Eq. (26) by Pascale (2003) as shown in Eq. (27) to obtain the tristimuli values XYZ of the images.

$$[M] = \begin{bmatrix} 0.4124 & 0.3575 & 0.1804 \\ 0.2126 & 0.7151 & 0.0721 \\ 0.0193 & 0.1191 & 0.9503 \end{bmatrix} \tag{26}$$

$$\begin{bmatrix} X \\ Y \\ Z \end{bmatrix} = [M] \begin{bmatrix} R \\ G \\ B \end{bmatrix} \tag{27}$$

These XYZ values in the case of the human eye represent the three cone types (red, green, and blue, RGB) in the retina and accounts for an images colour. However, each time the illumination condition varies, each cone independently turns to adapt to the illuminant (von Kris, 1970). This phenomenon is termed chromaticity adaptation. A chromatic adaptation model was thus applied by transforming the tristimuli values into a cone response domain and then individually scaling the RGB components according to the current and desired illuminants (Reinhard et al., 2014). The chromaticity adaptation was thus applied using Bradford method of cone response matrix $[B]$ of Eq. (28) (Katoh & Nakabayashi, 2001).

$$[B] = \begin{bmatrix} 0.8951 & 0.2664 & -0.161 \\ -0.7502 & 1.7135 & 0.0367 \\ 0.0389 & -0.0685 & 1.0296 \end{bmatrix} \tag{28}$$

The $[B]$ was first transformed with the reference light source taken as CIE standard illumination D65 (source white $[W_s]$; [0.95047 1.0000 1.08883]) of natural daylight illuminant to obtain the source white point $[BW_s]$ as shown in Eq. (29). Since the desired illuminant was an even colour of equal weight to all wavelength, illiminant E was used with elements[1.000 1.000 1.000] as the destination white $[W_d]$. Also, the $[W_d]$ was transformed with $[B]$ to obtain the destination white point $[BW_d]$ as shown in Eq. (29).

$$[BW_s] = [B] \times [W_s] \text{ and } [BW_d] = [B] \times [W_d] \tag{29}$$

Alternatively, the $R_{rs}(\lambda)$ and $L_u(\lambda)$ of the RAMSES data obtained in Section 4.2 for each site was used to calculate the illumination spectrum (E_{ill}) as shown in Eq. (30). Convolution was then used to weigh the resulting E_{ill} spectral with the CMF of CIE1931 as used previously in deriving $R_{rs}(\lambda)$ from RAMSES $R_{rs}(\lambda)$ from Section 4.3.1. The resulting vectors were also then used as $[W_s]$. The $[W_s]$ of RAMSES were similar to the $[W_s]$ of the average daylight of CIE standard illumination D65. The $[W_s]$ of CIE standard illumination D65 was thus chosen for further analysis.

$$E_{ill} = \frac{L_u}{R_{rs}} \tag{30}$$

The illumination correction matrix $[ICM]$ was then calculated by the product of $[BW_s]$ and the reciprocal of $[BW_d]$, and the diagonal adaptation matrices of [B] and [B^{-1}] as shown in Eq. (31). The $[ICM]$ was then applied on the XYZ of the images to obtain the chromatic adaptation $[XYZ_{ca}]$ colour corrected images as shown in Eq. (32) (Kang, 1996).

$$[ICM] = [B]^{-1} \times \left(\frac{[BW_d]}{[BW_s]}\right) \times [B] \tag{31}$$

$$[XYZ_{ca}] = [ICM] \times [XYZ] \tag{32}$$

The chromatic adapted XYZ_{ca} were then used to calculate the chromaticity coordinates and subsequently the $\alpha_P(°)$ and FUI as applied on the RAMSES data from the previous section. A summary of the processes used in a structural diagram is as shown in Figure 11.

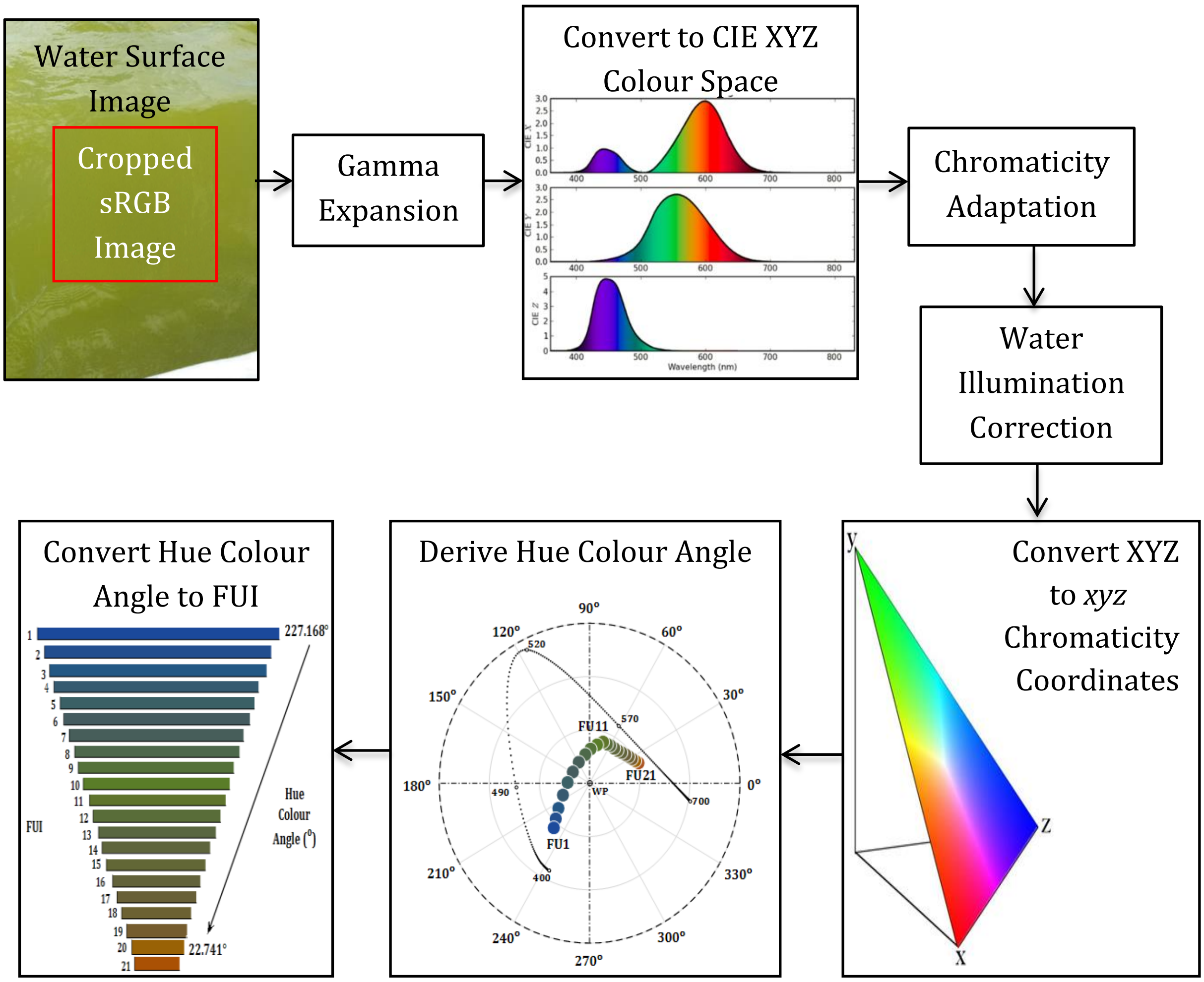

Figure 11: Structural diagram of the processes used to derive the xyz chromaticity coordinates, hue colour angle $\alpha_P(°)$ and Forel-Ule index FUI of the smartphone images adapted from Novoa et al. (2015).

The $\alpha_P(°)$ and FUI of the smartphone images on comparison with the $\alpha_P(°)$ and FUI derived from RAMSES was used to calculate the deviation (Δ) of the smartphone images from RAMSES (which is considered to be the "true" measured colour of the water bodies). The Δ of the smartphone images from RASMES were then used to develop a model for the smartphone images $\alpha_P(°)$ Δ as applied on MERIS data by van der Woerd & Wernand (2015).

Visual judgement was also used to compare the smartphone water surface images to the FU scale develop by Wernand et al. (2013). This was by using the RGB values of the FU scale to generate images and their corresponding FUI and to visually compare these images to the smartphone images.

4.4.3. Comparison of RAMSES and Smartphone Images *xyz* Chromaticity Coordinates

The derived *xyz* chromaticity coordinates of RAMSES was compared to the *xyz* chromaticity coordinates derived from the smartphone images taken of the water surfaces. Also the $\alpha_P(°)$ and the FUI derived from RAMSES observations and the $\alpha_P(°)$ and FUI of the smartphone images were compared. This was by using linear regression analysis to fit the data sets by ordinary least squares method to a line. The goodness of fit and uncertainty of the data sets to the fitted lines were then determined. The statistical measures that were used included; root mean square error (RMSE), percentage error (PE) and determination coefficient (R^2). Mathematical equations of these statistical measures are as shown in Eq. (33-35) for the FUI of RAMSES and the smartphone images. The 95 % confidence intervals CI of the data sets were then determined.

$$RMSE = \sqrt{\left(\frac{1}{n}\sum_{i=1}^{n}\left(FUI_{(RAMSES),i} - FUI_{(APP),i}\right)^2\right)} \tag{33}$$

$$PE = \frac{\left|FUI_{(RAMSES),i} - FUI_{(APP),i}\right|}{FUI_{(RAMSES),i}} \times 100 \tag{34}$$

$$R^2 = 1 - \frac{\sum_{i=1}^{n}(FUI_{(RAMSES),i} - FUI_{(APP),i})^2}{\sum_{i=1}^{n}(FUI_{(RAMSES),i} - \mu_{(RAMSES)})^2} \tag{35}$$

Where; n is the number of observations and μ is the mean of the obsevations.

4.4.4. Deriving Water Quality Variables for Citclops APP

As a pilot study, the *x* chromaticity coordinate derived from the smartphone images were used to obtain estimates of turbidity and [SPM] using specific models applied on the $R_{rs}(R)$ for HydroColor APP. The model used to estimate these water quality variables for HydroColor APP are shown in Section 4.3.4. This, in place of $R_{rs}(R)$, the *x* chromaticity coordinate was used.

4.4.5. Error Quantification

Since the estimation of turbidity and [SPM] through Citclops was proposed to be based on the same models used for HydoColor, the same procedure was followed to derive the uncertainty in the models parameters.

4.4.6. Deriving Colour Saturation and Dominant Wavelength

CIE1931 chromaticity coordinates (x_{cie}, y_{cie}) data were downloaded from the Institute of Ophthalmology CVRL through the following link: http://cvrl.ioo.ucl.ac.uk/cmfs.htm. The spectral wavelength (λ_{cie}) of the data was from 360 to 830 nm at 1 nm interval. The data were then plotted with the white point WP taken as (1/3, 1/3). The WP was then moved to the origin of a polar coordinate with the rest of the CIE1931 coordinates by subtracting (1/3, 1/3) from (x_{cie}, y_{cie}). The resulting (x_{cie}, y_{cie}) in the polar coordinate system was then used to obtain the radius rad_{cie} and angle θ_{cie} (in radians) using Eq. (36) and (37) respectively. For an angle within the fourth quadrant (IV) as shown in Figure 12, 2π was added.

$$rad_{cie} = \sqrt{(x_{cie})^2 + (y_{cie})^2} \tag{36}$$

$$\theta_{cie} = tan^{-1}\left(\frac{y_{cie}}{x_{cie}}\right) \tag{37}$$

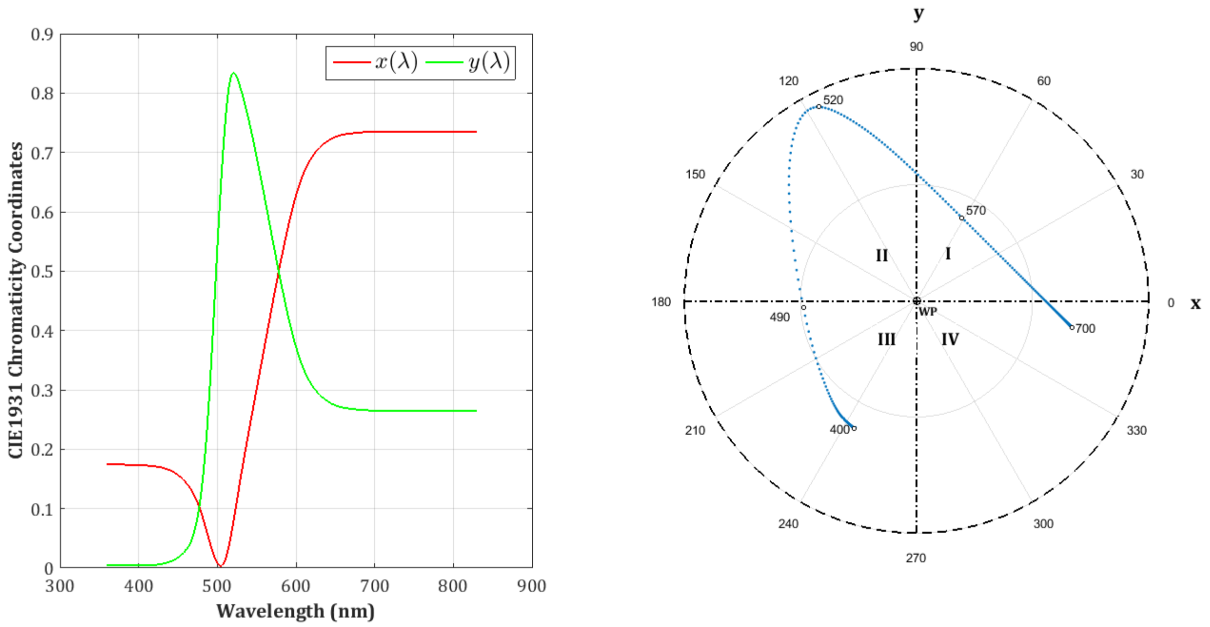

Figure 12: An illustration of the derivation of radians and angles from the *xy* chromaticity coordinate on a polar coordinate system. The left panel is the *xy* chromaticity coordinates of CIE1931 2-degree standard observation for spectrally pure colours at specific wavelengths (λ). Source: Colour & Vision Research Laboratory Database http://cvrl.ioo.ucl.ac.uk/cmfs.htm. The right panel is the *xy* chromaticity coordinates of a polar coordinate system showing the four quadrants of the polar coordinate system. The white point (WP) is indicated as the origin.

Field results of the chromaticity coordinates (x_{field}, y_{field}) for each point was then used to calculate the colour saturation and dominant wavelength. First, on reading a point measurement of (x_{field}, y_{field}), the WP was then subtracted from it. The resulting (x_{field},

y_{field}) in the polar coordinate system was then used to obtain the radius rad_{field} and angle θ_{field} (in radians) using Eq. (38) and (39) respectively.

$$rad_{field} = \sqrt{(x_{field})^2 + (y_{field})^2} \tag{38}$$

$$\theta_{field} = tan^{-1}\left(\frac{y_{field}}{x_{field}}\right) \tag{39}$$

The minimum of the absolute difference between θ_{field} and θ_{cie} were then obtained using Eq. (40) through a MATLAB programme. By this, the value of the minimum difference ($\min\_val$) and the index with the minimum difference (i_min) were determined.

$$[\min\_val,\ i\_min] = \min\big(abs(\theta_{field} - \theta_{cie})\big) \tag{40}$$

By using i_min, the corresponding λ_{cie} with the same index is selected as the dominant wavelength λ_{dom} of the measured (x_{field}, y_{field}) point.

Also, using i_min, the corresponding rad_{cie} with the same index is selected as the radius from the WP to the dominant wavelength. The colour saturation of the point measurement (x_{field}, y_{field}), was then calculated as the ratio of rad_{field} and rad_{cie} as shown in Eq. (41).

$$Colour\ Saturation = \frac{rad_{field}}{rad_{cie}} \tag{41}$$

On the other hand, the $\min\_val$ was then used to calculate the deviation Δ of the angle in degrees θ^o by using Eq. (42) to obtain the degree of deviation.

$$\Delta\ in\ \theta^o = \min\_val \times \frac{180}{\pi} \tag{42}$$

5. RESULTS AND DISCUSSIONS

5.1. Remote Sensing Reflectance

The dataset used in this research work included measurements of water bodies of varying water quality variables taken under different environmental conditions. This was to enable a good assessment of the smartphone APPs for such varying water systems. Generally, the bottleneck to remote sensing of water quality is the sun-sky glint effect which masks the intrinsic radiances of water surfaces. A good estimation of $R_{rs}(\lambda)$ would thus imply an accurately corrected sun-sky glint effects. Thus, using different sun-sky glint correction factor $\rho_{air-water}$, the following results as shown in Figure 13 were obtained for the resulting $R_{rs}(\lambda)$ of selected sample sites. Different $\rho_{air-water}$ were applied to slightly clear water, chlorophyll-a pigment material dominated water and CDOM dominated water respectively of Figure 13.a, b & c. Some general observations were made of the different water types. The clear water showed strong absorption of the green and red spectral bands with high reflectance at the blue spectral band region. The chlorophyll-a pigment materials dominated water showed high reflectance at the green and red spectral band region while strong absorption at the blue spectral band region. The results for the CDOM dominated water system indicated strong absorption of blue light by CDOM and strong reflectance at the red spectral band region.

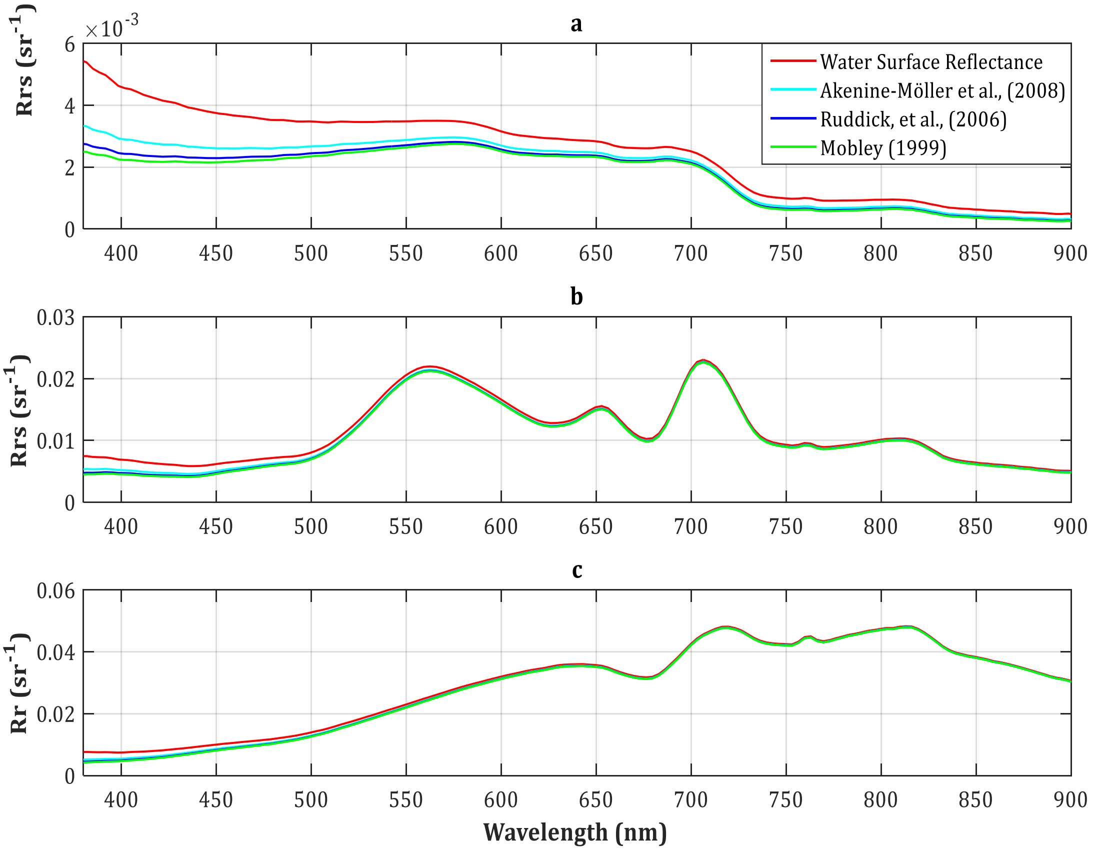

Figure 13: Spectral reflectance curves of water surface reflectance and remote sensing reflectance derived using different sun-sky glint correction factors applied to different water bodies. (a) Spectral reflectance curves of a clear water. (b) Spectral reflectance curves of a chlorophyll-a pigment materials dominated water. (c) Spectral reflectance curves of a CDOM dominated water.

From the above results, the $\rho_{air-water}$ of Mobley (1999) of 0.028 was used to correct for specular reflectance for the measurements of Binnenschelde, Markiezaatsmeer and Kristalbad to derive their $R_{rs}(\lambda)$. This was because it gave low reflectance values for all the water type it was tested on. The resulting spectral reflectance curves for the various study areas are as shown in Figure 14.a-e. The spectral reflectance curves of the water surfaces are shown as blue curves whereas the coefficient of variation (CV) between the wavelengths is shown in red. The magnitude of variation of the $R_{rs}(\lambda)$ across the spectral curves specifies the absorption and scattering of water molecules and the specific properties of each optically significant constituent and their effects on a light field as a function of wavelength.

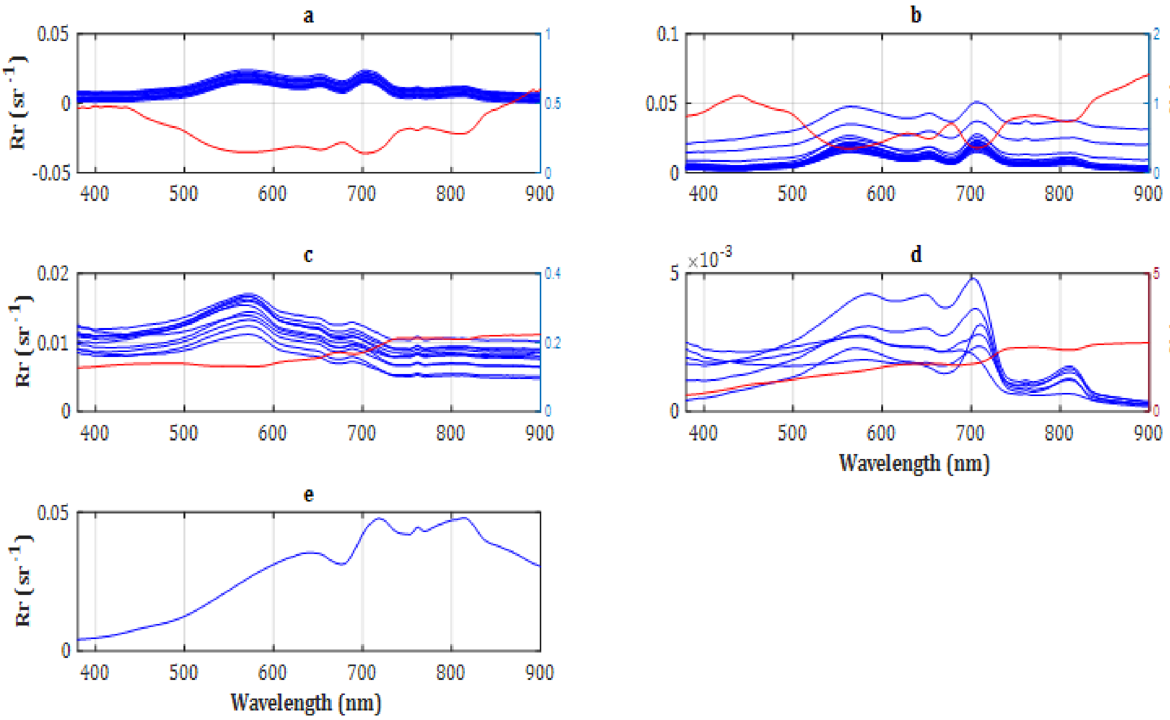

Figure 14: Spectral reflectance curves (blue lines) for the sample sites and their corresponding coefficient of variation of the wavelengths (red line). For all the measurements, Mobley (1999) sun-sky glint correction factor of 0.028 was used to correct for specular reflectance except for Hulsbeek Lake (c). (a) Binnenschelde Lake; (b) Markiezaatsmeer Lake; (c) Hulsbeek Lake; (d) Kristalbad Artificial Wetland; (e) CDOM dominated pit water sampled near Kristalbad wetland.

The spectral reflectance curves of Binnenschelde Lake and Markiezaatsmeer Lake were characterised by troughs at 624 and 670 nm. The spectral reflectance curves also showed peaks at 570 – 600 nm, 650 nm, and 704 – 710 nm. These troughs and peaks indicated the presence of chlorophyll and cyano-phycocyanin at the time these measurements were taken. Apart from these water quality variables, the presence of SPM and other CDOM constituents generally lowered the reflectance at the blue wavelengths of the hyperspectral measurements for these lakes.

Measurements for Binnenschelde Lake were taken under an overcast sky and rough wind condition. Although the wind-roughened surface could cause more reflectance facets, the overcast condition, on the other hand, reduces sun-sky glint effect. Thus, less variation within the individual spectral reflectance curves was observed. The CV of the wavelengths was also lower with a maximum of 0.62 at the infrared spectral region as indicated in Table 2.

Measurements for Markiezaatsmeer Lake were taken under fluctuating weather condition (from diffused clouds to clear skies and from gentle to rough winds). Such fluctuations resulted in large variations seen in the spectral reflectance curves. Apart from the spatial-temporal dynamics of a given inland water body which may account for such variations, the wind-roughened water surface enhanced variable wave slopes. The presence of varying illumination condition would have concurrently resulted in more Fresnel mirrored facets. The windy condition also resulted in the formation of whitecaps which affects observed reflectance should the measuring instrument be pointed in its direction. It is possible that the fluctuating illumination condition alone could have been the main cause of the spectral reflectance variations. For instance, the illumination condition at which some downwelling irradiance $E_d(\lambda)$, upwelling water surface radiance $L_u(\lambda)$, and sky radiance $L_{sky}(\lambda)$ were taken differed. This was because, measurements of $E_d(\lambda)$ and $L_u(\lambda)$ had to be taken before $L_{sky}(\lambda)$. In such a fluctuating weather condition, the illumination condition sometimes changed before changing terms of the measuring instrument. The CV of the wavelengths for the spectral curves was thus observed to be higher with a maximum of 1.43 as shown in Table 3.

Measurements for Hulsbeek Lake (c) were characterised by diffused to overcast clouds and from gentle to rough winds. The variation in its spectral curves could thus be due to the varying conditions at which the measurements were taken as discussed on Markiezaatsmeer Lake. Quite apart, not been able to correct for sun-sky glint effects due to inadequate information taken of the water body could also account for such variations. It should be noted that results from this lake were however used for further data analysis. This could translate into errors in the comparison of the RAMSES data with other data sets since its spectral reflectance curves plainly showed the variations in the measurements.

Measurements of Kristalbad artificial wetland (d) were taken under clear skies and gentle winds. However, the wetland was a shallow water system of different compartments and thus had a bottom reflectance of varying characteristics. This explains the high variation in the spectral reflectance curves of this site. Since the wetland was divided into compartments, each compartment's water had some eminent water characteristic. This is evident in the high CV of the wavelengths to a maximum of 2.49. Out of 6 measurements taken of Kristalbad wetland, only 1 had no bottom effect. Not been able to correct for the bottom reflectance, these measurements were removed from the dataset before any further analysis. The outstanding spectral reflectance curve shown of Figure 14.e is CDOM dominated pit water which was sampled near Kristalbad artificial wetland. Its spectral reflectance curve thus showed strong absorption of blue light by CDOM and strong reflectance in the red spectral band region.

Table 2: Summary of the coefficient of variation, CV of selected wavelengths for the study areas. The wavelengths used are dependent on the TriOS RAMSES-ACC-VIS irradiance sensor.

Wavelength (nm)		401.92	502.54	603.11	703.37	803.08	901.79
Binnenschelde	CV	0.48	0.29	0.17	0.14	0.28	0.62
Markiezaatsmeer		0.89	0.81	0.46	0.36	0.74	1.43
Hulsbeek		0.13	0.14	0.14	0.17	0.21	0.23
Kristalbad		0.67	1.17	1.62	1.73	2.23	2.49

5.2. Laboratory measurements

Summary of the results of the laboratory measurements of the water samples are as shown in Table 3. The water quality variables with the sampled sites are demonstrated as bar plots shown in Figure 15. The result indicated a variation of two orders of magnitude for turbidity and [SPM]. This indicates the variation in the nature of the water type sampled. The [SPM], however, showed the highest variation with 1.65 as the CV.

Table 3: Statistical summary of laboratory measurements of water quality variables: [SPM], the concentration of suspended particulate materials; SD, standard deviation; and CV, the coefficient of variation.

Water Quality Variables	Minimum	Maximum	Median	Mean	SD	CV
Turbidity (NTU)	1.40	163.4	20.66	22.88	37.67	1.65
[SPM] (mgL^{-1})	7.50	136.00	58.00	57.06	42.99	0.75

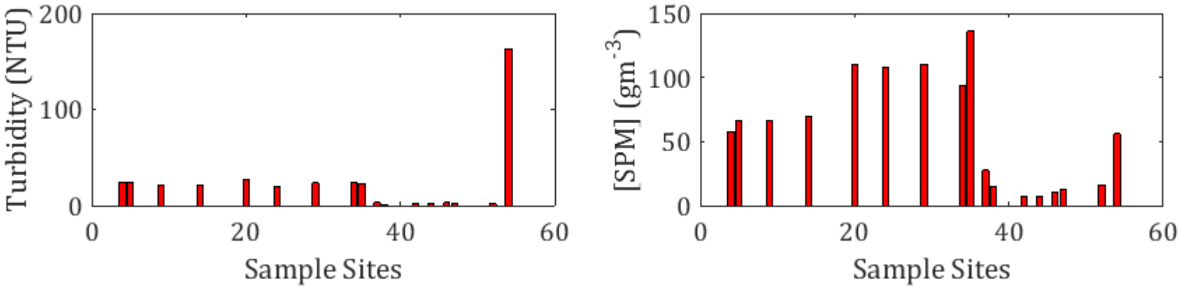

Figure 15: Bar plots of laboratory measured water quality variables with respect to their sample sites. (a) Turbidity. (b) [SPM], the concnetration of suspended particulate materials.

With turbidity being the degree to which light is scattered by dissolved and suspended materials in a water system, the relation between turbidity and the [SPM] was determined as shown in Figure 16. The correlation between turbidity and [SPM] indicated an R^2 of 0.79. The significant relation between turbidity and [SPM] confirmed the direct relation of these two variables stated in literature. According to Neukermans et al., (2012) where a linear model was developed for this two water quality variables, the relation work for both Case 1 and Case 2 water.

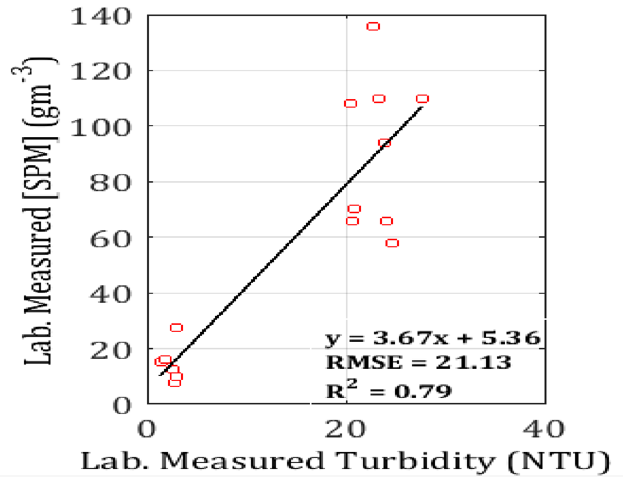

Figure 16: Relation between laboratory measured turbidity and the [SPM].

5.3. Smartphone Images Analysis

Results of selected smartphone images processed according to Section 4.3.2 is as shown in Figure 17-19 and Annex V. This shows the extracted RGB bands from a cropped image of which the histogram of each band was derived. This gave the pixel count on the y-axis and the grey level from 0 to 255 on the x-axis for each band.

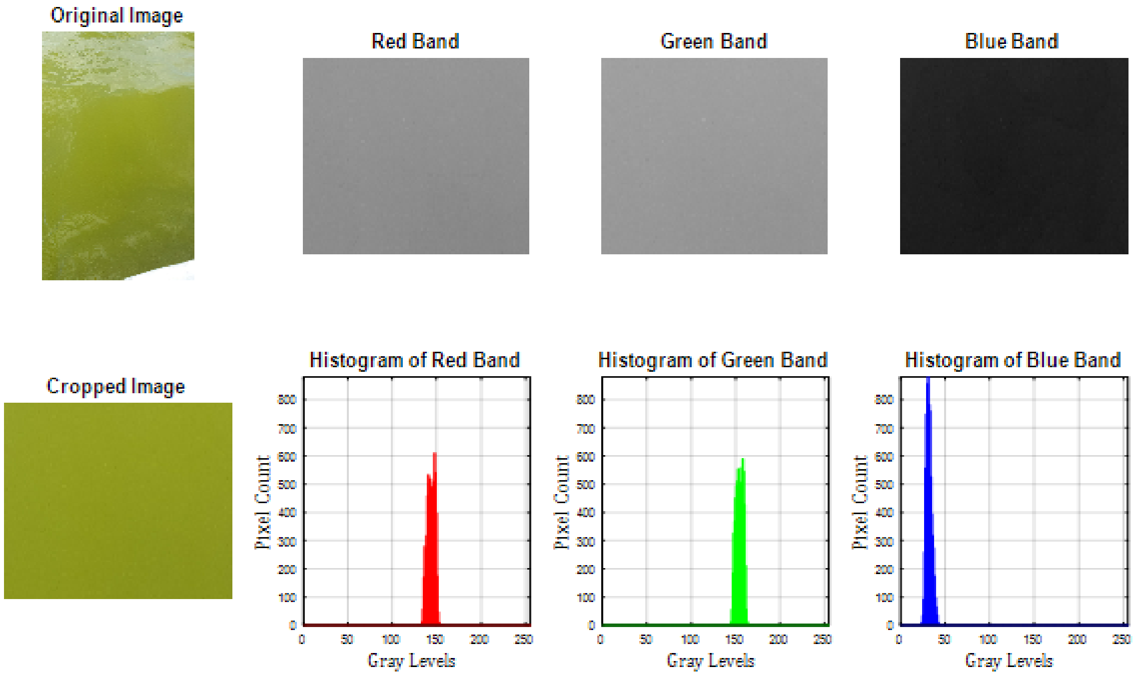

Figure 17: Derived RGB bands of a water surface image taken at Markiezaatsmeer Lake. The upper panel from left to right is the original image, the red band of the cropped image, the green band of the cropped image and the blue band of the cropped image. The lower panel from left to right is the cropped image, histogram of the red band, histogram of the green band and histogram of the blue band.

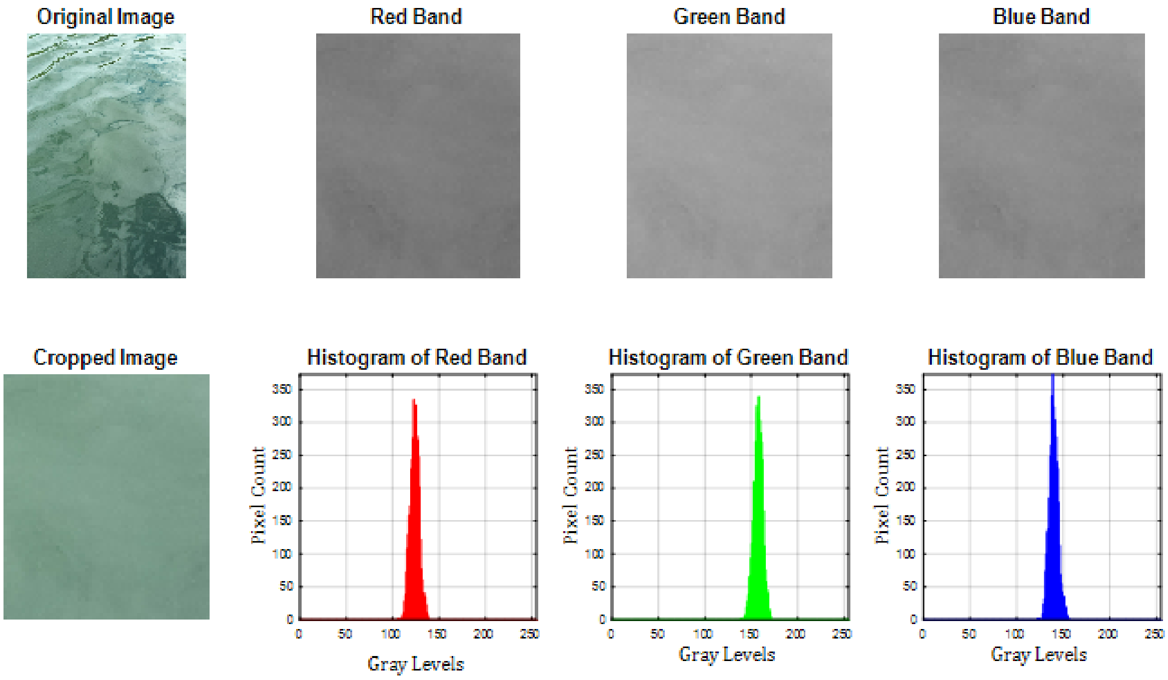

Figure 18: Derived RGB bands of water surface image taken at Hulsbeek Lake. The upper panel from left to right is the original image, the red band of the cropped image, the green band of the cropped image and blue band of the cropped image. The lower panel from left to right is the cropped image, histogram of the red band, histogram of the green band and histogram of the blue band.

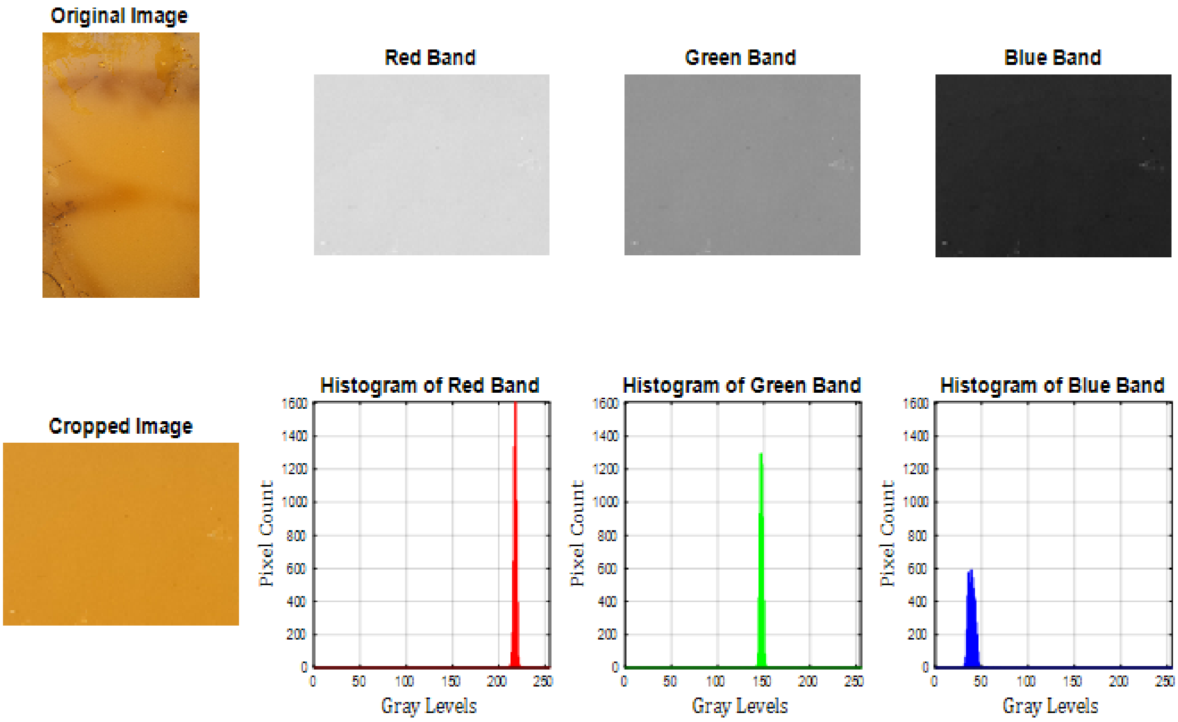

Figure 19: Derived RGB bands of water surface image taken at the CDOM dominated pit at Kristalbad artificial wetland. The upper panel from left to right is the original image, the red band of the cropped image, the green band of the cropped image and the blue band of the cropped image. The lower panel from left to right is the cropped image, histogram of the red band, histogram of the green band and histogram of the blue band.

6. HYDROCOLOR APP

6.1. Calibration of the Printed Grey Paper

The results from the printed grey paper images were corrected as described in Section 4.3.2. Scatter plots of the RGB bands obtained from the printed grey paper and the original grey card for the shadowed condition, sunny condition and for both conditions are as shown in Figure 20. The weather conditions under which the printed grey paper was used for Binnenschelde and Hulsbeek Lake were overcast and diffused skies respectively. This, the results for the shadowed condition was used for the correction. The expected grey card values for each site were then obtained base on Eq. (10).

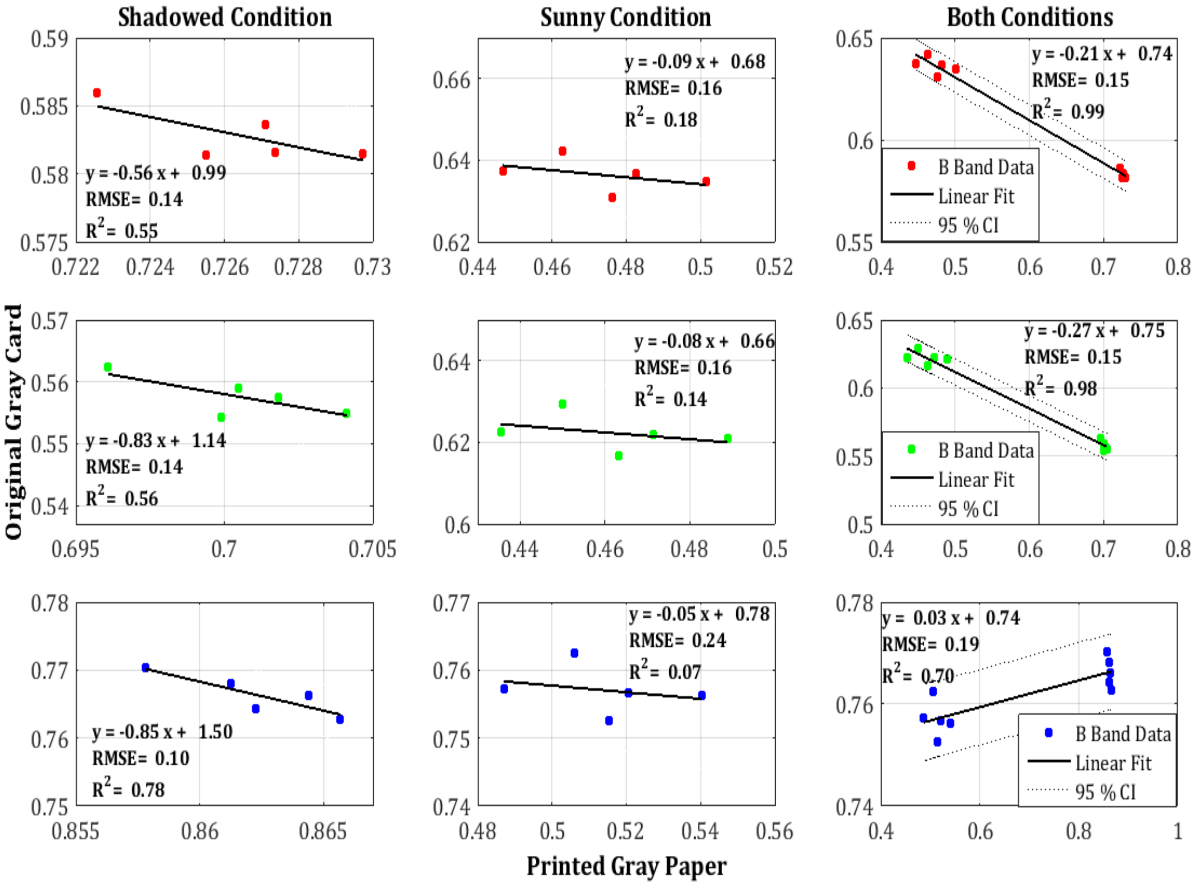

Figure 20: Scatter plot of printed grey paper versus original grey card under the shadowed condition, clear sky and sunny condition and for both conditions for the red (*R*), green (*G*) and blue (*B*) bands. The left panel is for the shadowed condition, middle panel for the sunny condition and the right panel for both conditions.

6.2. Comparison of RAMSES $R_{rs}(RGB)$ and Smartphone Images $R_{rs}(RGB)$

Using the three images (grey card, sky and water surface), the $R_{rs}(RGB)$ of each site was obtained as described in Section 4.3.2. Relations between the $R_{rs}(RGB)$ derived from RAMSES data and $R_{rs}(RGB)$ derived from the smartphone images are as shown in Figure 21. It was observed that the $R_{rs}(RGB)$ values obtained from RAMSES were higher than the $R_{rs}(RGB)$ obtained from the smartphone images. The resulting relations from this analysis were not good with percentage error PE of 69 %, 67 % and 77 % for the R, G and B bands respectively. The R^2 on the other hand was 0.22, 0.21 and 0.32 for R, G and B bands respectively. With the $R_{rs}(RGB)$ of the smartphone images, any scaling error from the smartphone camera would have been cancelled from the subtraction and division of the three images used in calculating the $R_{rs}(RGB)$ of the water surface (Leeuw, 2014). This, the primary source of error associated with the results was due to the convolution of the 2-degree field of view CMFs of CIE1931 with RAMSES $R_{rs}(\lambda)$ instead of the spectral response functions of the smartphone device used. The results obtained indicated that, the CIE1931 CMFs cannot be recommended as use in place of the spectral response function of a smartphone. First, $R_{rs}(RGB)$ is of the RGB colour space and depends on the sensitivity function of the device used. Thus, to make the result of the smartphone $R_{rs}(RGB)$ comparable to the $R_{rs}(RGB)$ of RAMSES, the convolution of RAMSES should have been done with the smartphone's spectral response. Secondly, the CMFs of the CIE1931 are illumination independent and are thus theoretical representation of the spectral response.

The maximum absolute variation between RAMSES $R_{rs}(RGB)$ and the smartphone images $R_{rs}(RGB)$ were obtained to be 0.022, 0.020 and 0.016 for the R, G and B bands respectively as indicated in Table 4.

Table 4: Statistical summary of the variation between RAMSES derived $R_{rs}(RGB)$ and smartphone images derived $R_{rs}(RGB)$. SD, standard deviation; CV, coefficient of variation; PE, percentage error.

Data		Minimum	Maximum	Median	Mean	SD	CV	PE
RAMSES versus Smartphone Images	R	6.6e-6	0.022	0.009	0.008	0.005	0.62	69
	G	5.1e-6	0.020	0.009	0.008	0.005	0.60	67
	B	4.9e-5	0.016	0.004	0.005	0.004	0.79	77

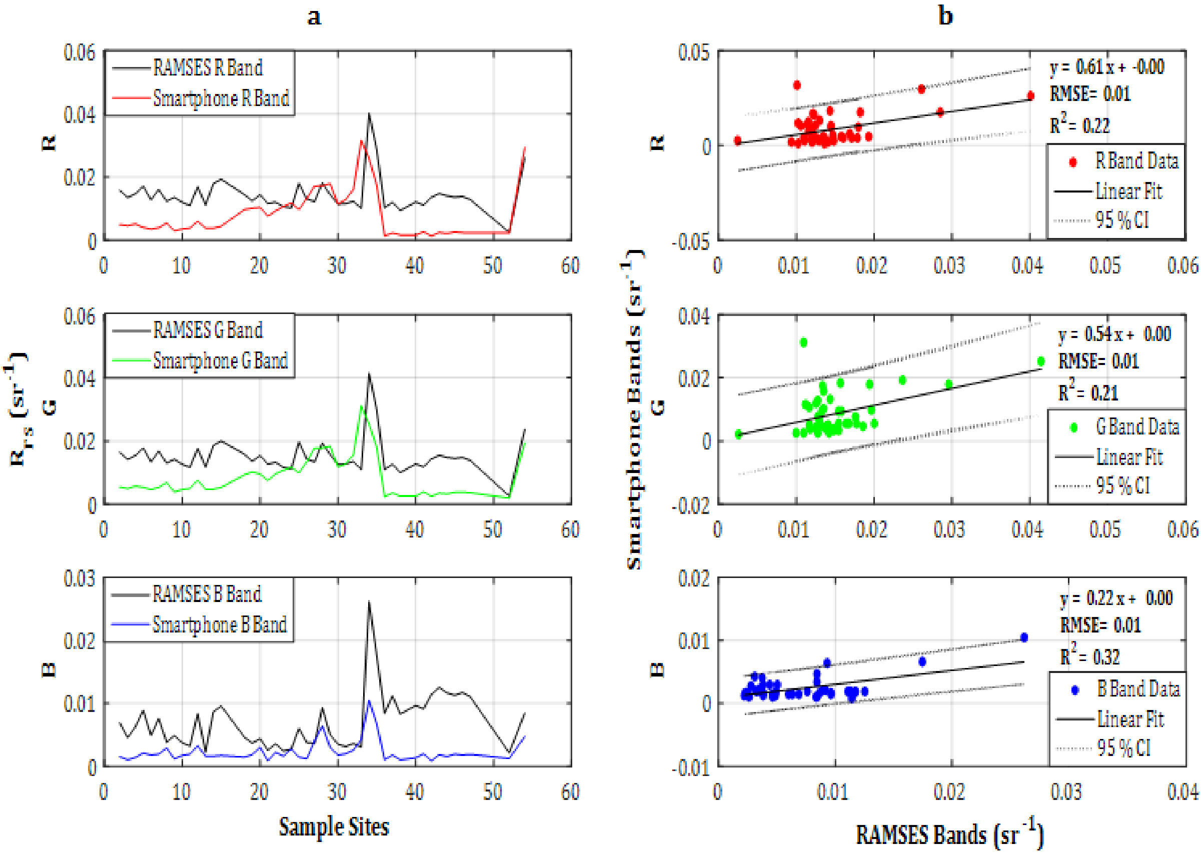

Figure 21: Relationship between derived RAMSES $R_{rs}(RGB)$ and smartphone images $R_{rs}(RGB)$ of the studied water bodies. (a) The variation of RAMSES and smartphone images $R_{rs}(RGB)$ with respect to sample sites. (b) The correlation between RAMSES $R_{rs}(RGB)$ versus smartphone images $R_{rs}(RGB)$.

6.3. Assessment of HydroColor APP Water Quality Variables

The relation between the laboratory measured turbidity and [SPM], and the red band reflectance $R_{rs}(R)$ of the smartphone images were determined by fitting two and three degree polynomial respectively as shown in Figure 22. For turbidity, the relation indicated an RMSE of 7.32 NTU with R^2 of 0.60. The relation for [SPM] also gave an RMSE of 15.08 gm^{-3} and R^2 of 0.89. It was this observed that turbidity and [SPM] influence the reflectance of the water bodies in the red band reflectance of the smartphone images. However, for the data sets used for this study, the relation only holds for turbidity less than 28 NTU with reflectance of 0.0165 sr^{-1} and [SPM] less than 128 gm^{-3} with reflectance of 0.015 sr^{-1}. The reflectance in the red band increased with increase in turbidity up to approximately 20 NTU before it turns to saturate. A similar (but not identical) dependence of turbidity and the red band reflectance was observed using iPod

Touch, iPhone 4 and iPhone 5 devices with the HydroColor APP by Leeuw (2014) and also for the red band wavelength 645 nm of a multispectral sensor product used by Dogliotti et al. (2015) in their research.

The lower correlation of the reflectance in the red band with turbidity than with [SPM] might be attributed to differences in particle size distribution within the water bodies (Neukermans et al., 2012). This is because; the turbidity meter uses the amount of backscattered light in its computation. For instance, Stramski et al. (2004) reported that homogeneous spherical particles smaller than 2.4 µm, contribute more to backscattering of water as they scatter light in equal intensities in all directions. Also, studies also indicate that particles larger than 302 µm may contribute more backscattering of water as particles larger than the wavelength of the light source used by the turbidimeter results in greater forward scattering (Hatcher et al., 2001). In this case, such an effect was likely to have been encountered for homogenously smaller particle size and larger particle size in the water samples used for the laboratory measurements. The results also indicated that in some case, as turbidity increased the reflected light in the red band decreased as observed in Figure 22.a. Research conducted by Binding et al. (2005) indicated that as particle scattering decrease with increase in the [SPM] of homogenously smaller particle size and of larger particle size, this causes a reduction in the water surface reflectance.

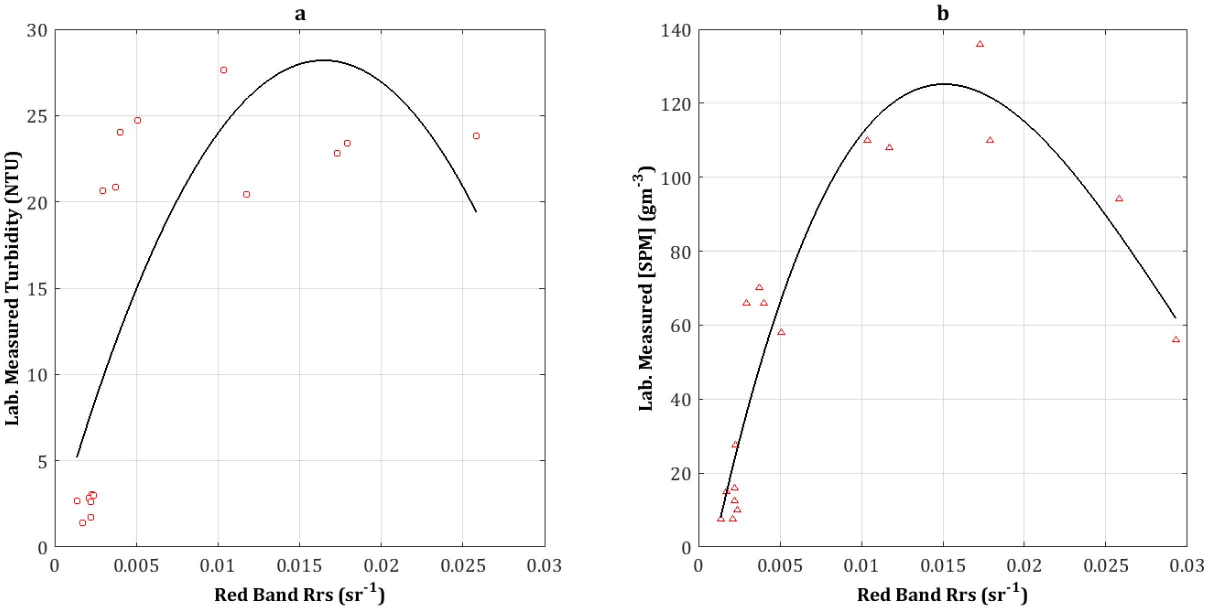

Figure 22: The relationship between laboratory measured turbidity and the [SPM], and the red band reflectance of the smartphone images. (a) Smartphone images red band reflectance versus lab measured turbidity. (b) Smartphone images red band reflectance versus lab measured [SPM].

Using the relation of the red band reflectance to turbidity and [SPM] as shown in Eq. (13 & 14), estimations of these water quality variables were obtained as specified for the HydroColor APP. Results of validation of the APPs models with the laboratory measurements is as shown in Figure 23. The results indicated a good correlation of R^2 = 0.68 and RMSE = 7.37 NTU for turbidity. The [SPM], on the order hand, gave a correlation of R^2 = 0.38 and RMSE = 10.75 gm^{-3}. It should however be noted that this results were based on using all the corresponding laboratory measurements of the smartphone images red band reflectance.

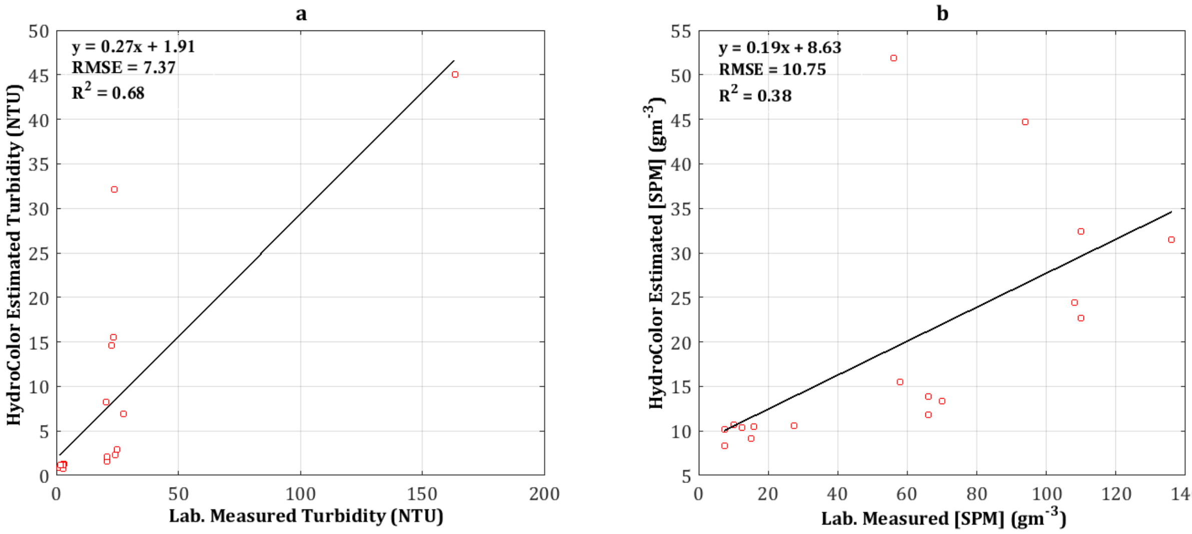

Figure 23: Validation of the original models used by HydroColor APP to estimate turbidity and the [SPM]. (a) Estimates of turbidity through the semi-analytical model of the HydroColor APP versus laboratory measured turbidity. (b) Estimates of the [SPM] through the logarithmic model of HydroColor APP versus laboratory measured [SPM]. The relations were based on all the corresponding red band reflectance of the smartphone images to laboratory measurements.

Based on the previous relation of the reflectance in the red band with turbidity and [SPM], reflectance values > 0.02 sr^{-1} were excluded from the data since the water quality variables estimates above this reflectance were considered not reliable. The relation between the laboratory measurements and the estimated smartphone images results were again determined. The results from this relation as shown in Figure 24 gave R^2 = 0.36 and RMSE = 4.13 NTU for turbidity while R^2 = 0.83 and RMSE = 3.44 for [SPM]. This indicated a decrease in the correlation between turbidity and an increase for [SPM] as compared to results of all the reflectance values of Figure 23.

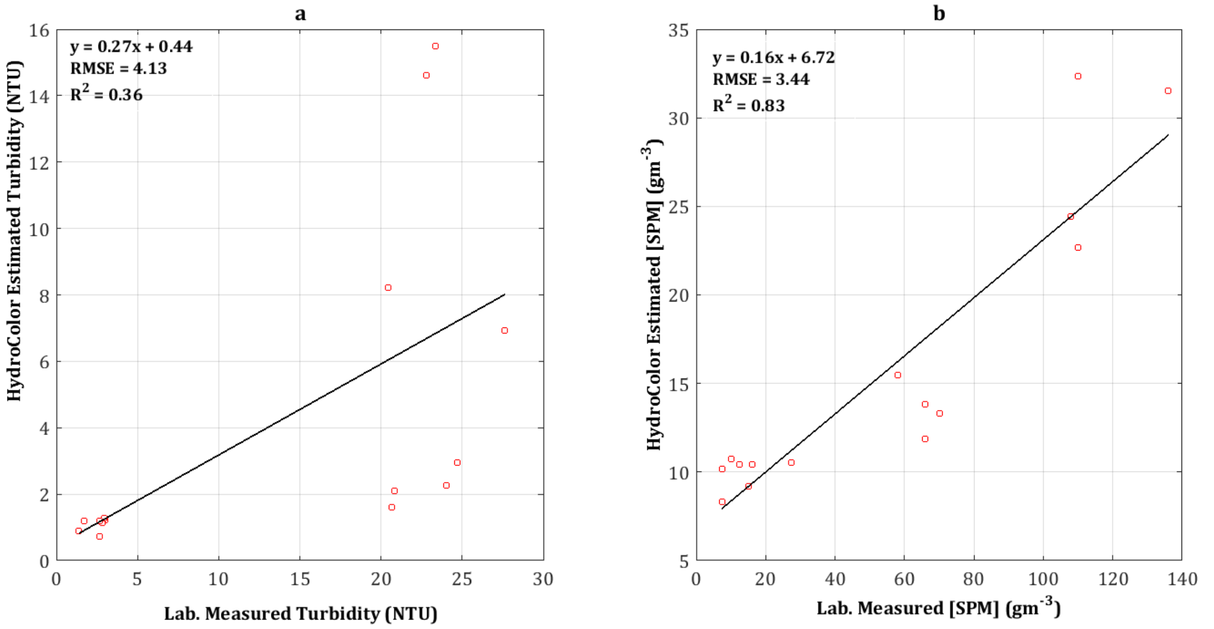

Figure 24: Validation of the original models used by HydroColor APP to estimate turbidity and [SPM]. (a) Estimates of turbidity through the semi-analytical model of HydroColor APP versus laboratory measured turbidity. (b) Estimates of the [SPM] through the logarithmic model of HydroColor APP versus laboratory measured [SPM]. The relations were based on measurements of the red band reflectance of the smartphone images < 0.02 sr^{-1}.

6.3.1. Limitation of HydroColor APP Models

The limit of the models used to estimate turbidity and [SPM] by the HydroColor APP were evaluated by varying the red band reflectance. From the turbidity model of Eq. (13), the saturation of the reflectance occurs at 0.044 sr^{-1} and the concentration of turbidity at half the saturation was 22.57 NTU. From the results obtained as shown in Figure 25.a, the estimate of turbidity starts at 0 when the red band reflectance = 0 sr^{-1}. As turbidity gets larger the red band reflectance approaches an asymptote at 0.044 sr^{-1}. The limit of turbidity estimate before the asymptote is approximately 4943 NTU. As can be seen from the Figure, the major limitation to this model is that reflectance values above the saturation limit of 0.044 sr^{-1} gives negative turbidity results. With the possibility of having to encounter a water system with reflectance ≥ 0.044 sr^{-1} which is typical of very turbid water dominated with CDOM or suspended mineral substance (Dierssen et al. 2006), this model would not be able to estimate the concentration of turbidity in such case. On a positive note, the results indicated that the model would give an estimate of turbidity and [SPM] no matter how small the optical signal received by the smartphone may be. For instance, the estimate of turbidity and [SPM] at a reflectance value of 0.0001 sr^{-1} gave 0.05 NTU and 0.04 gm^{-3} respectively. With such, the APP can be used on optically clear water systems.

In the same contest, since [SPM] is estimated from the concentration of turbidity as shown in Eq. (14) the estimation of [SPM] will fall under the same limitation. Thus, as shown in Figure 25.a for turbidity, a similar result would be obtained for [SPM] as shown in Figure 25.b. This is because the HydroColor APP model for turbidity and [SPM] has approximately 1 NTU : 1 gm^{-3} relation based on researches conducted by Neukermans et al. (2012) and Boss et al. (2009) as cited in Leeuw (2014). This would, therefore, give the results for these water quality variables to approximately overlap as observed in Figure 25.c. The limit of the [SPM] estimate before the asymptote specified for turbidity was therefore obtained to be approximately 5344 gm^{-3}. From the laboratory measurements indicated previously, the relation between turbidity and [SPM] was observed to be approximately 1 NTU : 4 gm^{-3}. In this case, the model used by HydroColor APP would underestimate the [SPM].

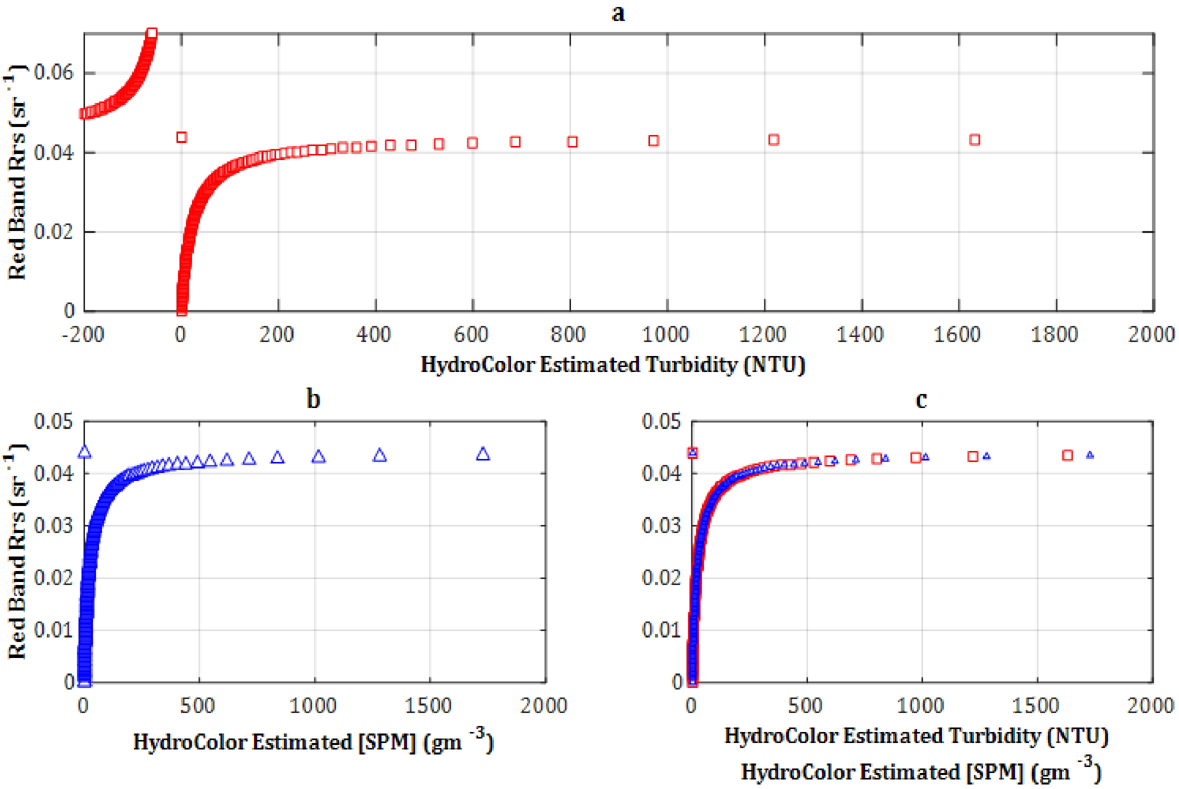

Figure 25: Simulation of the estimation of turbidity and [SPM] from the red band reflectance to determine the limitation of the original models used by HydroColor APP. (a) Estimated turbidity versus the red band reflectance. (b) Estimated [SPM] versus the red band reflectance. (c) The 1 NTU : 1 gm^{-3} relation of turbidity and [SPM] applied by HydroColor APP showing an overlap of the two estimated water quality variables.

6.4. Alternative Approaches for Estimating [SPM]

From the results obtained and its associated limitations in using the models specified by HydroColor APP, alternative approaches to estimating [SPM] and turbidity were sort. Starting with [SPM], the estimation of the [SPM] directly from the red reflectance band based on the single band relation between [SPM] and reflectance proposed by Novo et al. (1989) was used. This was by first using the single band nonlinear relation of the Kabelka-Munk theory of reflectance as proposed by Nechad et al. (2010) and hereafter referred to as Nechad model. This was applied to the dataset with the red band reflectance < 0.02 sr^{-1}. The results of the model coefficients indicated as PD_c are as shown in the upper panel of Figure 26. The model coefficients were determined over a range with the associated probability that the "true" model results would be within the interval. This was to avoid any substantial errors associated with point estimate of model parameters (Haan et al., 1998). Taking the mean of these estimates, the resulting model was therefore as shown in Eq. (43). Using type II linear regression to validate the model with the Val data sets; the slope, intercept, MAE and R^2 were determined with the resulting PD_v as shown in the middle and lower panel of Figure 26. The mean of the estimated slope, intercept, MAE and R^2 were 1.32, -17.13, 24.97 gm^{-3} and 0.80 respectively.

$$[SPM] = \frac{1594.75 \times R_{rs}(R)}{0.18 + R_{rs}(R)} \tag{43}$$

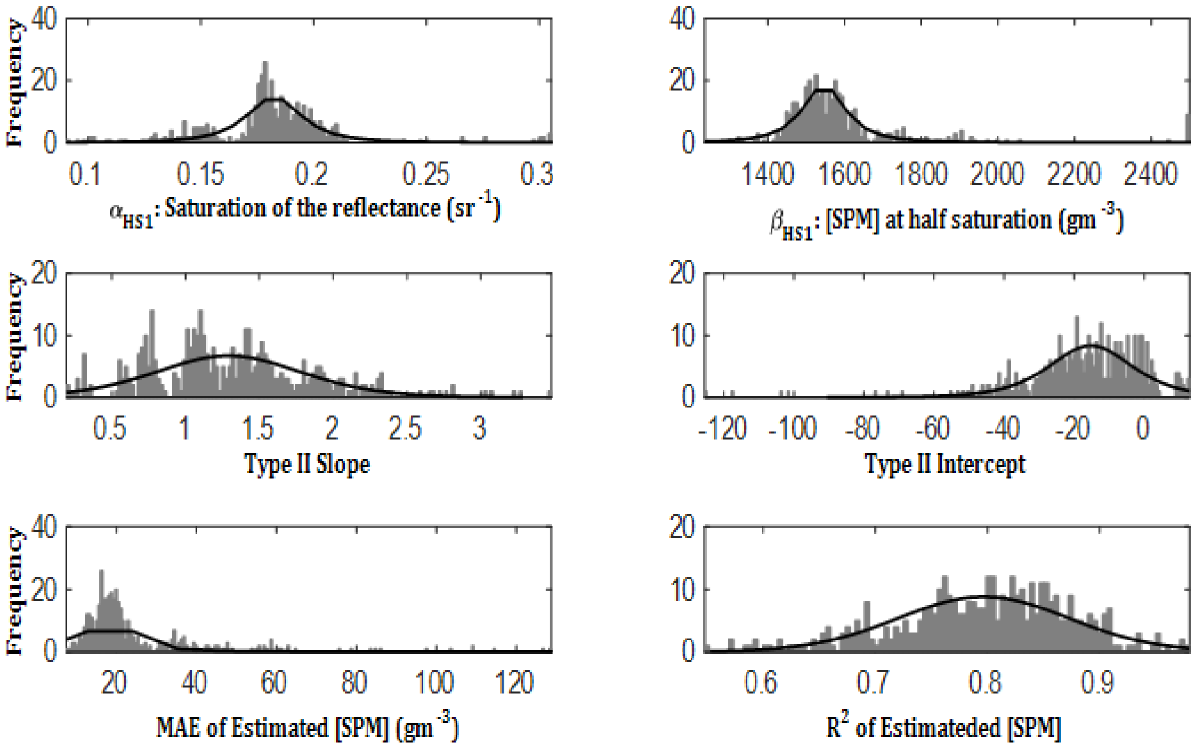

Figure 26: Probability distributions of the derived Nechad model coefficients α_{HS1} and β_{HS1} (upper plots) the slope and intercept of the type II linear regression (middle plots), the MAE and R^2 (lower plots).

Previous research of Myint & Walker (2002) also used linear models to relate the [SPM] and the red band reflectance. Thus, a linear model was used to predict [SPM] from the log transformed red band reflectance and hereafter called the logarithmic model. The results of the model calibration are as shown in the upper panel of Figure 27. The resulting model was therefore as shown in Eq. (44). On validating the model with the Val data sets, the mean of the slope, intercept, MAE and R^2 were obtained as 1.08, -4.00, 15.68 gm^{-3} and 0.90 respectively. The results of the validation parameters are as shown in the middle and lower panel of Figure 27.

$$[SPM] = \frac{\log(R_{rs}(R)) + 6.51}{0.02} \tag{44}$$

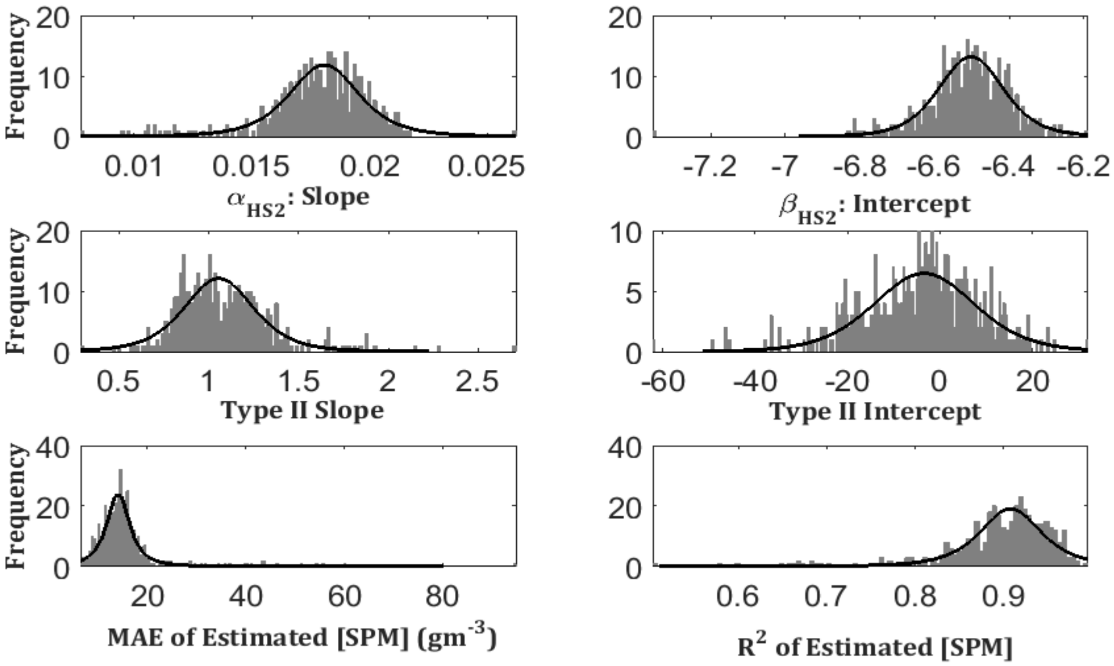

Figure 27: Probability distributions of the derived logarithmic model coefficients α_{HS2} and β_{HS2} (upper plots) the slope and intercept of the of type II linear regression (middle plots), the MAE and R^2 (lower plots).

The relation between the laboratory measurements and the model estimates for all the corresponding measurements are as shown in Figure 28. For the Nechad model, the results obtained indicated an R^2 of 0.78 and RMSE of 27.29 gm^{-3}. From the results, such a model gave more error and was less accurate as compared to the original model used by the HydroColor APP. The logarithmic model, on the order hand, gave a better estimate of [SPM] with R^2 of 0.90 and an RMSE 15.34 gm^{-3}. With the logarithmic model, it was also observed that reflectance values less than 0.0014 sr^{-1} of the studied data set gave negative estimates of [SPM]. This implies that, a water body with [SPM] of approximately 7.5 gm^{-3} of the studied water bodies would not be appropriate to use the logarithmic model in its prediction.

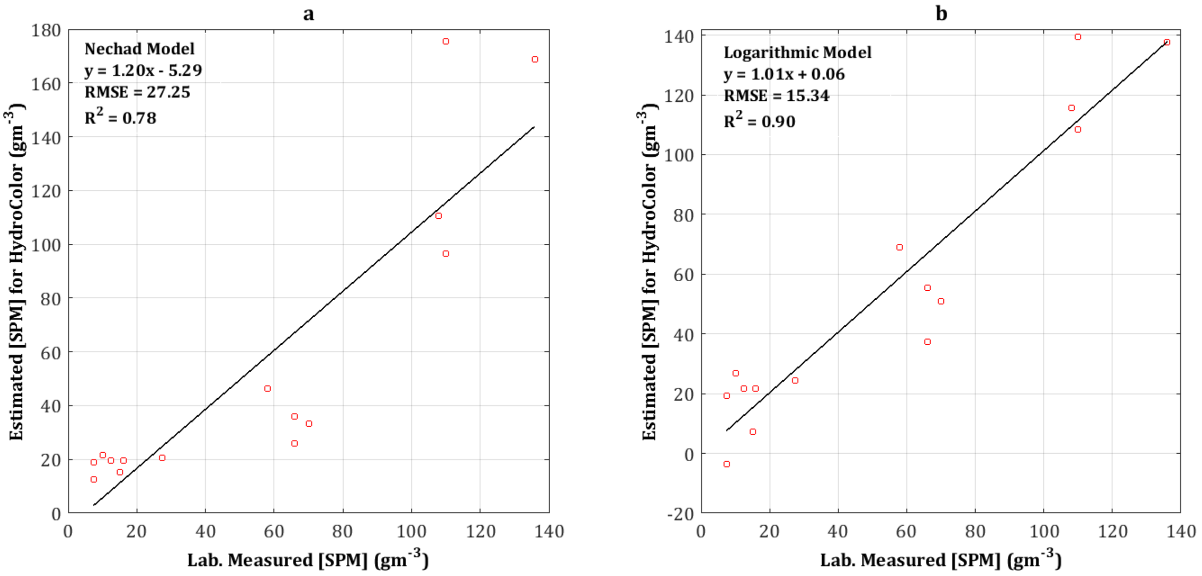

Figure 28: Validation of the proposed models for the HydroColor APP in estimating [SPM]. (a) Estimated [SPM] of the proposed semi-analytical model of Nechad et al. (2010) versus laboratory measured [SPM]. (b) Estimated [SPM] of the proposed logarithmic model versus laboratory measured [SPM]. The relations were based on measurements of the red band reflectance <0.02 sr^{-1}.

6.4.1. Limitation of the Proposed HydroColor [SPM] Models

The limit of the Nechad and logarithmic models for estimating [SPM] using the red band reflectance of smartphones images proposed to be used by HydroColor APP were evaluated by varying the red band reflectance. For the Nechad model, the saturation of the red band reflectance occurred at 0.18 sr^{-1} and the [SPM] at half the saturation was 1595 gm^{-3}. From the results obtained as shown in Figure 29.a, the estimate of the [SPM] gets larger as the red band reflectance approaches an asymptote of 0.18 sr^{-1}. Estimates of the [SPM] above the saturation limit would thus give negative values. Also [SPM] at 0.044 sr^{-1} gave 151 gm^{-3} as compared to 22.57 gm^{-3} of the original model used by the HydroColor APP. If the Nechad model proposed is to be used, the APP would still be able to give good estimates of [SPM] at reflectance > 0.044 sr^{-1} which in the case of the original model is the saturation limit.

For the logarithmic model, it was observed that the model was limited to reflectance values ≥ 0.001491 sr^{-1}. Figure 29.b this showed that reflectance values less than the limit gave negative estimates of [SPM]. At reflectance value of 0.1 sr^{-1}, the [SPM] estimate was 236 gm^{-3}. This model was therefore observed to be only limited by low reflectance values which can be attributed to clear water systems.

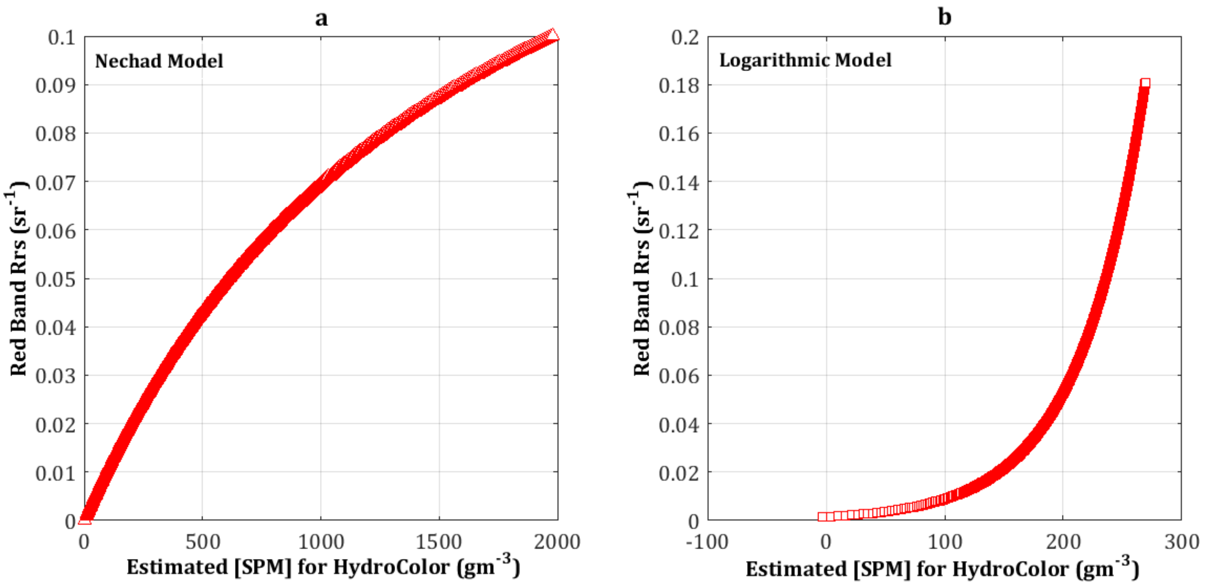

Figure 29: Simulation of the estimation of the [SPM] from the red band reflectance to determine the limitation of the proposed models for HydroColor APP. (a) Semi-analytical model of Nechad et al. (2010) estimated [SPM] versus the red band reflectance. (b) The logarithmic model estimated [SPM] versus the red band reflectance.

6.5. Alternative Approaches for Estimating Turbidity

Based on the results from the HydroColor APP, alternative approaches were assessed to estimate turbidity using the same models applied on [SPM] through the red band reflectance. This was because; from the previous analysis the relation of turbidity and [SPM] gave a good correlation of R^2 0.79. Previous studies also proposed that because of the strong correlation between these two water quality variables, the same model can be designed and apply equally to both (Nechad et al., 2010). Quite apart research conducted by Kallio et al. (2001) also concluded that the best model for the estimation of turbidity is the single band (red) since the impact of other optical water constituents are small. A single band semi-analytical model has thus been developed to relate remote sensing reflectance to turbidity (Nechad et al., 2009). Based on these reasons, the red band reflectance of the smartphone images were used to relate to the measured turbidity. This was done by using the Nechad and logarithmic models as applied on [SPM] to derive their coefficients and validated using the laboratory measurements. The results of the correlation of the laboratory measurements and the estimated turbidity from these models are as shown in Figure 30. The results of the logarithmic model gave an RMSE of 6.65 NTU and an R^2 of 0.63. The Nechad model, on the other hand, gave an RMSE of 6.17

NTU and R^2 of 0.45. The models of Eq. 45 and 46 were obtained for the Nechad and logarithmic model respectively.

$$Turb = \frac{10.16 \times R_{rs}(R)}{0.023 + R_{rs}(R)} \tag{45}$$

$$Turb = 12.47 \times log(R\_rs\ (R)) + 82.58 \tag{46}$$

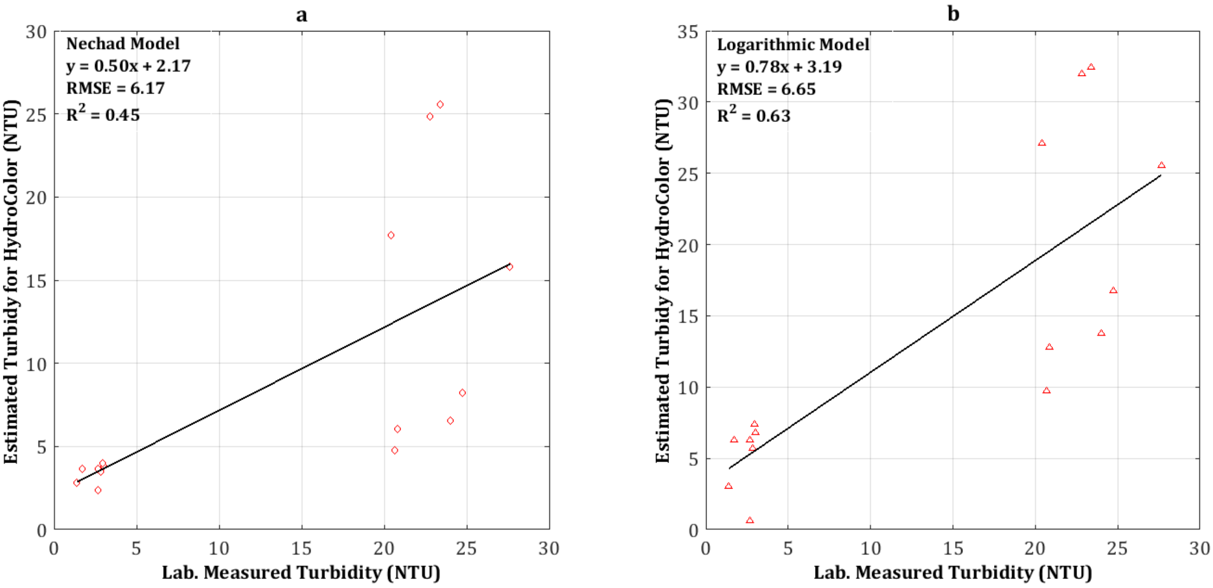

Figure 30: Validation of the proposed models for HydroColor APP in estimating turbidity. (a) Estimates of the proposed semi-analytical model by Nechad et al. (2009) versus laboratory measurements. (b) Estimates of the proposed logarithmic model versus laboratory measurements. The relations were based on measurements of the red band reflectance < 0.02 sr^{-1}.

6.5.1. Limitation of the Proposed Turbidity Models

The limit of the proposed Nechad and logarithmic models for estimating turbidity via the HydroColor APP using the red band reflectance were evaluated by varying the red band reflectance. For the Nechad model of Figure 31.a, the saturation of the red band reflectance occurred at 0.023 sr^{-1} and turbidity at half the saturation was 10.16 NTU. Any other limitation that applied to the Nechad model of the [SPM] would equally affect turbidity because they both use the same parameterization. The saturation limit as well as turbidity estimate at half the saturation was observed to be low as compared to the original model used by the HydroColor APP. This was because of the low values of turbidity (≤ 24 NTU) for red band reflectance < 0.02 sr^{-1} used to calibrate the model.

For the logarithmic model, it was observed that the model was limited to reflectance values ≥ 0.00134 sr^{-1}. Figure 31.b this indicated that reflectance values less than the limit gave negative estimates of turbidity. The turbidity estimate for this model was observed to be low which could be related to the low values used in the calibration which also occurred in the Nechad model.

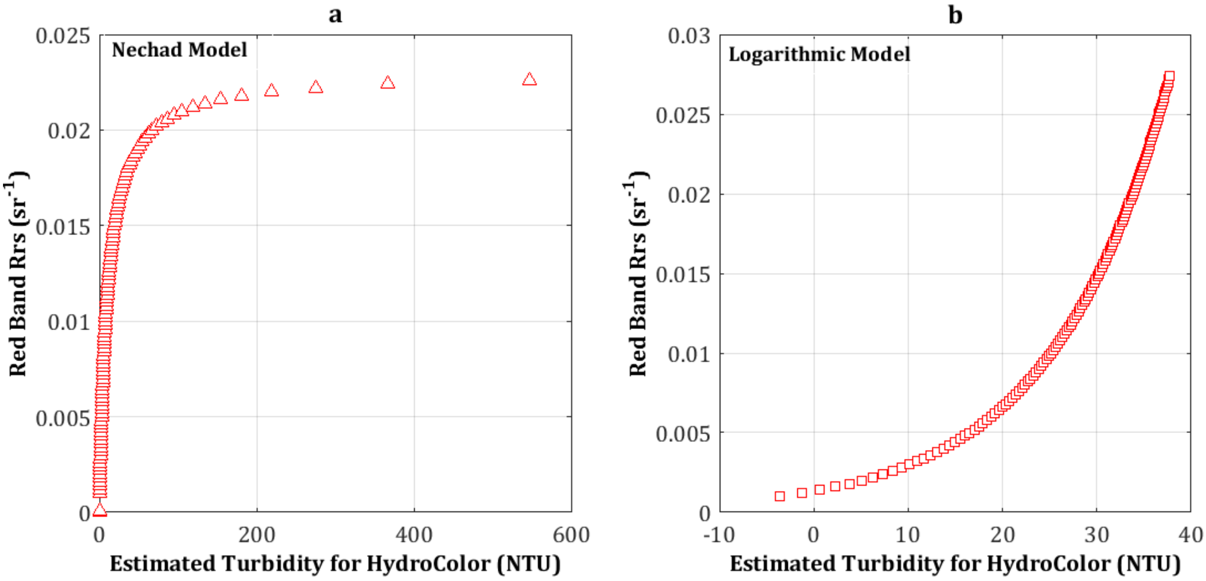

Figure 31: Simulation of the estimation of turbidity from the red band reflectance to determine the limitation of the proposed models for HydroColor APP. (a) Semi-analytical model of Nechad et al. (2009) estimated turbidity versus the red band reflectance. (b) The logarithmic model estimated turbidity versus the red band reflectance.

6.6. Error Quantification of the HydroColor APP Models

Both turbidity and the [SPM] model parameters were evaluated for their uncertainties as described in Section 4.3.5. It was observed that for the [SPM] the total error of the logarithmic model was 48.65 and the Nechad model was 48.41. The total error for turbidity was also observed to be 20.43 for the logarithmic model and 20.04 for the Nechad model. From the two models of the [SPM] and turbidity, the total error propagated for the logarithmic models were higher than the Nechad models. Also, because each of the model parameters has an uncertainty about its mean, the square root of the partial derivative of their mean and their standard deviation was used to obtain the error in each parameter from the resulting Eqs. (43, 44, 45 and 46). The percentage of each models' parameters error to the total error of each model indicated in pie charts are as shown in Figure 32. It was observed that the error in $R_{rs}(R)$ derived from the smartphone images contributed the most to the error incurred in estimating

[SPM]. The error in estimating turbidity for the Nechad model was affected by the reflectance saturation limit α_{HT1} followed by the $R_{rs}(R)$. The logarithmic model, on the other hand, for turbidity was affected by the intercept β_{HT2} followed by the $R_{rs}(R)$. Generally, the values of the derived $R_{rs}(R)$ affects the estimation of the water quality variables studied. This could be due to the variation in the water types studied.

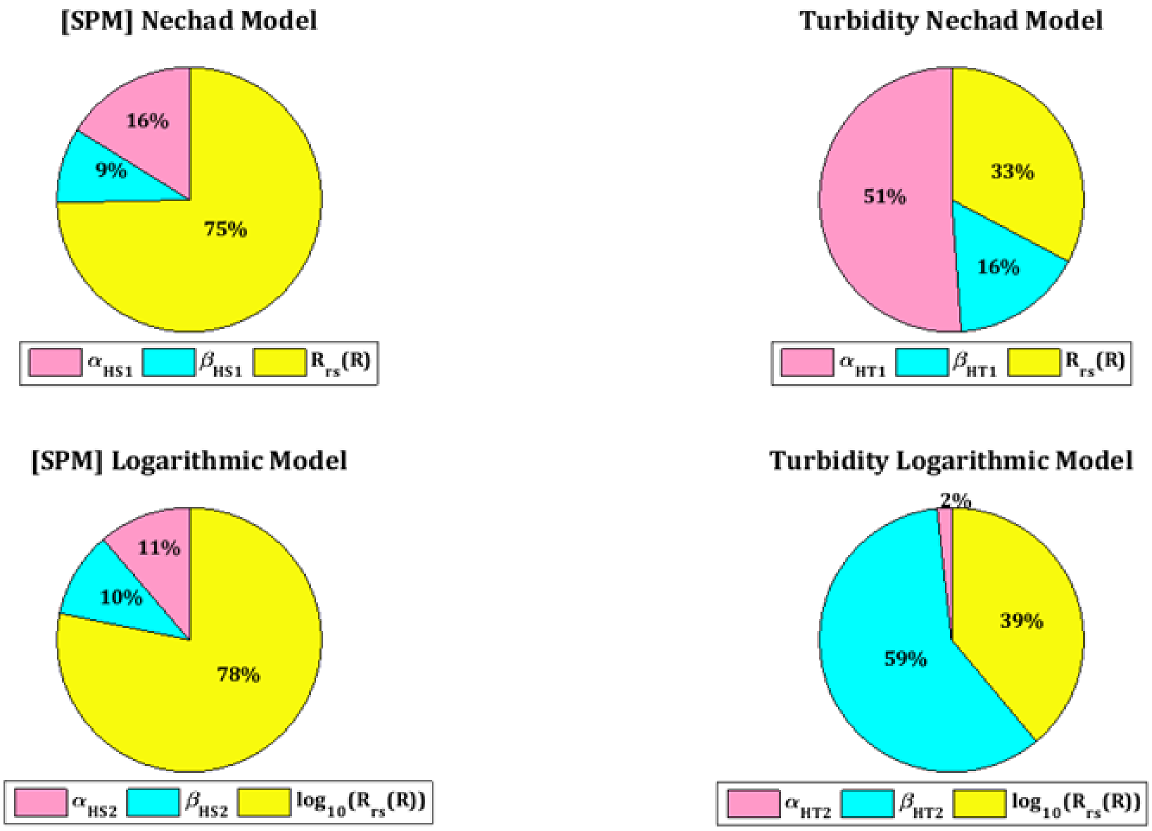

Figure 32: Pie charts of the relative contributions of the error in the models parameters proposed for the HydroColor APP shown as percentages, % with respect to the total error of each model. The upper left panel indicates the errors in % of the Nechad model parameters in estimating [SPM]. The lower left panel indicates the errors in % of the logarithmic model parameters in estimating [SPM]. The upper right panel indicates the errors in % of the Nechad model parameters in estimating turbidity. The lower right panel indicates the errors in % of the logarithmic model parameters in estimating turbidity.

6.7. Accuracy of the HydroColor APP Models

The accuracy of the original models used by HydroColor APP and the proposed Nechad and logarithmic models in estimating turbidity and [SPM] were determined by their R^2 and MAE. The results are as shown in bar charts of Figure 33. It was observed that the logarithmic model was the best for the estimation of [SPM] with R^2 = 0.90 and MAE =

11.66 gm^{-3}. For the turbidity models, the logarithmic model was also the best with R^2 = 0.63 and MAE = 5.82 NTU.

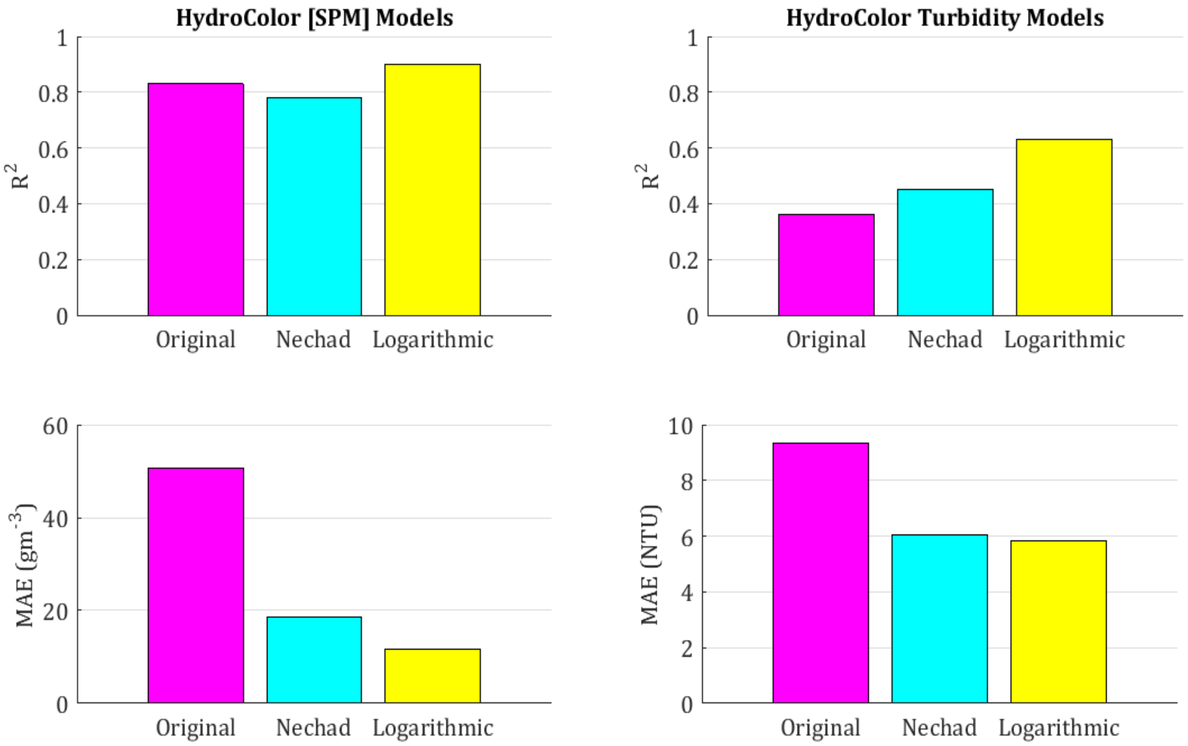

Figure 33: Bar charts of the accuracy of the original HydroColor APP models and the proposed HydroColor APP models estimate of turbidity and [SPM] compared to laboratory measurements. The upper left panel indicates the R^2 of the models for estimated [SPM] after validating with lab measured [SPM]. The lower left panel indicates the MAE of the models for estimated [SPM] after validating with lab measured [SPM]. The upper right panel indicates the R^2 of the models for estimated turbidity after validating with lab measured turbidity. The lower right panel indicates the MAE of the models for estimated turbidity after validating with lab measured turbidity.

7. CITCLOPS APP

7.1. Comparison of RAMSES xyz and Smartphone Images xyz

The correlation of RAMSES *xyz* chromaticity coordinates and the smartphone images *xyz* chromaticity coordinates are as shown in Figure 34. The *xyz* chromaticity coordinates of RAMSES and the smartphone images showed a correlative pattern for the sample sites as shown on the left panel of the Figure. The maximum absolute variation between the two devices were obtained to be 0.101, 0.058 and 0.159 for x, y and z respectively as indicated in Table 5. The results of the correlation also indicated the highest value(s) of; x chromaticity coordinate at the CDOM dominated water site, y chromaticity coordinate for chlorophyll-a pigment dominated water sites and z chromaticity coordinate at the clear water sites. Scatter plots of the *xyz* chromaticity coordinates of RAMSES and the smartphone images are as shown on the right panel of Figure 34. The figure indicates a correlation of R^2 0.65, 0.70 and 0.67 respectively for x, y and z. the PE were also 9.69 %, 0.07 % and 22 % respectively for x, y and z.

Table 5: Statistical summary of the variation between RAMSES derived *xyz* chromaticity coordinates and smartphone images derived *xyz* chromaticity coordinates. SD, standard deviation; CV, coefficient of variation; PE, percentage error.

Data		Minimum	Maximum	Median	Mean	SD	CV	PE
RAMSES versus Smartphone Images	x	0.009	0.101	0.039	0.041	0.022	0.530	9.69
	y	0.0003	0.058	0.021	0.022	0.016	0.747	0.07
	z	0.002	0.159	0.041	0.049	0.040	0.827	22

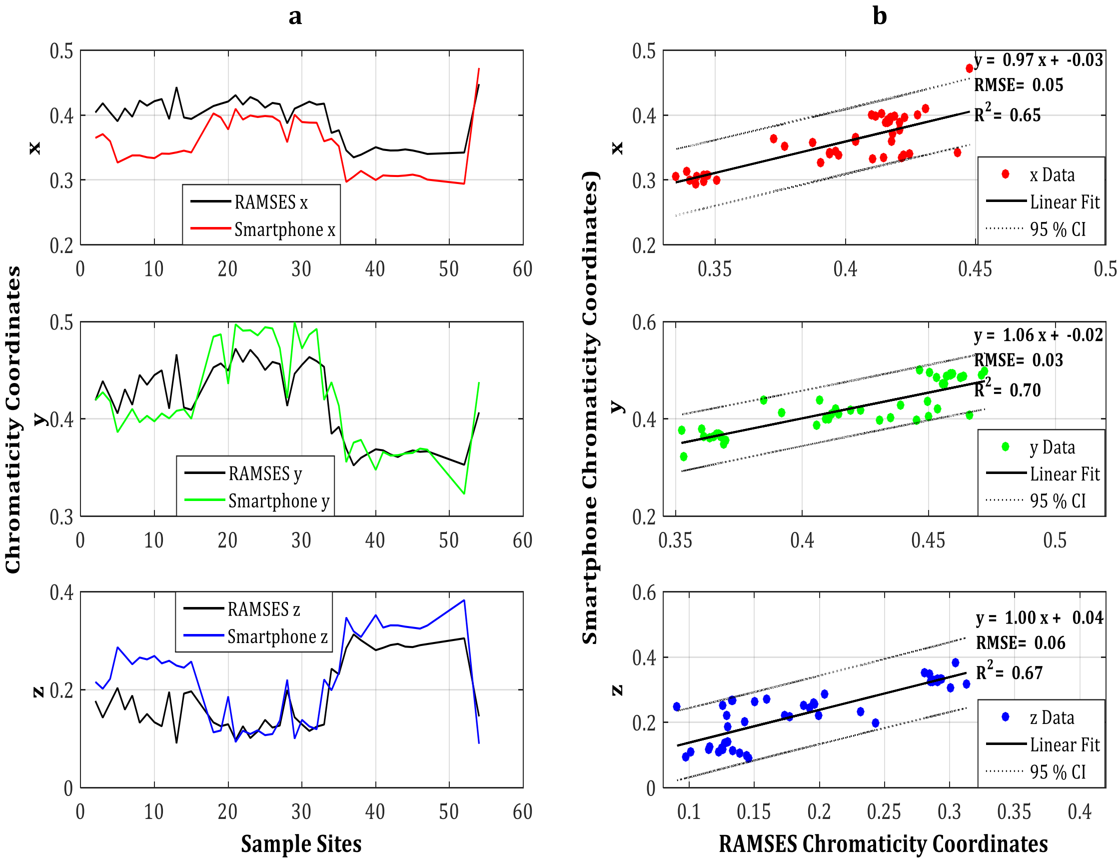

Figure 34: Relationship between RAMSES *xyz* chromaticity coordinates and smartphone images *xyz* chromaticity coordinates. The *x* data is specified by red, *y* data by green and the *z* data by blue. The left panel of the figure, (a) indicates the plot of the *xyz* chromaticity coordinates versus the sample sites. On the right panel, (b) are the scatter plots of the *xyz* chromaticity coordinates of RAMSES versus the smartphone images.

An illustration of selected *xy* chromaticity coordinates of RAMSES and the smartphone images are as shown in a chromaticity diagram of Figure 35. The Figure indicates the derived chromaticity coordinates of the devices with respect to the chromaticity coordinates that were developed from laboratory FU solution transmission measurements by Novoa et al. (2013). It was observed that the chromaticity coordinates of RAMSES were closer to the white point, WP as compared to the smartphone images chromaticity coordinates. The closeness of RAMSES chromaticity coordinates to the WP indicated that its resulting colours were less saturated as compared to the smartphone images. This could be as a result of the gamma expansion that was applied on the smartphone images. By gamma expansion with a value of 2.2, the colour of the output smartphone images became saturated with the enhancement of their gray level.

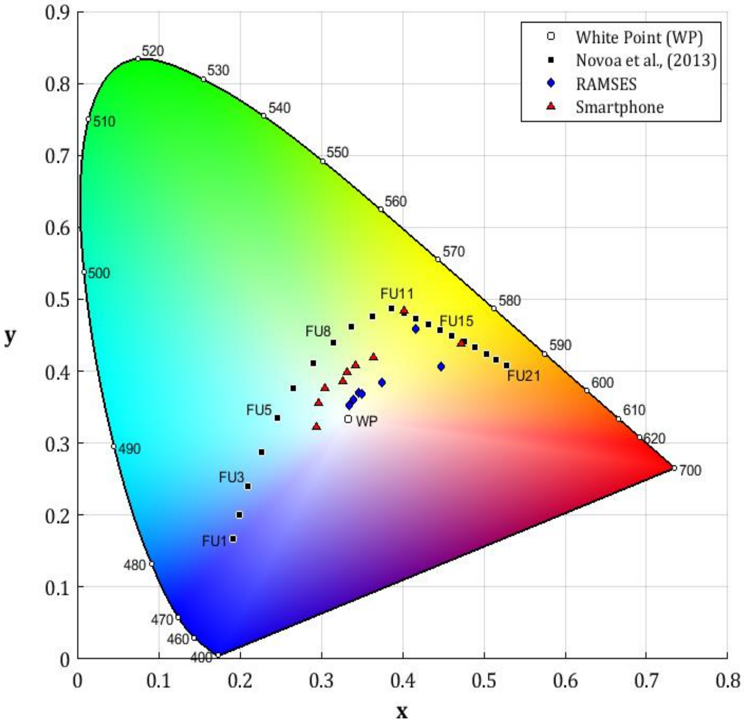

Figure 35: Illustration of the xy chromaticity coordinates derived from RAMSES and the smartphone images on a chromaticity diagram. This is compared to the chromaticity coordinates that were developed from laboratory FU solution transmission measurements by Novoa et al. (2013). The white point of the chromaticity coordinate is indicated as WP.

7.2. Hue Colour Angles and Forel-Ule Index

Statistical summary of the $\alpha_P(°)$ and FUI that were derived from RAMSES and the smartphone images are as shown in Table 6. This indicated that, the $\alpha_P(°)$ derived from RAMSES data range 32.68° to 85.47°. The FUI of RAMSES also ranged 9 to 18. The $\alpha_P(°)$ of the smartphone images ranged from 36.90° to 156.85° and the FUI ranged from 6 to 17.

Table 6: Statistical summary of the hue colour angles, $\alpha_P(°)$ and Forel-Ule Index (FUI) derived from RAMSES and the smartphone images. SD, standard deviation; CV, coefficient of variation; PE, percentage error.

Data	Minimum	Maximum	Median	Mean	SD	CV	PE
RAMSES $\alpha_P(°)$	32.68	85.47	55.55	57.40	9.74	0.17	38.4
Smartphone $\alpha_P(°)$	36.90	156.85	76.91	87.89	28.05	0.32	
RAMSES FUI	9	18	14	13.37	1.66	0.12	26.7
Smartphone FUI	6	17	10	9.89	2.38	024	

Comparison of the $\alpha_P(°)$ and FUI derived from RAMSES and the smartphone images are as shown in Figure 36. With the $\alpha_P(°)$ it was observed that 98 % of the data were within the 95% confidence interval (CI). The R^2 obtained was 0.63 and an RMSE of 17.20°. Figure 36 also indicated that, the $\alpha_P(°)$ of the data set within the third quartile were more dispersed. This could be due to the high angular differences existing in the blue to cyan hue colour angles as can be seen in Figure 10**.** Quite apart, the water system that was characterised by these angles was the clear water body of Hulsbeek Lake with measurements taken under a fluctuation weather condition. The effect of such fluctuating weather condition could have also caused a significant influence on the water surface reflectance which in this case resulted in varying angles.

For the FUI, 100 % of the data were within the 95 % CI. The correlation between RAMSES and the smartphone images gave R^2 of 0.70, RMSE of 1.32 and PE of 26.7. The consistency in the FU 14 for the RAMSES data was for Binnenschelde and Markiezaatsmeer Lake which had similar water characteristics. It was therefore expected to have the same range of FUI as was observed from RAMSES (considered to be the true results).

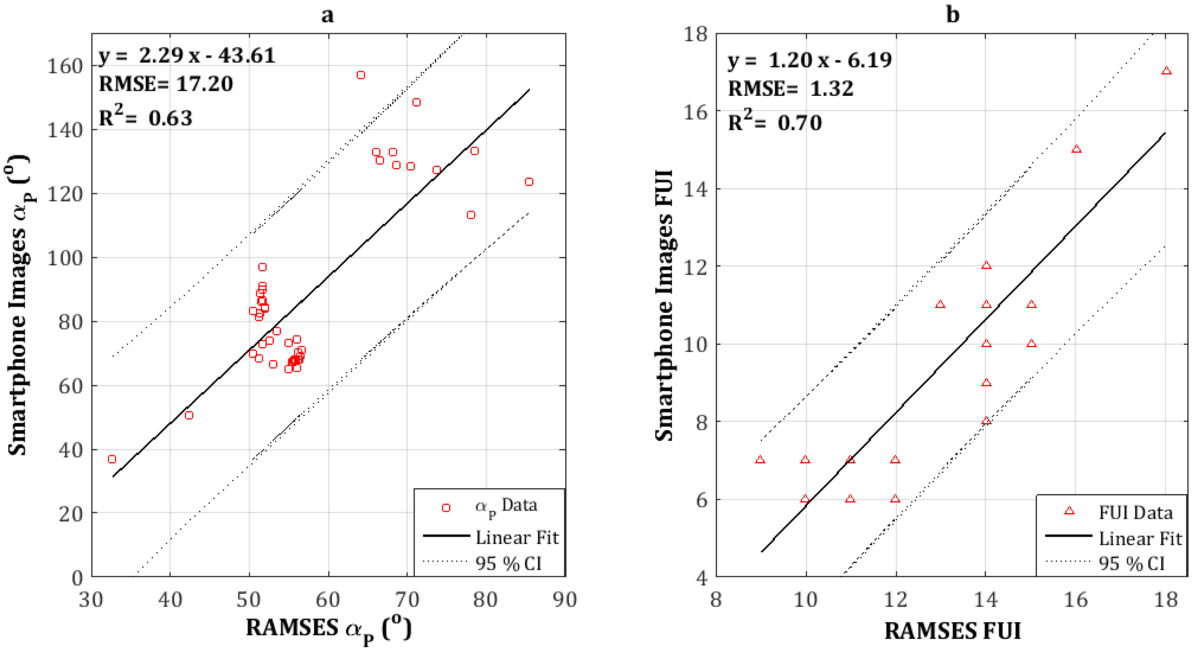

Figure 36: Relationship between the hue colour angle $\alpha_P(°)$ and Forel-Ule Index (FUI) derived from RAMSES and the smartphone images. (a) Scatter plot of the $\alpha_P(°)$ derived from RAMSES and the smartphone images with a linear fit (full line) and the 95 % confidence interval (dotted line). (b) Scatter plot of the FUI derived from RAMSES and the smartphone images with a linear fit (full line) and the 95 % confidence interval (dotted line).

Variations in $\alpha_P(°)$ as seen from Figure 36 caused significantly the derived FUI. To identify such areas of $\alpha_P(°)$, deviation, Δ of the smartphone images from RAMSES (considered to be the true measurement) were determined. This was by subtracting the $\alpha_P(°)$ of the smartphone images from RAMSES $\alpha_P(°)$. The Δ of $\alpha_P(°)$ with respect to the sample sites is as shown in Figure 37.a. It was observed that, there was much variation in the sample sites of Hulskeeb Lake up to -92.71°. A summary of the deviation of the smartphone images from RAMSES $\alpha_P(°)$ and FUI are as shown in Table 7.

Table 7: Statistical summary of the deviation, Δ of smartphone images hue colour angle $\alpha_P(°)$ and Forel-Ule index (FUI) from RAMSES.

Smartphone Images Deviation, Δ	Minimum	Maximum	Median	Mean
Δ of $\alpha_P(°)$	-4.21	-92.71	-23.37	-30.49
Δ of FUI	1	6	3	3.49

Generally, Figure 37.b indicated that $\alpha_P(°) > 100°$ gave most of its deviation > -50°. From Figure 10, $\alpha_P(°) > 100°$ correspond to FUI from 7 to 1. It was this observed that FUI derived with $\alpha_P(°) > 100°$ gave much variation in FUI as shown in Figure 37.c. Such disparity in $\alpha_P(°)$ which subsequently affected the FUI of Hulsbeek Lake could be attributed to its fluctuation in weather condition. Also, its RAMSES $R_{rs}(\lambda)$ were not corrected for sky glint effects which could contribute to such deviation because of the clear start of the water at the time the study was conducted.

The Hulsbeek Lake results were thus removed from the data set and the remaining $\alpha_P(°)$ used to develop a model on which Δ of the smartphone images $\alpha_P(°)$ from the "true" $\alpha_P(°)$ of RAMSES was obtained. This was by fitting a 3 degree polynomial function to the data set. The results obtained indicated a good fit with an R^2 of 0.97 and RMSE of 2.00° as shown in Figure 37.d with the resulting model shown in Eq. (47).

$$\Delta_{\alpha_p}(°) = 0.0003x^3 0.0757x^2 + 5.144x - 107.8 \tag{47}$$

It should, however, be noted that this deviation factor, $\Delta_{\alpha_p}(°)$ cannot be applied on $36.896° < \alpha_P(°) > 99.991°$. Thus, $\alpha_P(°)$ derived outside this interval with the addition of the $\Delta_{\alpha_p}(°)$ will give inaccurate results.

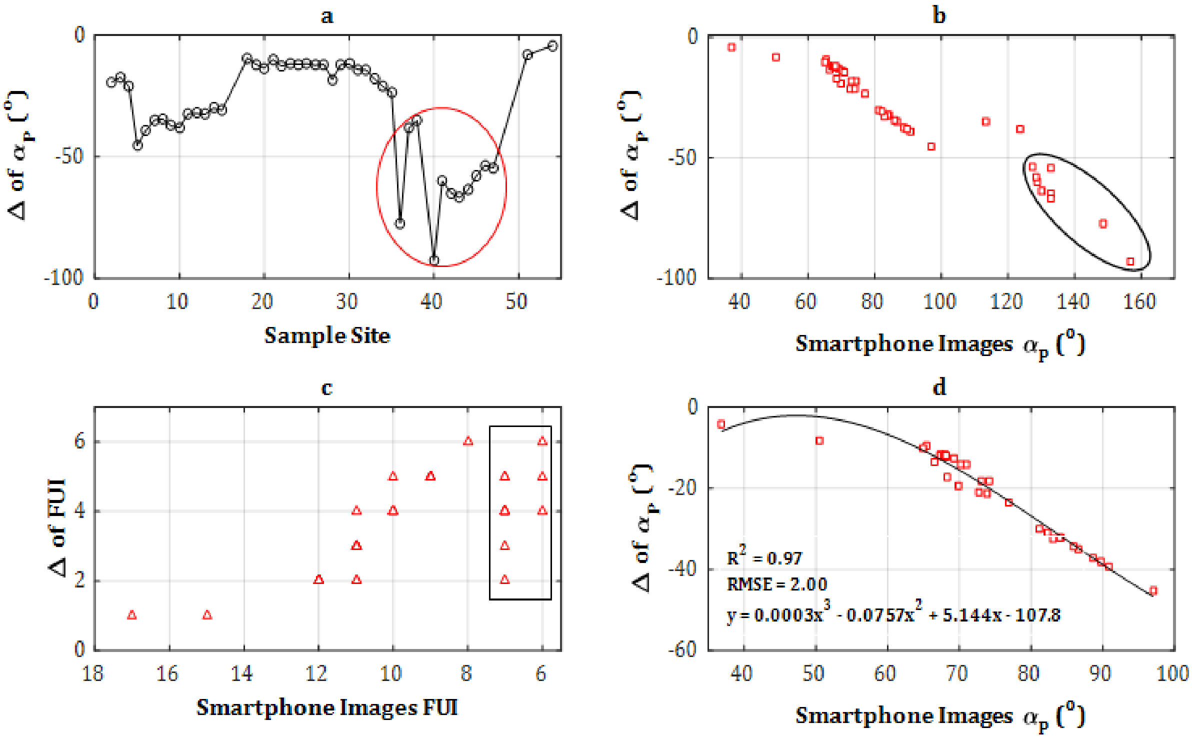

Figure 37: Deviation, Δ of the smartphone images hue colour angles α_P(°) and Forel-Ule index (FUI) from RAMSES. (a) Derived Δ of the smartphone images α_P(°) with respect to sample sites. (b) Derived Δ of the smartphone images α_P(°) with respect to the original α_P(°) of the smartphone images. (c) Derived Δ of the smartphone images FUI with respect to the original FUI of the smartphone images. (d) Derived Δ of the smartphone images α_P(°) for the sample sites excluding Hulsbeek Lake (36 - 47) in order to derive a model to correct for the deviations of the smartphone images.

Another comparison was to match the water surface images with the FU scale develop by Wernand et al. (2013). This was by using the RGB values of the FU scale to generate images and their corresponding FUI and to visually compare these images to the smartphone images. The results were relatively good for the smartphone images except for the pit water surface image. From visual inspection, this water should correspond to FU 20 - 21 as can be visualised from the images in Table 8. Since the Citclops APP is based on relating the α_P(°) of the smartphone image to the α_N(°) of Novoa et al. (2013), FU 17 were obtained for the smartphone image and also FU 18 for RAMSES. However, the α_P(°) of the smartphone image and RAMSES on relating to the α_W(°) of Wernand et al. (2013) gave FU 21. From the preliminary results displayed by Citclops APP when an image is first captured and sent to the Citclops database which are indicated in Annex II, one could say the pit water contains extreme concentrations of humic acid which covers an FU range of 18 – 21. By this, the derived FUI of RAMSES and perhaps the smartphone image fall within the same range of water system. On the other hand, the “true” colour of the water translated to FUI would be missed if the relation is based on the $\alpha_P(°)$ of the smartphone image to the $\alpha_N(°)$ of Novoa et al. (2013). Thus, the Citclops APP would underestimate the "true" colour of water bodies if the Citclops APP model is based on comparing smartphone images $\alpha_P(°)$ with the $\alpha_N(°)$ of Novoa et al. (2013).

Table 8: Visual comparison of the pit water smartphone image $\alpha_P(°)$ and FUI to the $\alpha_W(°)$ and FUI generated using RGB values of Wernand et al. (2013) and the $\alpha_N(°)$ and FUI of laboratory FU solution transmission by Novoa et al. (2013). The FUI is calculated based on the $\alpha_P(°)$. For example, the $\alpha_P(°)$ of the smartphone image was 36.896°. Base on Novoa et al. (2013) this angle is < 39.769°. The smartphone image is this indexed 17. Also, Base on Wernand et al. (2013) this angle is < 39.674°. The point measured RAMSES data is this indexed 21.

Water Surface Image	RGB of FUI	Field Data $\alpha_P(°)$		Novoa et al. (2013)		Wernand et al. (2013)	
				FUI	$\alpha_N(°)$	FUI	$\alpha_W(°)$
	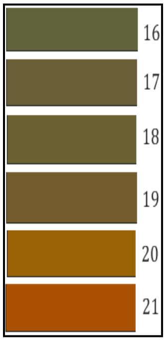	RAMSES	32.677	16	39.769	16	58.623
				17	34.906	17	54.649
				18	30.439	18	49.527
		Smartphone Image	36.896	19	26.337	19	43.963
				20	22.741	20	39.674
				21	<22.741	21	<39.674

7.3. Assessment of the Chromaticity Coordinates for Estimating Water Quality Variables

In terms of the Citclops APP, the only water quality variable estimated is the water colour which is translated into FUI. This water quality variable was previously assessed by comparing the results of the $\alpha_P(°)$ and FUI derived from RAMSES and the smartphone images from Section 7.2. The relation of the *xyz* chromaticity coordinates derived from RAMSES and the smartphone images gave a good correlation as was observed in Figure 34. From the perspective of HydroColor APP, the $R_{rs}(RGB)$ are comparable to the $R_{rs}(RGB)$ bands of traditional radiometers used generally for remote sensing of water quality. From Section 6.4 & 6.5, the assessment of the estimation of [SPM] and turbidity were successful through the red band reflectance from smartphone images using known remote sensing models used on radiometric measurements. The $R_{rs}(RGB)$ derived from the sRGB images of the grey card, sky and water surface this represents the “intrinsic colour” of the water sampled as a measure of reflectance. In the same contest, the *xyz* chromaticity coordinates obtained from the smartphone sRGB image of the water surface after gamma expansion, chromaticity adaptation, and illumination correction specified for natural water bodies would also represent the “intrinsic colour” of the water sampled in the CIE XYZ colour space. This, it is possible to quantify water quality variables from the *xyz* chromaticity coordinates since they used the same “spectra” as the $R_{rs}(RGB)$ of HydroColor APP and traditional remote sensing radiometers. The two colour space used by this APPs can also be transformed from one colour space to the other (that is, from RGB colour space to XYZ colour space and vice versa). The same relation as applied to the red band reflectance of HydroColor can thus be applied to the *x* chromaticity coordinate of Citclops to derive turbidity and [SPM].

As a pilot study, a relation between the *x* chromaticity coordinate and laboratory measured turbidity and [SPM] were first determined. The results indicated a good correlation between these two water quality variables and the *x* chromaticity coordinate after fitting a 2-degree polynomial as shown in Figure 38. The correlation of turbidity gave RMSE of 0.02 NTU and R^2 of 0.70 whiles the [SPM] gave RMSE of 0.02 gm^{-3} and R^2 of 0.79.

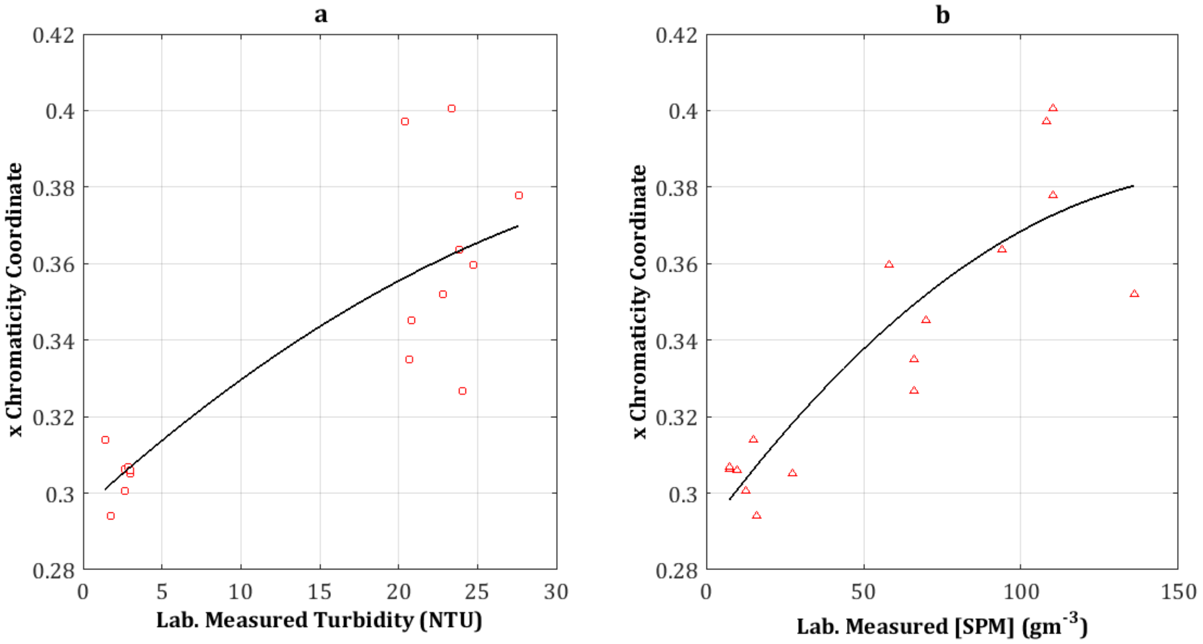

Figure 38: The relationship between laboratory measured turbidity and the [SPM], and the *x* chromaticity coordinate from the smartphone images. (a) Smartphone images *x* chromaticity coordinate versus laboratory measured turbidity (b) Smartphone images *x* chromaticity coordinate versus laboratory measured [SPM].

7.4. Estimating the [SPM] from the x Chromaticity Coordinate

Using the same models as applied on the red band reflectance of HydroColor APP in Section 6.4, estimates of the Nechad and logarithmic model coefficients were determined by using *x* chromaticity coordinate in estimating the [SPM]. The resulting models are as shown in Eq. (48 and 49) for the Nechad and logarithmic model respectively. The models validation of the [SPM] using the laboratory measurements gave an RMSE of 20.18 gm^{-3} and R^2 of 0.79 for the logarithmic model and RMSE of 2.93 gm^{-3} and R^2 of 0.77 for the Nechad model as indicated in Figure 39.

$$[SPM] = \frac{13.34 \times chrom(x)}{0.43 - chrom(x)} \tag{48}$$

$$[SPM] = 413.91 \times log(chrom(x)) + 508.99 \tag{49}$$

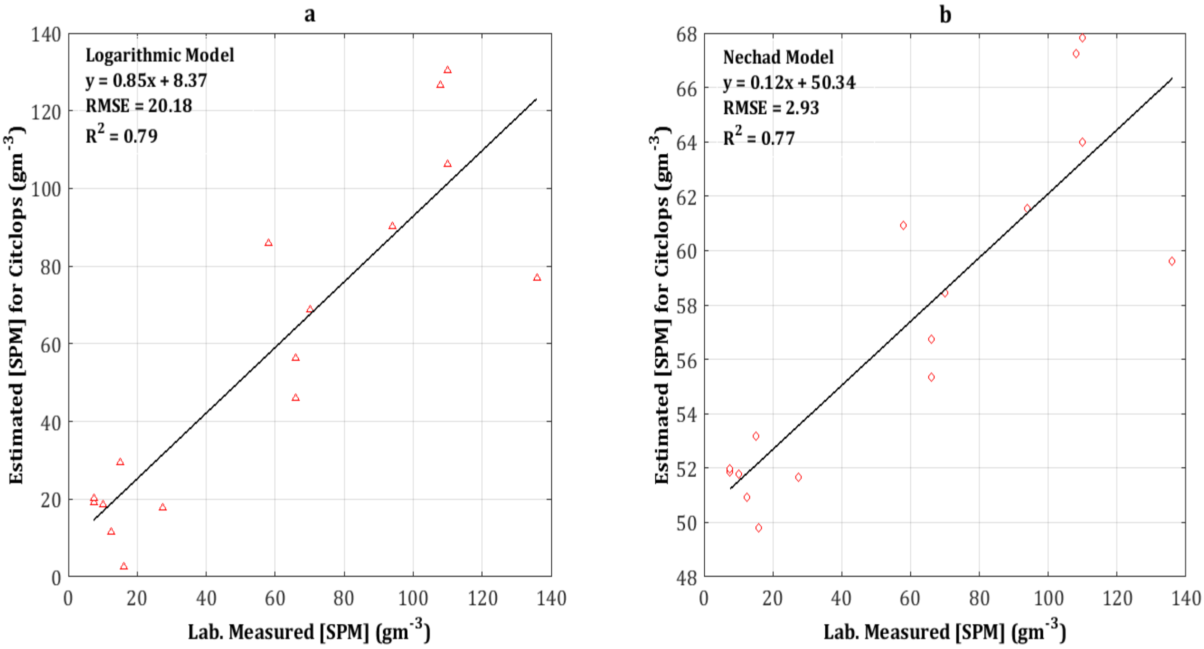

Figure 39: Validation of the proposed models for Citclops APP in estimating [SPM]. (a) Estimated [SPM] of the proposed semi-analytical model by Nechad et al. (2010) versus laboratory measured [SPM]. (b) Estimated [SPM] of the proposed logarithmic model versus laboratory measured [SPM].

7.4.1. Limitation of the Proposed [SPM] Models

The models limit in estimating the [SPM] using the *x* chromaticity coordinate were evaluated by varying the *x* chromaticity coordinate. For the Nechad model, the saturation of the *x* chromaticity coordinate occurred at 0.43 and [SPM] at half the saturation was 13.34 gm^{-3}. As shown in Figure 40.a, any *x* chromaticity coordinate above the saturation limit gave negative estimates of the [SPM]. In this regard, the Nechad model would not be effective in estimating [SPM] since turbid water systems as a result of SPM could exceed the model saturation limit. This, such a model cannot be used for estimation of the [SPM] in the case of using the x chromaticity coordinate.

For the logarithmic model, it was observed that the model was limited to x chromaticity coordinates ≥ 0.293. Figure 40.b this showed that *x* chromaticity coordinates values less than the limit gave negative estimates of [SPM]. The [SPM] estimate at the *x* chromaticity coordinate limit, 1 was approximately 509 gm^{-3}. Although the water systems that were used for this study varied, the least x chromaticity coordinate was greater than the limit of the logarithmic model. This model would, therefore, be appropriate for the estimation of [SPM].

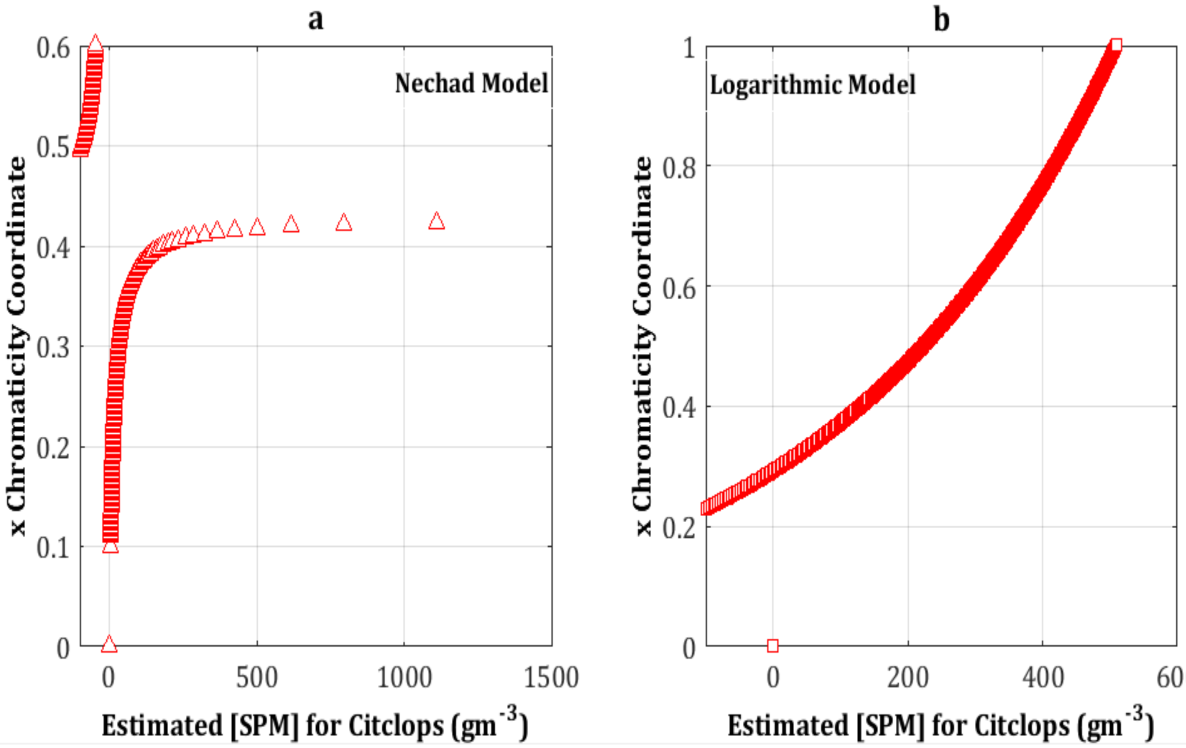

Figure 40: Simulation of the estimation of the [SPM] from the x chromaticity coordinate to determine the limitation of the proposed models for Citclops APP. (a) Semi-analytical model of Nechad et al. (2010) estimated [SPM] versus the x chromaticity coordinate. (b) The logarithmic model estimated [SPM] versus the x chromaticity coordinate.

7.5. Estimating Turbidity from the *x* Chromaticity Coordinate

Using the same models as applied on the red band reflectance of HydroColor APP in Section 6.5, estimates of the models' coefficients were determined for turbidity. The resulting models are as shown in Eq. (50 and 51) for the Nechad and logarithmic model respectively. The models validation of turbidity estimates with the laboratory measurements gave an RMSE of 5.86 NTU and R^2 of 0.73 for the logarithmic model and RMSE of 0.83 NTU and R^2 of 0.70 for the Nechad model as shown in Figure 41.

$$Turb = \frac{17.6 \times chrom(x)}{0.42 - chrom(x)} \tag{50}$$

$$Turb = 106.07 \times log(chrom(x)) + 130.29 \tag{51}$$

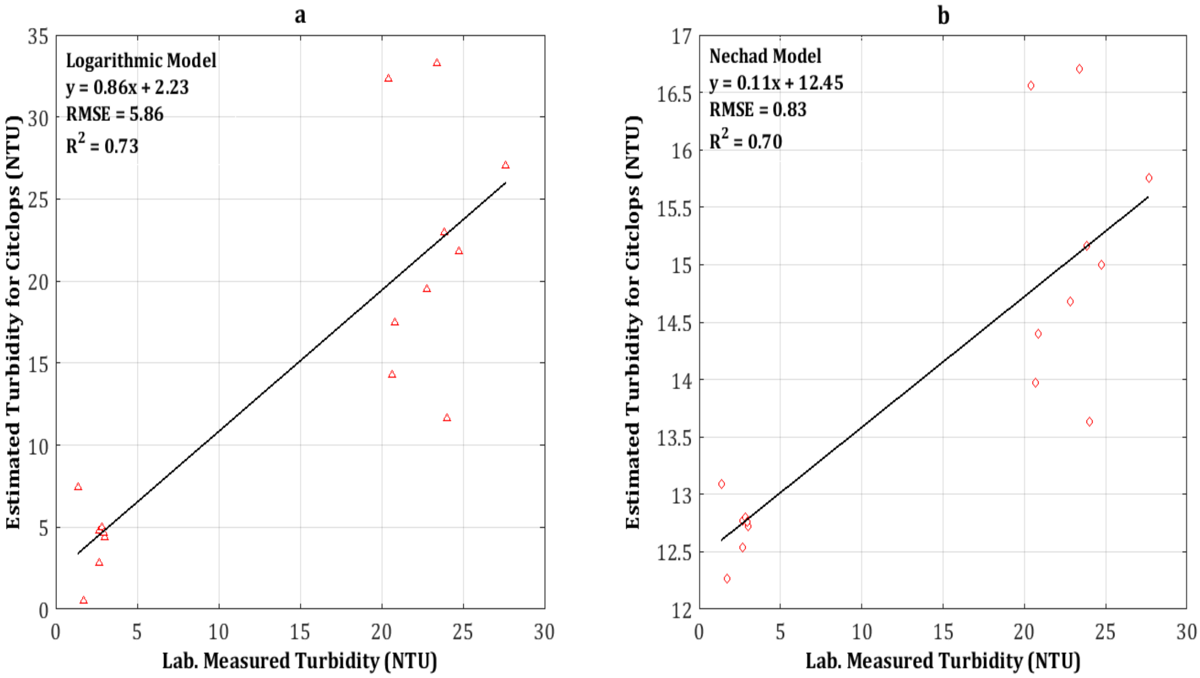

Figure 41: Validation of the proposed models for Citclops APP in estimating turbidity. (a) The estimated turbidity of the proposed semi-analytical model by Nechad et al. (2009) versus laboratory measured turbidity. (b) Estimated turbidity of the proposed logarithmic model versus laboratory measured turbidity.

7.5.1. Limitation of the Proposed Turbidity Models

The models on assessing their use in estimating turbidity gave the following results on turning the *x* chromaticity coordinate. For the Nechad model, the saturation of the *x* chromaticity coordinate occurred at 0.42 and turbidity at half the saturation was 17.6 NTU. From the results obtained as shown in Figure 42.a, any *x* chromaticity coordinate above the saturation limit gave a negative estimate of turbidity. In this regard, the Nechad model would not be effective in estimating turbidity since turbid water systems could exceed the model saturation limit. Thus, the Nechad model cannot be used for estimation of turbidity in the case of using the x chromaticity coordinate.

For the logarithmic model, it was observed that the model was limited to x chromaticity coordinates ≥ 0.293. This was approximately the same limit as the [SPM]. Figure 42.b this showed that x chromaticity coordinate values less than the limit gave negative estimates of turbidity. Turbidity estimate at the *x* chromaticity coordinate limit, 1 was approximately 130 NTU. For the varied water systems studied, the logarithmic model is thus recommended as the appropriate model for estimating turbidity from the *x* chromaticity coordinate. Generally, the estimates of turbidity were observed to be small due to the low values of turbidity that were used to calibrate the models.

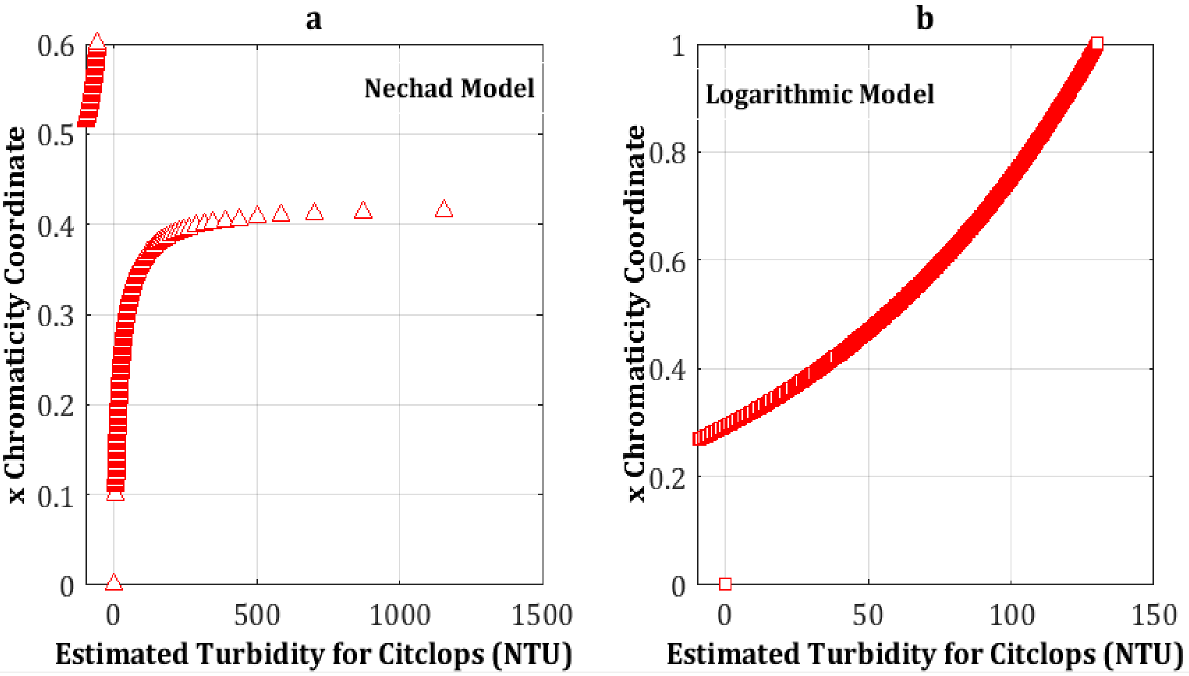

Figure 42: Simulation of the estimation of turbidity from the x chromaticity coordinate to determine the limitation of the proposed models for Citclops APP. (a) Semi-analytical model of Nechad et al. (2009) estimated turbidity versus the x chromaticity coordinate. (b) The logarithmic model estimated turbidity versus the x chromaticity coordinate.

7.6. Error Quantification of the Proposed Citclops APP Models

From the quantification of the models errors, it was observed that for the [SPM] the total error of the logarithmic model was 43.16 and the Nechad model was 42.89. The total error for turbidity was also observed to be 11.50 for the logarithmic model and 18.72 for the Nechad model. From the two models of the [SPM], the total error propagated for the logarithmic model was higher than the Nechad model. For the turbidity models, the logarithmic model had a lower total error as compared to the Nechad model. The errors in each models parameters of Eqs. (48, 49, 50 and 51) over their total error were determined as indicated in Figure 43. For the Nechad model in estimating [SPM], it was observed that the error in x chromaticity coordinate, $x\ chrom.coord.$ derived from the smartphone images contributed the most to the total error. The logarithmic model for [SPM] on the other hand was affected by the slope α_{CT2} followed by the $x\ chrom.coord.$ The error in estimating turbidity for the Nechad and logarithmic models were affected by the $x\ chrom.coord.$ Generally, the effects of the derived$x\ chrom.coord$ affects the estimation of the water quality variables studied. This could be due to the variation in the water systems studied.

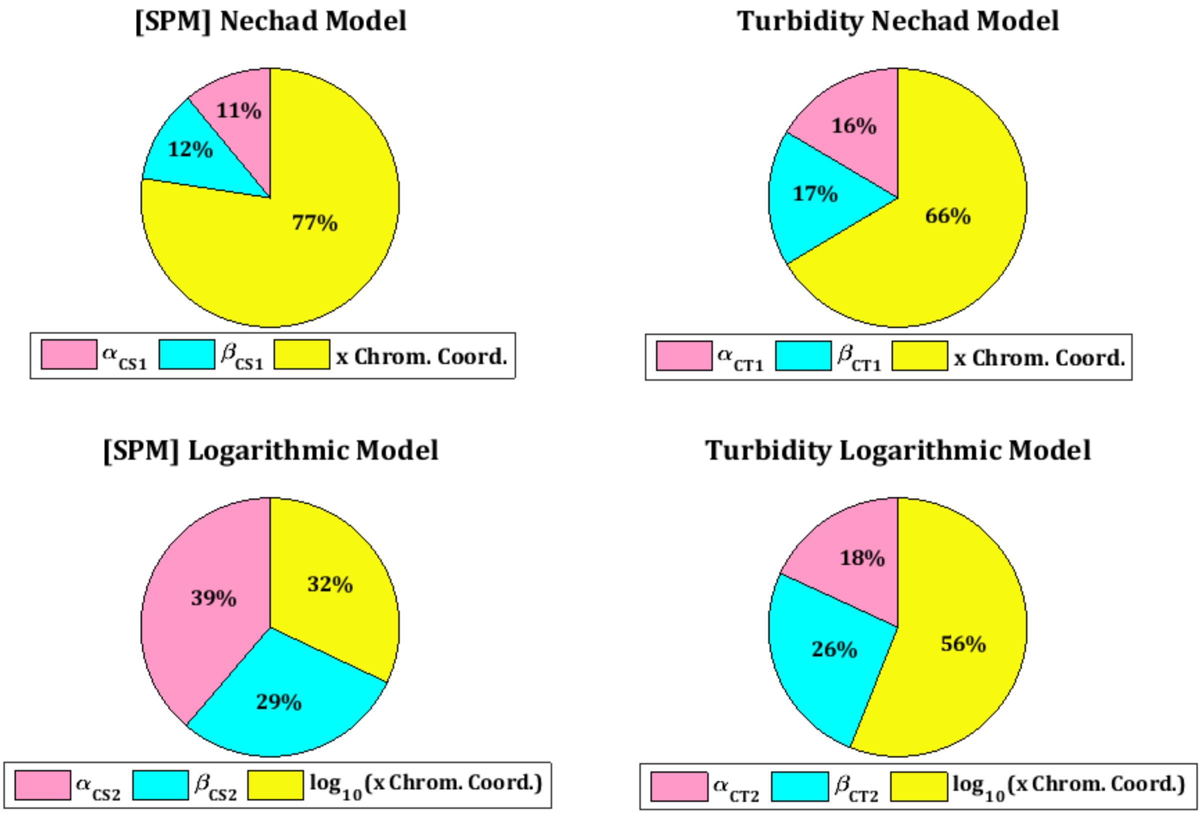

Figure 43: Pie charts of the relative contributions of the errors in the models parameters proposed for the Citclops APP shown as percentages % with respect to the total error of each model. The upper left panel indicates the errors in % of the Nechad model parameters in estimating [SPM]. The lower left panel indicates the errors in % of the logarithmic model parameters in estimating [SPM] The upper right panel indicates the error in % of the Nechad model parameters in estimating turbidity. The lower right panel indicates the error in % of the logarithmic model parameters in estimating turbidity.

7.7. Accuracy of Citclops APP Models

The accuracy of the proposed Nechad and logarithmic models in estimating turbidity and [SPM] were determined by their R^2 and MAE. The results are as shown in the bar charts of Figure 44. It was observed that the logarithmic model performed better for the estimation of [SPM] with $R^2 = 0.79$ and MAE = 14.77 gm^{-3}. For the turbidity models, the logarithmic model again performed better with $R^2 = 0.73$ and MAE = 4.14 NTU.

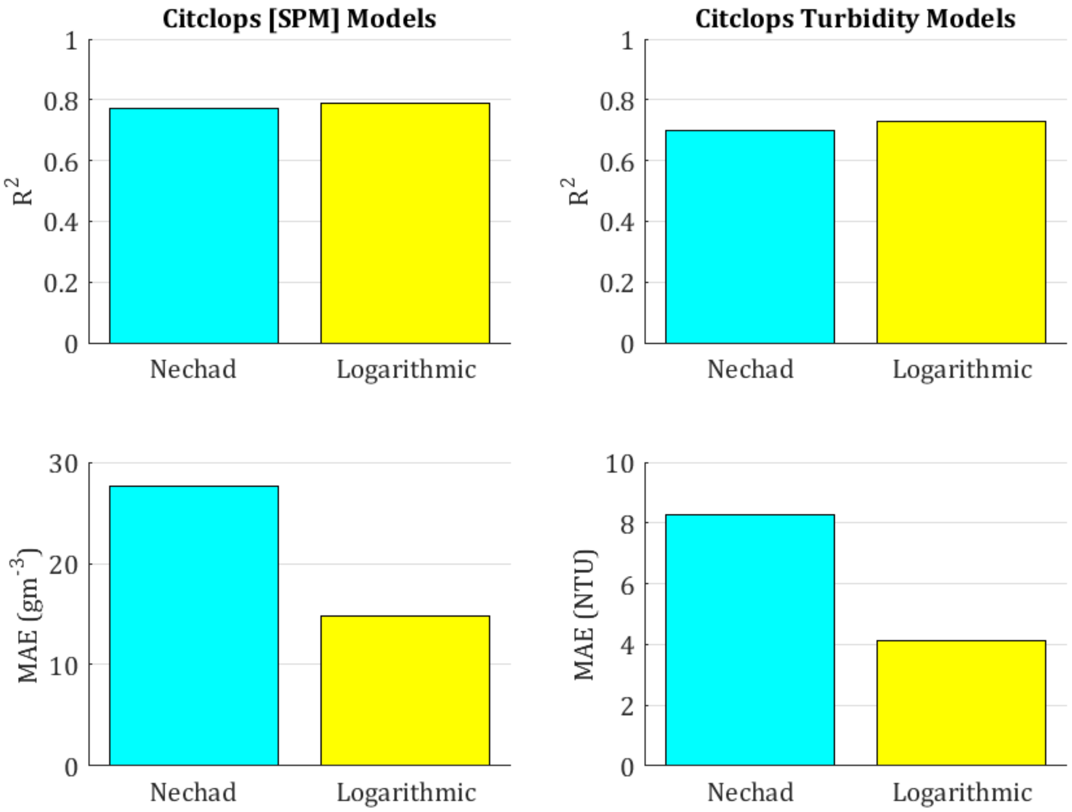

Figure 44: Bar charts of the accuracy of proposed Citclops APP models (Nechad and logarithmic) estimates of water quality variables compared to laboratory measurements. The upper left panel indicates the R^2 of the models for estimated [SPM] after validating with lab measured [SPM]. The lower left panel indicates the MAE of the models for estimated [SPM] after validating with lab measured [SPM]. The upper right panel indicates the R^2 of the models for estimated turbidity after validating with lab measured turbidity. The lower right panel indicates the MAE of the models for estimated turbidity after validating with lab measured turbidity.

7.8. Colour Saturation as a Measure of Water Transparency

The derived colour saturations described in Section 4.4.6 were intended to be used as a measure of the transparency of point measurements of the water bodies. This is because; the colour saturation of a water system determines how much optically active components are present to apparently affect the measure of the depth of light penetration into the water. Colour saturation as a quantitative measure of the saturation of a particular colour does not depend on the type of water constituent but on the constituents' capability to attenuate light. Colour saturation and dominant wavelength for each point measurement were thus obtained. An illustration of the results for a point measurement (P) is as shown in Figure 45.

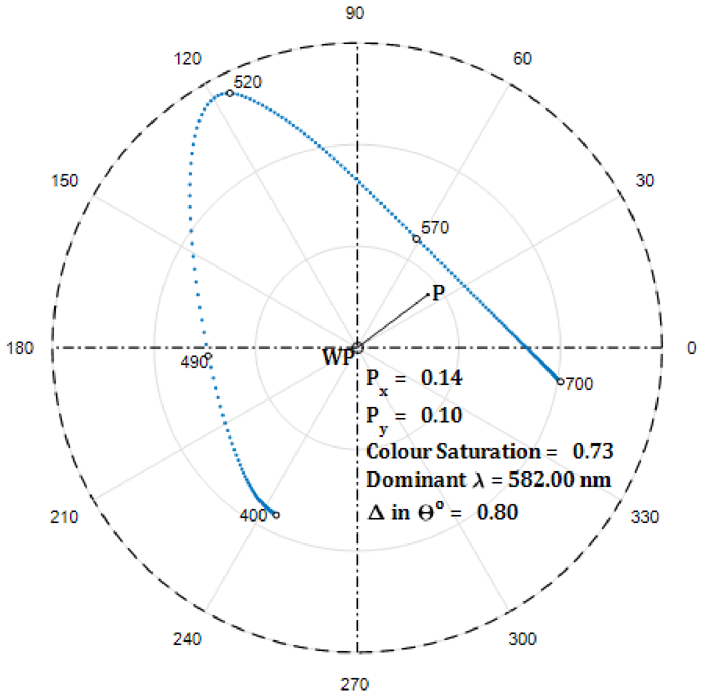

Figure 45: An illustration of derived colour saturation and dominant wavelength from the *xy* chromaticity coordinate on a polar coordinate system, and the deviation, Δ in estimating the difference in a point measured angle θ° and the angle of the corresponding CIE1931 chromaticity coordinate. This illustration is the result of the pit water sampled near Kristalbad artificial wetland.

For the whole study sites, the results of the colour saturation ranged from 0.08 to 0.73 as shown in Figure 46.a. This indicated that the point measured water bodies ranged from high transparent waters to low transparent waters. The more saturated the colour was, the closer the measurement was to the dominant wavelength. In terms of the dominant wavelength, the minimum wavelength was 497 and the maximum was 582 as shown in Figure 46.b. This being a wavelength range for cyan to the orange colour indicated the variation in the water types that were studied. The Δ in estimating the difference in a point measured angle and the angle of the corresponding CIE1931 chromaticity coordinate also ranged from 0.005° to 0.99° as indicated in Table 9. The Δ in estimating the angles were thus obtained to be lower than 1° out of 360° and thus can be said to be insignificant.

Since transparency measurements were not taken of the water bodies, no model was developed to relate these two parameters.

Table 9: Statistical summary of the colour saturation, dominant wavelength and the deviation, Δ in estimating the difference in a point measured angle θ° and the angle of the corresponding CIE1931 chromaticity coordinate. SD, standard deviation; CD, coefficient of variation.

Data	Minimum	Maximum	Median	Mean	SD	CV
Colour Saturation	0.08	0.73	0.29	0.35	0.23	0.66
Dominant Wavelength (nm)	497.0	582.0	562.0	550.2	25.32	0.05
Δ in θ°	0.005	0.99	0.41	0.45	0.27	0.60

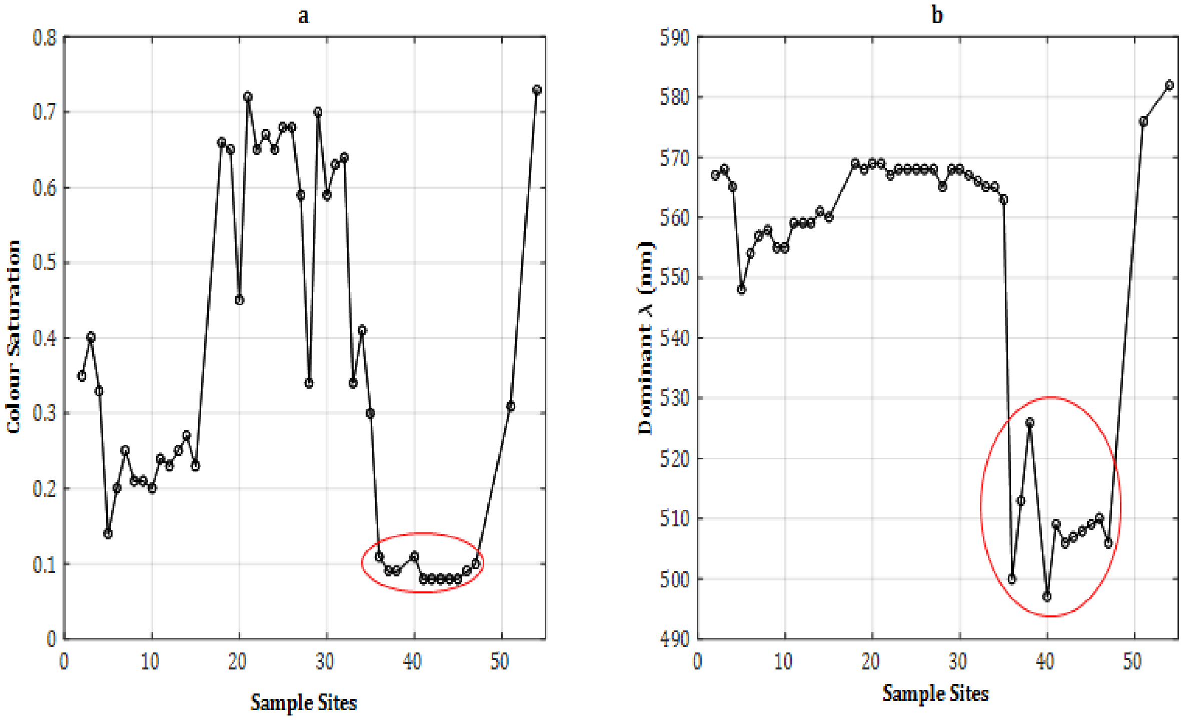

Figure 46: Variation of the colour saturation and dominant wavelength derived from the smartphone images with respect to the sample sites. (a) Colour saturation versus sample site. (b) Dominant wavelength versus sample site. From the Figure, Hulbeek Lake of site 36 – 47 (circled with red full line) gave lower colour saturation and dominant wavelengths within the blue wavelength range because of the clear nature of the water system.

8. CONCLUSION AND RECOMMENDATIONS

8.1. Conclusion

Smartphones although not empowered as water quality sensing devices can be used to obtain spectral information about our water quality through their enhanced capability to capture images and process using APPs. As was the focus of this study, the efficiency and accuracy in using the HydroColor and Citclops APPs in estimating water quality variables such as water colour translated to FUI, turbidity and [SPM] were successfully assessed. The results of their transfer functions (that is, the $R_{rs}(RGB)$ and the xyz chromaticity coordinates respectively of HydroColor and Citclops APP) derived from smartphone images on comparison with RAMSES cannot be conclusive. This is because, the $R_{rs}(RGB)$ of RAMSES data was not weighed with the spectral response function of the smartphone. This, the correlation of smartphone images and RAMSES $R_{rs}(RGB)$ were lower with $R^2 \leq 0.32$. The correlation of smartphone images and RAMSES xyz chromaticity coordinates on the other hand was good with $R^2 \geq 6.5$.

For the estimated water quality variables, even though it might not be representative of all water bodies, the models applied to derive turbidity and the [SPM] performed satisfactorily after comparison with laboratory measurements. The original models used by the HydroColor APP in estimating turbidity and [SPM] gave good results but had $R_{rs}(R)$ of 0.044 sr^{-1} as the reflectance saturation limit. The model used by HydroColor APP therefore would not be able to estimate turbid water systems such as CDOM and mineral dominated waters whose reflectances are greater than the saturation reflectance limit of the APP. The use of other models to improve the original model of HydroColor APP revealed some important results about the type of models to be used by the APP. The semi analytical model of Nechad et al. (2010) gave estimates of [SPM] until a reflectance saturation limit of 0.18 sr^{-1} and the estimate of [SPM] at half the saturation limit to be 1594.75 gm^{-3}. This would greatly improve on the APPs ability to sample a wider range of water systems. The logarithmic model for [SPM] and turbidity also indicates that the models were sensitive to very low reflectance values of water systems with turbidity < 0.09 NTU and [SPM] < 0.38 gm^{-3}. Thus, water systems with $R_{rs}(R) <$ 0.00134 sr^{-1} and 0.0015 sr^{-1} would therefore give no estimate of turbidity and [SPM] respectively. The error propagation of the models indicated the results of estimating both turbidity and [SPM] were greatly affected by the $R_{rs}(R)$ parameter up to 78 % of the total error. The accuracy of the models in estimating turbidity and [SPM] based on their R^2 and MAE also concluded that the proposed logarithmic model was the best compared to the original model used by the HydroColor APP and the proposed Nechad model.

For the Citclops APP, the resulting water colour of the smartphone images translated into FUI gave a good correlation with RAMSES with $R^2 = 0.70$. A model was successfully developed to correct for the offset in hue colour angles calculated within 36.896° and 99.991° to obtain an accurate estimate of FUI within this hue colour angles since the study was limited by data set. The *x* chromaticity coordinate of the smartphone images used to estimate turbidity and [SPM] gave good correlation with laboratory measurements. The Nechad model and the logarithmic model used in estimating turbidity and [SPM] both gave $R^2 \geq 0.70$. Parameterization of the Nechad model indicated that the model only estimated turbidity and [SPM] if the *x* chromaticity coordinate was > 0.42. The logarithmic model gave a limit to the *x* chromaticity coordinate to be > 0.29 for both turbidity and [SPM]. In other to sample all water systems, the logarithmic model was a better model to be used. It was observed that the error incurred in the estimation of turbidity and [SPM] were contributed mostly by the *x* chromaticity coordinate up to 77 % of the total error. The accuracy of the proposed models based on their R^2 and MAE showed that the logarithmic model performed better.

For the two APPs, it can be generally concluded that the use of the logarithmic model in estimating turbidity and [SPM] performed better than the Nechad model. The estimate of turbidity for the Citclops APP which is based on the XYZ colour space performed better with $R^2 = 0.73$ compared to $R^2 = 0.63$ of the HydroColor APP which uses the RGB colour space. On the other hand, the estimation of [SPM] for the HydroColor APP performed better with $R^2 = 0.90$ compared to $R^2 = 0.79$ of the Citclops APP. If the models used for this study are incorporated into the APPs, the Citclops APP is recommended for the estimation of water quality variables. This is because; the XYZ colour space used by this APP requires only the water surface image which would be easy and efficient to be used by ordinary citizen and researchers for water quality monitoring. Also, other water quality parameters such as water transparency can be estimated from the colour space of the Citclops APP. The XYZ colour space through the Citclops APP is therefore recommended for use for inland waters in the Netherlands.

8.2. Recommendations

At the end of this research work, the following are given as recommendations that require further studies:

- ⇒ Incorporate the proposed models into real measurements to assess their accuracy.
- ⇒ Model calibration and validation on a wider range of water systems should be further investigated to obtain models that can be applicable to all water systems.
- ⇒ With the sun being the primary source of daylight, changes in received sunlight due to the time of the day, weather conditions, geographical latitude, season, and sunspot cycle would significantly affect perceived water surface colour. This, the use of smartphones should be further studied under different lighting conditions to ascertained its effect on water surface colour.
- ⇒ Smartphones images format and their subsequent gamma correction requirements differ. This, a detailed study should be done on smartphone inter-comparison to determine the format of images, gamma correction and the models to be used in estimating water quality variables.
- ⇒ CDOM and mineral-dominated turbid water often have red colour water surfaces. Likewise, red tide events of algae bloom would also have red colour water surfaces. Images taken of these two different water bodies might give the same $R_{rs}(RGB)$ or xyz chromaticity coordinate base on the sRGB of the images. These images would therefore give the same estimate of water quality variables such as water colour of FU 21. Studies should be carried out to differentiate between the two cases of water systems in terms of smartphone images.
- ⇒ For inland water bodies, the presence of some inorganic and organic compounds have the ability to interact with light in many ways to produce colour (Nassau, 2001). Some inorganic compounds (pigments) turn to be weather resistant with the ability to hide light energy thereby producing dull colours as compared to organic compounds. Sophisticated procedure should, therefore, be applied to

assess the effects of such materials on the colour of water systems and its impact on smartphone images results.

⇒ Derive chlorophyll and CDOM using the band ratio models as specified by Goddijn & White (2006) and Goddijn et al. (2009) for the two APPs. For chlorophyll, the red band reflectance should be subtracted from the green and blue band reflectance in the band ratio to remove the impact of scattering of mineral particles in Case 2 water as specified by Leeuw (2014).

⇒ Comparison of smartphone images with high-resolution multispectral sensors.

⇒ Scale down of multispectral sensor images using smartphone images through Bayesian inference and other methods.

⇒ The use of smartphone images and multispectral sensors to identify areas of submerged aquatic vegetation of water bodies.

⇒ Develop a graphical user interface (GUI) in open source software such as ILWIS (Integrated Land and Water Information System) for water colour monitoring translated into FUI. This should include documentation of a user guide manual for the GUI.

LIST OF REFERENCES

Abbenhues, C. (2003). *Facts and figures on tourism and recreation in Overijssel*. Zwolle, The Netherlands.

Aitken, M., & Gauntlett, C. (2013). *Patient Apps for Improved Healthcare: From Novelty to Mainstream*. Parsippany, USA.

Akenine-Möller, T., Haines, E., & Hoffman, N. (2008). *Real-Time Rendering* (3rd ed.). Natick, Massachusetts: A K Peters/CRC Press.

Ambarwulan, W., Verhoef, W., Mannaerts, C. M., & Salama, M. S. (2012). Estimating total suspended matter concentration in tropical coastal waters of the Berau estuary , Indonesia. *International Journal of Remote Sensing*, *33*(16), 4919–4936. doi:10.1080/01431161.2011.583289

Aminot, A., & Rey, F. (2000). *Standard procedure for the determination of chlorophyll a by spectroscopic methods. ICES Techniques in Marine Environmental Sciences*. Plouzane, France. Retrieved from http://www.ices.dk/ocean/procedures/timeschl.pdf

Arnell, N. W. (1999). Climate change and global water resources. *Global Environmental Change*, *9*, 31–49. doi:10.1016/S0959-3780(99)00017-5

Banna, M. H., Imran, S., Francisque, A., Najjaran, H., Sadiq, R., Rodriguez, M., & Hoorfar, M. (2014). Online Drinking Water Quality Monitoring: Review on Available and Emerging Technologies. *Critical Reviews in Environmental Science and Technology*, *44*(12), 1370–1421. doi:10.1080/10643389.2013.781936

Bethea, N. B. (2011). *The Water Cycle (Science Foundations)* (3rd ed.). Lewiston, New York, U.S.A.: Chelsea House Publications.

Bevington, R. P., & Robinson, K. D. (2003). *Data Reduction and Error Analysis for the Physical Sciences* (3rd ed.). New York, USA: McGraw-Hill.

Binding, C. E., Bowers, D. G., & Mitchelsson-Jacob, E. G. (2005). Estimating suspended sediment concentrations from ocean colour measurements in moderately turbid waters; the impact of variable particle scattering properties. *Remote Sensing of Environment*, *94*, 373–383. doi:10.1016/j.rse.2004.11.002

Boss, E., Taylor, L., Gilbert, S., Gundersen, K., Hawley, N., Janzen, C., … Tamburri, M. N. (2009). Comparison of inherent optical properties as a surrogate for particulate matter concentration in coastal waters. *Limnology and Oceanography: Methods*, (Methods 7), 803–810.

Business Communications Company. (2014). *Environmental Sensing and Monitoring Technologies: Global Markets. BCC Research Instruction & Sensors Report*. Wellesley, Massachusetts, USA. Retrieved from http://www.bccresearch.com

Centre for Affordable Water and Sanitation Technology. (2008). Project Implementation for the Biosand Filter Workshop. In *Participant Manual* (p. 97). Calgary, Alberta, Canada: CAWST. Retrieved from www.cawst.org

Chang, G. C., & Gould, R. W. J. (2006). Comparisons of optical properties of the coastal ocean derived from satellite ocean color and in situ measurements. *Applied Optics*, *14*(22), 15.

Chapman, D. V. (2002). *Water Quality Assessments : A guide to the use of biota, sediments and water in environmental monitoring* (2nd ed.). London: CRC Press.

Commission Internationale d'Eclairage. (2004). *CIE Technical Report: Colorimetry* (3rd ed.). (E. C. . Carter, Y. . Ohno, M. R. . Pointer, A. R. . Robertson, R. . Sève, J. D. . Schanda, & K. . Witt, Eds.). Vienna, Austria: CIE.

Corke, P., Wark, T., Jurdak, R., Hu, W., Valencia, P., & Moore, D. (2010). Environmental Wireless Sensor Networks. *Proceedings of the IEEE*, *98*(11), 1903–1917. doi:10.1109/JPROC.2010.2068530

Cotton, S. D. (1995). *Colour , colour spaces and the human visual system*. Birmingham, England: B15-2TT.

Dierssen, H. M., Kudela, R. M., Ryan, J. P., & Zimmerman, R. C. (2006). Red and black tides: Quantitative analysis of water-leaving radiance and perceived color for phytoplankton, colored dissolved organic matter, and suspended sediments. *Limnology and Oceanography*, *51*(6), 2646–2659.

Dogliotti, A. I., Ruddick, K. G., Nechad, B., Doxaran, D., & Knaeps, E. (2015). A single algorithm to retrieve turbidity from remotely-sensed data in all coastal and estuarine waters. *Remote Sensing of Environment*, *156*, 157–168. doi:10.1016/j.rse.2014.09.020

Dore, M. H. I. (2005). Climate change and changes in global precipitation patterns: What do we know? *Environment International*, *31*(8), 1167–1181. doi:10.1016/j.envint.2005.03.004

Ericsson. (2014). *Ericsson Mobility Report*. Stockholm, Sweden. Retrieved from http://www.ericsson.com/res/docs/2014/ericsson-mobility-report-june-2014.pdf

Ericsson. (2015). *Ericsson Mobility Report*. Stockholm, Sweden. Retrieved from http://www.ericsson.com/res/docs/2015/ericsson-mobility-report-june-2015.pdf

Garaba, S. P., & Zielinski, O. (2013). Methods in reducing surface reflected glint for shipborne above-water remote sensing. *Journal of the European Optical Society - Rapid Publications*, *8*(13058). Retrieved from http://dx.doi.org/10.2971/jeos.2013.13058

Gert, S. (1996). *Hermann Günther Grassmann (1809-1877): Visionary Mathematician, Scientist and Neohumanist Scholar* (Vol. 187). Dordrecht, The Netherlands: Springer Science & Business Media. doi:10.1007/978-94-015-8753-2

Goddijn, L. M., & White, M. (2006). Using a digital camera for water quality measurements in Galway Bay. *Estuarine, Coastal and Shelf Science*, *66*, 429–436. doi:10.1016/j.ecss.2005.10.002

Goddijn-Murphy, L., Dailloux, D., White, M., & Bowers, D. (2009). Fundamentals of in Situ Digital Camera Methodology for Water Quality Monitoring of Coast and Ocean. *Sensors*, (9), 5825–5843. doi:10.3390/s90705825

Gordon, H. R., Brown, J. W., Brown, O. B., Evans, R. H., Smith, R. C., Baker, K. S., & Clark, D. K. (1988). A semianalytic radiance model of ocean color. *Journal of Geophysical Research*, *93*(D9), 10,909–10,924.

Haan, C. T., Storm, D. E., Al-Issa, T., Prabhu, S., Sabbagh, G. J., & Edwards, D. R. (1998). Effect of parameter distributions on uncertainty analysis of hydrologic models. *Transactions of the ASAE*, *41*(1), 65–70. doi:10.13031/2013.17158

Haas, H. A., & Tosserams, M. (2001). *Balancing between sweet and salty: Space for resilience and security in the Delta*. Middelburg, The Netherlands: Rijkswaterstaat, RIKZ.

Hach Company. (2008). *Portable Turbidimeter Model 2100P: Instrument and Procedure Manual*. Dusseldorf, Germany: Hach Company.

Haklay, M. (2013). Citizen Science and Volunteered Geographic Information: Overview and Typology of Participation. In D. Sui, S. Elwood, & M. Goodchild (Eds.), *Crowdsourcing Geographic Knowledge* (pp. 105–122). Dordrecht, The Netherlands: Springer Science & Business Media. doi:10.1007/978-94-007-4587-2_7

Hatcher, A., Hill, P., & Grant, J. (2001). Optical backscatter of marine flocs. *Journal of Sea Research*, *46*, 1–12.

In-Situ Inc. (2013). SMARTROLL™ Multiparameter Handheld Specifications. Retrieved August 4, 2015, from https://in-situ.com/wp-content/uploads/2014/11/smarTROLL-Multiparameter-Handheld-and-iSitu-Smartphone-App_Specs.pdf

International Telecommunication Union. (2014). *The World in 2014 - ICT Facts and Figures*. Geneva, Switzerland.

IOCCG. (2006). *Remote Sensing of Inherent Optical Properties : Fundamentals , Tests of Algorithms , and Applications* (No. 5). (Z. Lee, Ed.)*Reports of the International Ocean-Colour Coordinating Group*. Dartmouth, Canada: IOCCG.

Kallio, K., Kutser, T., Hannonen, T., Koponen, S., Pulliainen, J., Pyhalahti, T., & Vepsalainen, J. (2001). Retrieval of water quality from airborne imaging spectrometry of various lake types in different seasons. *The Science of the Total Environment*, *268*, 59–77.

Kang, H. R. (1996). *Color Technology for Electronic Imaging Devices*. Bellingham, Washington, U.S.A.: SPIE Optical Engineering Press.

Katoh, N., & Nakabayashi, K. (2001). Applying Mixed Adaptation to Various Chromatic Adaptation Transformation (CAT) Models. In *PICS 2001: Image Processing, Image Quality, Image Capture Systems Conference* (Vol. 4, pp. 299–305). Montreal (Quebee), Canada.

Keith, P. B. T., Lane, K. R., & Csallny, C. S. (1975). Remote Sensing and Water Resources Management. *Desalination*, *17*, 141–143.

Kim, S., & Paulos, E. (2010). inAir: Sharing Indoor Air Quality Measurements and Visualizations. In *Proceedings of ACM CHI 2010 Conference on Human Factors in Computing Systems* (pp. 1861–1870). Atlanta, Georgia, U.S.A. Retrieved from http://doi.acm.org/10.1145/1753326.1753605

Kim, S., Robson, C., Zimmerman, T., Pierce, J., & Haber, E. M. (2011). Creek Watch: Pairing Usefulness and Usability for Successful Citizen Science. In *Proceedings of ACM CHI 2011 Conference on Human Factors in Computing Systems* (pp. 2125–2134). Vancouver, BC, Canada. Retrieved from http://dx.doi.org/10.1145/1978942.1979251

Klein, G. A. (2010). Light Sources, Types of Colorants, Observer. In *Industrial Color Physics* (pp. 11–131). New York: Springer.

Kokhanovsky, A. A. (2013). *Light Scattering Reviews 8: Radiative transfer and light scattering*. Verlag, Berlin, Germany: Springer Berlin Heidelberg.

Kotovirta, V., Toivanen, T., Järvinen, M., Lindholm, M., & Kallio, K. (2014). Participatory surface algal bloom monitoring in Finland in 2011 – 2013. *Environmental Systems Research*, *3*(24), 11. doi:10.1186/s40068-014-0024-8

Ku, H. H. (1966). Notes on the Use of Propagation of Error Formulas. *Journal of Research of the National Bureau of Standards*, *70C*(4), 263–273. doi:10.6028/jres.070c.025

Lee, Z., Carder, K. L., & Arnone, R. A. (2002). Deriving inherent optical properties from water color: a multiband quasi-analytical algorithm for optically deep waters. *Applied Optics*, *41*(27), 5755–5772. doi:10.1364/AO.41.005755

Lee, Z., Pahlevan, N., Ahn, Y.-H., Greb, S., & O'Donnell, D. (2013). Robust approach to directly measuring water-leaving radiance in the field. *Applied Optics*, *52*(8), 1693–1701. doi:10.1364/AO.52.001693

Leeuw, T. (2014). *Crowdsourcing Water Quality Data Using the iPhone Camera*. University of Maine. Electronic Theses and Dissertations. Paper 2118. Retrieved from http://digitalcommons.library.umaine.edu/cgi/viewcontent.cgi?article=3155&context=etd

Lim, S.-H. (2015). Experimental Comparison of Hybrid and Native Applications for Mobile Systems. *International Journal of Multimedia and Ubiquitous Engineering*, *10*(3), 1–12. doi:10.14257/ijmue.2015.10.3.01

Maisonneuve, N., Stevens, M., & Ochab, B. (2010). Participatory noise pollution monitoring using mobile phones. *International Journal of Government & Democracy in the Information Age*, *15*, 51–71. doi:10.3233/IP-2010-0200

Maritorena, S., Siegel, D. A., & Peterson, A. R. (2002). Optimization of a semianalytical ocean color model for global-scale applications. *Applied Optics*, *41*(15), 2705–2714. doi:10.1364/AO.41.002705

McGrath, M. J., & Scanaill, C. N. (2014). *Sensor Technologies: Healthcare, Wellness and Environmental Appli cations*. New York: Apress Media, LLC.

Mobley, C. D. (1999). Estimation of the remote-sensing reflectance from above-surface measurements. *Applied Optics*, *38*(36), 7442–7455. doi:10.1364/AO.38.007442

Myint, S. W., & Walker, N. D. (2002). Quantification of surface suspended sediments along a river dominated coast with NOAA AVHRR and SeaWiFS measurements: Louisiana, USA. *International Journal of Remote Sensing*, *23*(16), 3229–3249. doi:10.1080/01431160110104700

Nassau, K. (2001). *The Physics and Chemistry of Color: The Fifteen Causes of Color* (2nd ed.). New York ; Chichester : Wiley.

Nechad, B., Ruddick, K. G., & Neukermans, G. (2009). Calibration and validation of a generic multisensor algorithm for mapping of turbidity in coastal waters. *Remote Sensing of the Ocean*, *7473*. doi:10.1117/12.830700

Nechad, B., Ruddick, K. G., & Park, Y. (2010). Remote Sensing of Environment Calibration and validation of a generic multisensor algorithm for mapping of total suspended matter in turbid waters. *Remote Sensing of Environment*, *114*(4), 854–866. doi:10.1016/j.rse.2009.11.022

Neukermans, G., Loisel, H., Me, X., Astoreca, R., & Mckee, D. (2012). In situ variability of mass-specific beam attenuation and backscattering of marine particles with respect to particle size , density , and composition. *Limnology and Oceanography*, *57*(1), 124–144. doi:10.4319/lo.2011.57.1.0124

Novo, E. M. M., Paulo, S., Hansom, J. D., Rran, P. J. C. U., & Bank, W. (1989). The effect of viewing geometry and wavelength on the relationship between reflectance and suspended sediment concentration. *International Journal of Remote Sensing*, *10*(8), 1357–1372. doi:10.1080/01431168908903973

Novoa, S., van der Woerd, H. J., & Wernand, M. (2015). WACODI : A generic algorithm to derive the intrinsic color of natural waters from digital images. *Limnology and Oceanography: Methods*, *13*(2), 697–711. doi:10.1002/lom3.10059

Novoa, S., Wernand, M. R., & van der Woerd, H. J. (2013). The Forel-Ule scale revisited spectrally: Preparation protocol, transmission measurements and chromaticity. *Journal of the European Optical Society - Rapid Publications*, *8*(13057). doi:10.2971/jeos.2013.13057

Novoa, S., Wernand, M. R., & van der Woerd, H. J. (2014). The Forel-Ule scale converted to modern tools for participatory water quality monitoring. In *Ocean Optics Conference XII* (p. 6). Portland, Maine, USA. doi:10.13140/2.1.4179.4246

Novoa, S., Wernand, M. R., & van der Woerd, H. J. (2014). The modern Forel-Ule scale: A "do-it-yourself" colour comparator for water monitoring. *Journal of the European Optical Society - Rapid Publications*, *9*(14025). doi:10.2971/jeos.2014.14025

O'Reilly, J. E., Maritorena, S., Mitchell, B. G., Siegel, D. a., Carder, K. L., Garver, S. a., … McClain, C. (1998). Ocean color chlorophyll algorithms for SeaWiFS. *Journal of Geophysical Research*, *103*(C11), 24937–24953. doi:10.1029/98JC02160

Ouyang, Y., Nkedi-Kizza, P., Wu, Q. T., Shinde, D., & Huang, C. H. (2006). Assessment of seasonal variations in surface water quality. *Water Research*, *40*, 3800–3810. doi:10.1016/j.watres.2006.08.030

Pascale, D. (2003). *A Review of RGB Color Spaces*. Montreal (Quebee), Canada. Retrieved from www.babelcolor.com

Qihao, W. (2011). *Advances in Environmental Remote Sensing Sonsors: Algorithms, and Applications*. *International Journal of Applied Earth Observation and Geoinformation* (Vol. 13). London: CRC Press, Taylor & Frances. doi:10.1016/j.jag.2011.05.015

Reinhard, E., Heidrich, W., Debevec, P., Pattanaik, S., Ward, G., & Myszkowski, K. (2014). *High Dynamic Range Imaging: Acquisition, Display, and Image-Based Lighting*. Elsevier Science.

Ruddick, K. G., De Cauwer, V., Park, Y.-J., & Moore, G. F. (2006). Seaborne measurements of near infrared water-leaving reflectance: The similarity spectrum for turbid waters. *Limnology and Oceanography*, *51*(2), 1167–1179. doi:10.4319/lo.2006.51.2.1167

Salama, M. S., Su, Z., Mannaerts, C. M., Verhoef, W., & Dekker, A. (2009). Deriving inherent optical properties and associated inversion-uncertainties in the Dutch Lakes. *Hydrology and Earth System Sciences*, *6*(2), 2075–2098. doi:10.5194/hessd-6-2075-2009

Salama, M. S., van der Velde, R., van der Woerd, H. J., Kromkamp, J. C., Philippart, C. J. M., Joseph, a. T., … Su, Z. (2012). Technical Note: Calibration and validation of geophysical observation models. *Biogeosciences*, *9*, 2195–2201. doi:10.5194/bg-9-2195-2012

Sicard, C., Glen, C., Aubie, B., Wallace, D., Jahanshahi-Anbuhi, S., Pennings, K., … Filipe, C. D. M. (2015). Tools for water quality monitoring and mapping using paper-based sensors and cell phones. *Water Research*, *70*, 360–369. doi:10.1016/j.watres.2014.12.005

Stramski, D., Boss, E., Bogucki, D., & Voss, K. J. (2004). The role of seawater constituents in light backscattering in the ocean. *Progress in Oceanography*, *61*, 27–56. doi:10.1016/j.pocean.2004.07.001

Su, Z., Roebeling, R. A., Schulz, J., Holleman, I., Levizzani, V., Timmermans, W. J., … Wang, L. (2011). Observation of Hydrological Processes Using Remote Sensing. In P. Wilderer (Ed.), *Treatise on Water Science* (pp. 351–399). Oxford: Academic Press.

Tilstone, G. H., Moore, G. F., Sorensen, K., Doerffer, R., Røttgers, R., Ruddick, K. G., … Jørgensen, P. V. (2003). Regional Validation of MERIS Chlorophyll products in North Sea coastal waters. In *Working meeting on MERIS and AATSR Calibration and Geophysical Validation (ENVISAT MAVT-2003)* (pp. 1–78). Frascati.

Tkalcic, M., & Tasic, J. F. (2003). *Colour spaces - perceptual, historical and applicational background* (Vol. 1). Slovenia.

Tosserams, M., Backx, J., van der Melj, V., Dijkers, C., & Slager, H. (2001). *Exploring the Delta*.

United Nations. (2002). *United Nations World Summit on Sustainable Development*. Johannesburg, South Africa.

van der Woerd, H. J., & Wernand, M. R. (2015). True Colour Classification of Natural Waters with Medium-Spectral Resolution Satellites: SeaWiFS, MODIS, MERIS and OLCI. *Sensors*, *15*, 25663–25680. doi:10.3390/s151025663

Verma, S. (2009). Seasonal Variation of Water Quality in Betwa River at Bundelkhand Region, India. *Global Journal of Environmental Research*, *3*(3), 164–168.

von Kris, J. (1970). Influence of adaptation on the effects produced by luminous stimuli. In D. L. . MacAdam (Ed.), *Sources of Color Science* (pp. 120–126). Cambridge, MA: MIT Press.

Wernand, M. R., Hommersom, A., & van der Woerd, H. J. (2013). MERIS-based ocean colour classification with the discrete Forel – Ule scale. *Ocean Science*, *9*, 477–487. doi:10.5194/os-9-477-2013

Withagen, L. (2000). *DELTA 2000: Inventory of current situation Delta Waters*. Zealand, The Netherlands.

World Economic Forum. (2014). *The Global Information Technology Report 2014: Rewards and Risks of Big Data*. (B. Bilbao-Osrio, S. Dutta, & B. Lanvin, Eds.)*Insight Report*. Geneva, Switzerland.

Wyszecki, G. (2006). *Color*. Chicago: World Book Incoperation.

ANNEX I – LINKS TO THE APPS USED

Links to more information on the APPs used are; Citclops APP http://www.citclops.eu now called EyeOnWater http://www.eyeonwater.org and HydroColor APP http://misclab.umeoce.maine.edu/research/HydroColor.php. A general overview of these smartphone APPs for monitoring water quality is discussed below.

ANNEX II - CITCLOPS APP USAGE

The Citclops APP includes a digitalized Forel-Ule (FU) color-comparator scale that mimics the colour scale of the traditional FU colour scale or Xantho-meter which has been used by oceanographers and limnologists since the 19th century to measure the colour of natural water bodies. Examples of the colours of water bodies taken from some parts of the globe are as shown in below.

Colours of water bodies taken from some parts of the globe; Source: http://forel-ule-scale.com

The traditional FU scale includes 21 chemically prepared colours placed in glass vials. These colours range from indigo-blue (index 1) thru green (index 10) to cola-brown (index 21) as shown in a Modern FU scale of the Figure below. The final vial (index 22) added to Modern FU scales is distilled water (which is colourless). Recently, Novoa, et al. (2014) developed the FU scale using high-quality lighting filters and a white frame as shown in the Figure below to improve upon the materials originally used in the manufacture of the scale and to reduce the risk in handling it (chemical solutions placed in glass vials).

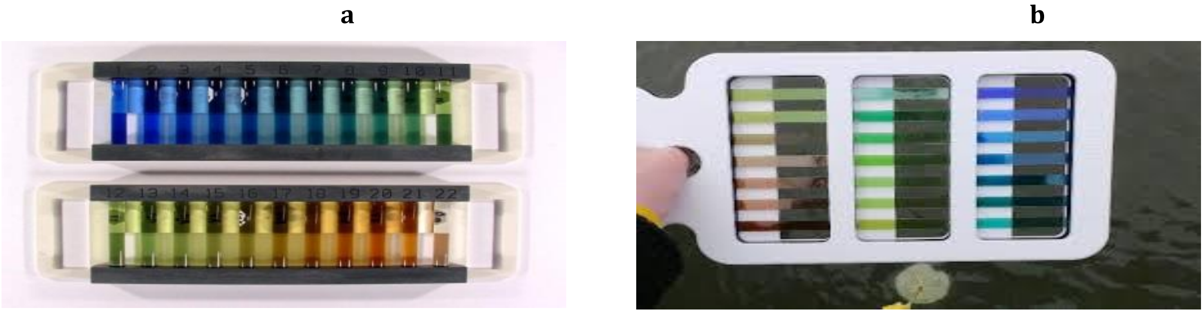

Modern FU scales of different materials; (a) glass vials containing chemically prepared solutions, and (b) high-quality lighting filters on a white frame. These images were acquired from the Citclops website: http://www.citclops.eu

Using the back camera of a smartphone to view a water body, the part of the picture that best represents the colour of the water (without foam or sun reflection) is captured. The image of the water is taken at an angle ≤ 40° from the horizontal surface of the water. This is achieved by adhering to the compass display on the image capture screen. For a better view of the water colour, the user in possession of a Secchi disc is asked to place it at half the Secchi disc depth (SDD) to boost the light signal coming from the water. The use of the Secchi disc is especially important on cloudy and dark days when not enough light is coming from the water column. The APP also includes an option where the user can indicate the measure of transparency at half the SDD. Thus, in the case of using a Secchi disc, the area where the Secchi disc (at ½ SDD) can appear in the image is preferred. An area of the image which best represents the colour of the water is then cropped for analysis.

The cropped water surface image is then simultaneously viewed with the digitalized FU scale of 21 colour bars. Each colour bar has 3 colour saturations to mimic the water transparency. The best matching colour bar of the digitalized FU scale is then selected as the corresponding colour of the water image. As a measure of accuracy, measurements from a Modern FU scale can be used to validate the digitalised FU output from the APP.

The standard RGB, sRGB of the digital image is then used to calculate the FUI using specific models after the image is submitted to the Citclops community as specified via the APP. The results of the FUI can then be obtained from the Citclops database via their website for a user of the Citclops APP.

However, preliminary results displayed by the APP are as follows based on their corresponding colour indexes listed below. The corresponding category of water that was sampled is thus highlighted to make it clear to the observer the water type that was sampled. This information was taken directly from the site of the Citclops APP http://www.citclops.eu which is the same information displayed categorically by the APP.

1. Indigo blue to greenish blue with high light penetration (1-5 FU scale). These waters have often low nutrient levels and low production of biomass. The colour is dominated by microscopic algae (phytoplankton).

2. Greenish blue to bluish green (6-9 FU scale). The colour is still dominated by algae, but also increased dissolved matter and some sediment may be present. Typical for areas towards the open sea.

3. Greenish (10-13 FU scale). Often coastal waters which usually display increased nutrient and phytoplankton levels, but also contain minerals and dissolved organic material.

4. Greenish brown to brownish green (14-17 FU scale). Usually with high nutrient and phytoplankton concentrations, but also increased sediment and dissolved organic matter. Typical for near-shore areas and tidal flats.

5. Brownish green to cola brown (18-21 FU scale). Waters with an extremely high concentration of humic acids, which are typical for rivers and estuaries.

To make the results more presentable, an illustrative water colour with their FUI is as show in the Figure below.

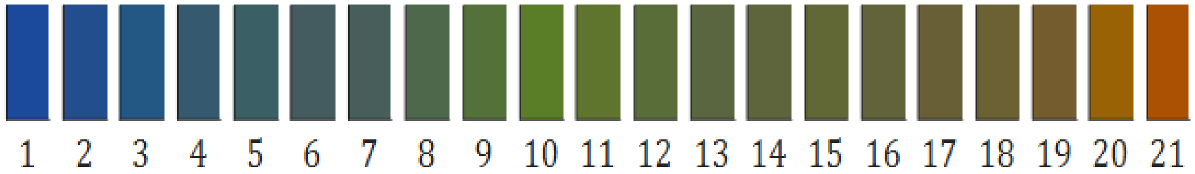

Developed RGB images of water colour with their FUIs. This was developed based on the RGB colour values for the reproduction of the *FU* legend by Wernand et al. (2013).

ANNEX III - HYDROCOLOR APP USAGE

HydroColor APP requires three images to be taken by the user with an open end forward-looking digital camera of a smartphone. The required images include; the water surface, the sky (which is used to correct the water surface image off water surface skylight reflectance), and an 18 % reflectance grey card (which is used as a measure of the down-welling irradiance from the sky and sun). The RGB values from a 200 × 200 pixel square at the centre of the three images are averaged. The averaged values are then used to obtain the relative radiance of the images by dividing the RGB of the images by the exposure time of the phone camera and subsequently used to derive the remote sensing reflectance $R_{rs}(RGB)$. It is from this $R_{rs}(RGB)$ that specific models are applied to derive turbidity, [SPM] and backscattering coefficient. The $R_{rs}(RGB)$ in this case is a calculated value rather than a direct field measured value (where a tube/cone is fitted around the camera lens to block skylight and water surface reflected light) (Goddijn & White, 2006; Lee et al., 2013).

In order to reduce the effects of sun glint and non-uniform sky radiance from the water surface image, the image is taken at a zenith angle of 40° from nadir and an azimuth angle of 135° from the sun as recommended by Mobley (1999). This is achieved by adhering to the compass display on the image capture screen. The image of the grey card is taken at the same zenith and azimuth angles as the water image. Taking the water surface and the grey card images at the same zenith and azimuth angle also avoid shading problems by creating the condition of having to block the same portion of the sky radiance for the two images. In order to capture the portion of the sky that contribute the most to the surface reflectance of the water image, the image of the sky is taken at a zenith angle of 130° from nadir and an azimuth angle of 135° from the sun as recommended by Mobley (1999).

ANNEX IV - COMPARISON OF CITCLOPS AND HYDROCOLOR APPS

A comparison of the Citclops and HydroColor APPs based on the required images, reference materials, RGB transfer functions, estimated water quality variable, advantages and disadvantages are as shown in Table 1.

Comparison of Citclops and HydroColor APPs

Citclops	HydroColor
Required Image(s)	
Water surface image.	Water surface, sky and grey card images.

Reference Material	
Digitalized FU colour comparator scale as reference material. The user can add information on Modern FU scale and Secchi disc measurements.	No reference material needed.
RGB Transfer Function	
From sRGB of water surface image to *xyz* chromaticity coordinates.	From sRGB of grey card, sky and water surface images to $R_{rs}(RGB)$.
Colour Space Conditions	
XYZ colour space; not dependent on the device used. Also, the resulting chromaticity coordinates does not depend on the illumination condition of which the image was taken.	RGB colour space; dependent on the device used. This is because; it is influenced by the specific spectral response function of the capturing device. Also, it depends on the illumination condition of which the image was taken.
Estimated Water Quality Variables	
Water surface colour translated to FUI.	Water turbidity (0-80 NTU), [SPM] (g/m^{3}), and backscattering coefficient in the red (m^{-1}).
Advantages	
It is only the upwelling light from the water surface that carries any useful information on the water body. By this, it only requires an image of the water surface which would be easier for citizen monitoring.	In deriving the $R_{rs}(RGB)$ using the three images, error incurred from each image as a result of the smartphone cancels out. Thus, the phone camera needs no calibration.
Disadvantages	
The weather conditions of the location are given as parameter values to be selected by the user concerning the location and not of the pertaining condition of the	Does not take into account the weather conditions such as the wind which can affect the resulting output. It is cumbersome for citizens who would

location. This can result in an optimistic estimate of water quality variables without correcting sun-sky glint effects on the water surface image.	like to take random measurements without the availability of a grey card.

ANNEX V – PROCESSED SMARTPHONE IMAGES

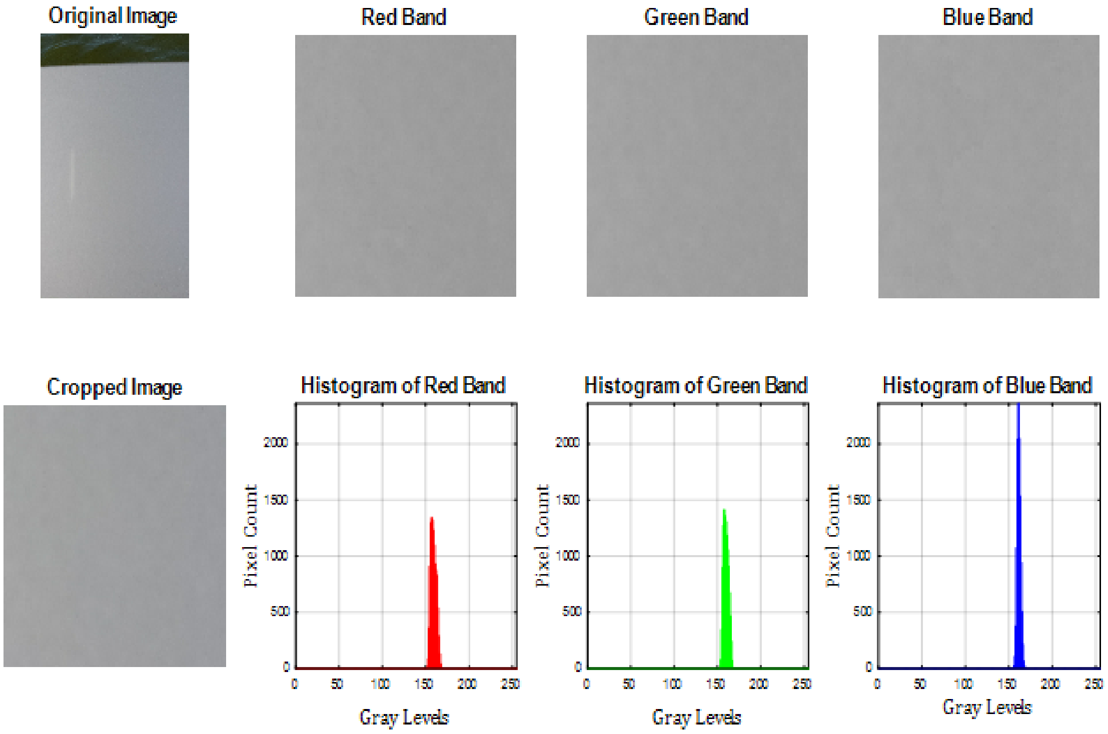
Original Image
Red Band
Green Band
Blue Band
Cropped Image
Histogram of Red Band
Histogram of Green Band
Histogram of Blue Band

Derived RGB bands of a grey card image. The upper panel from left to right is the original image, the red band of the cropped image, the green band of the cropped image and the blue band of the cropped image. The lower panel from left to right is the cropped image, histogram of the red band, histogram of the green band and histogram of the blue band.

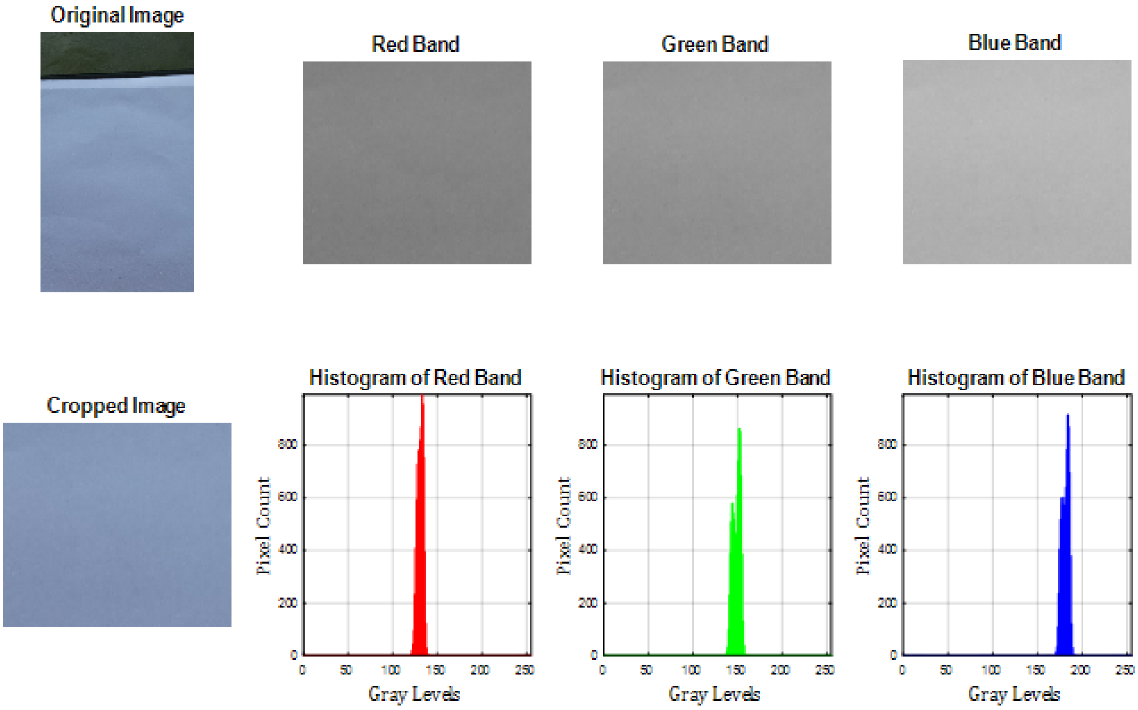

Derived RGB bands of a printed grey paper. The upper panel from left to right is the original image, the red band of the cropped image, the green band of the cropped image and the blue band of the cropped image. The lower panel from left to right is the cropped image, histogram of the red band, histogram of the green band and histogram of the blue band.

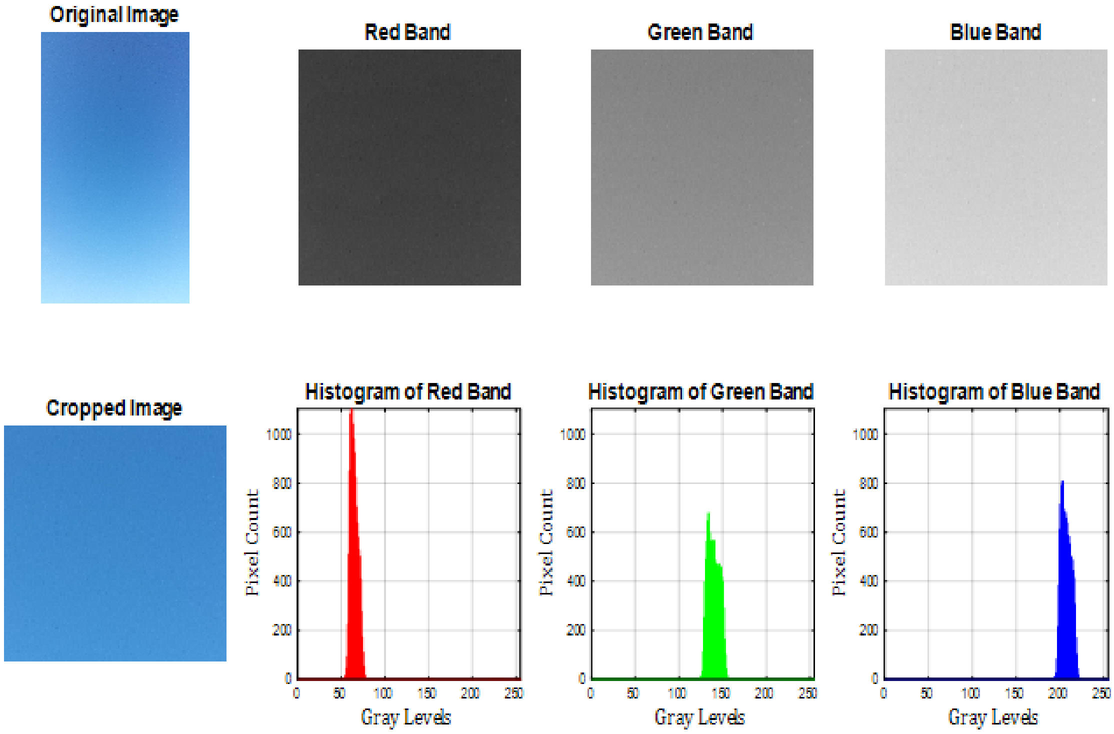

Derived RGB bands of a clear sky image taken at Kristalbad artificial wetland. The upper panel from left to right is the original image, the red band of the cropped image, the green band of the cropped image and the blue band of the cropped image. The lower panel from left to right is the cropped image, histogram of the red band, histogram of the green band and histogram of the blue band.

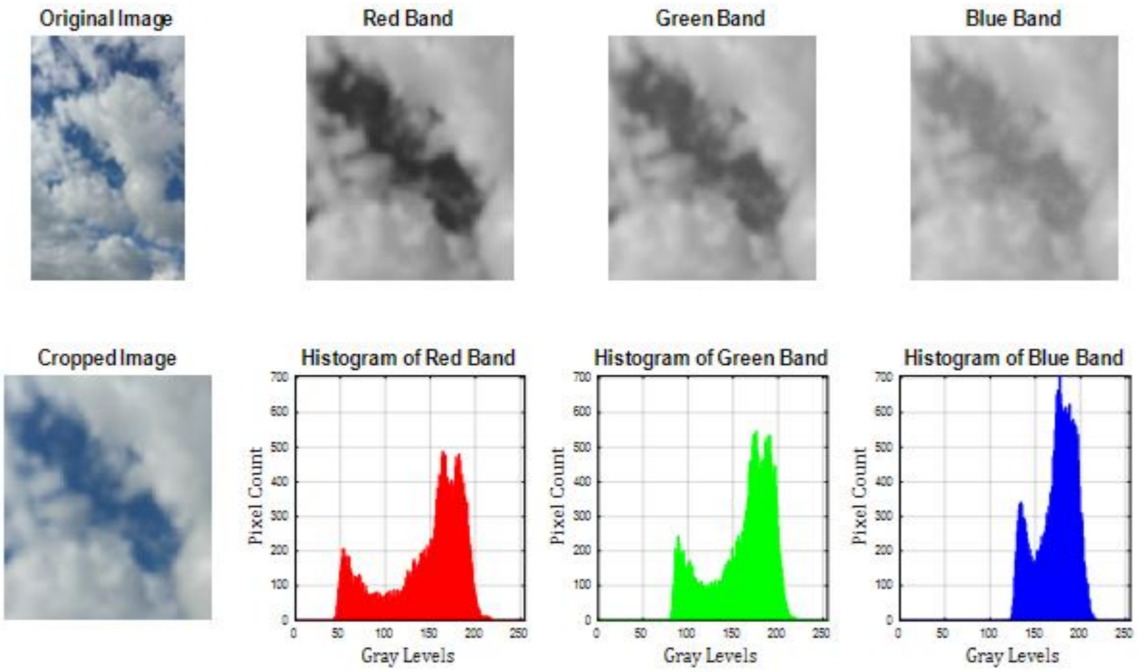

Derived RGB bands of a partial cloud image taken at Hulsbeek Lake. The upper panel from left to right is the original image, the red band of the cropped image, the green band of the cropped image and the blue band of the cropped image. The lower panel from left to right is the cropped image, histogram of the red band, histogram of the green band and histogram of the blue band.

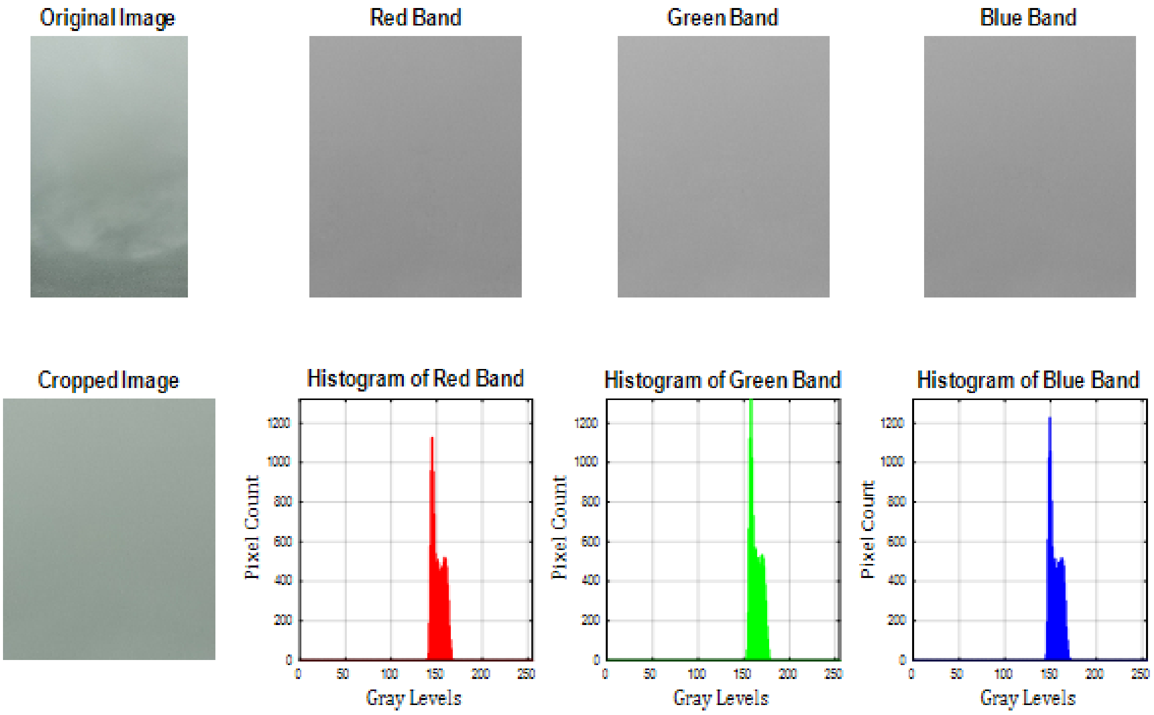

Derived RGB bands of an overcast cloud taken at Binnenschelde Lake. The upper panel from left to right is the original image, the red band of the cropped image, the green band of the cropped image and the blue band of the cropped image. The lower panel from left to right is the cropped image, histogram of the red band, histogram of the green band and histogram of the blue band.